NUMERICAL SIMULATION OF THE PLASTICS INJECTION MOULDING PROCESS

by

WILLEM JOHAN DE KOCK

Thesis Presented for the Degree of

DOCTOR OF PHILOSOPHY

in the

Department of Mechanical Engineering

UNIVERSITY OF CAPE TOWN

Supervisors : Prof J.B. Martin
Prof B.D. Reddy

1994

ABSTRACT

The Hele–Shaw formulation is widely used for the simulation of the injection moulding process. The influence of the Hele–Shaw approximations is, however, unknown. A two–dimensional numerical model based on the Hele–Shaw formulation, and a model based on the Navier–Stokes equations without the Hele–Shaw approximations were developed. The solutions obtained with these two approaches were compared to investigate the influence of the Hele–Shaw approximations on the simulation of the injection moulding process.

Weakly compressible, non–Newtonian flow of an amorphous polymer melt under non–isothermal conditions were simulated using constitutive equations generalized to non–Newtonian materials. The finite volume method, which is a very powerful method yet easy to use, was used to discretize the governing equations as compared to finite element methods used in most other reported models. The influence of the Hele–Shaw approximations on the solutions of specific flow cases was determined by comparing the solutions obtained with the model based on the Hele–Shaw formulation and the model based on the Navier–Stokes equations. Parametric studies were done to compare the solutions of the two numerical models for a wider range of flow cases.

The following conclusions were made as a consequence of this study : Numerical models to simulate the injection moulding process can be simplified and the computer time required to solve these models can be reduced by using the Hele–Shaw formulation instead of solving the full Navier–Stokes equations. Numerical models based on the Hele–Shaw formulation are well suited to simulate the injection moulding process when the geometries and flow conditions fall within certain limits. These limits are determined by the combined effect of the geometry and the flow conditions represented by the Reynolds number. The simplicity of the finite volume method used in the generalized Hele–Shaw model makes it an attractive model to use for injection moulding simulations.

DECLARATION

I, Willem Johan de Kock, declare that this thesis is essentially my own work and has not been submitted for a degree at another university.

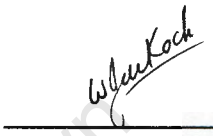

W J de Kock
December 1993

ACKNOWLEDGEMENTS

I wish to express my gratitude to Proff. J.B. Martin and B.D. Reddy for their encouragement and guidance.

I wish to thank Prof. G.P. Greyvenstein for many discussions.

I gratefully acknowledge the financial contribution which I have received from the Foundation for Research Development as part of their Development Programme in Manufacturing Technology.

I wish to thank my family, friends and colleaques for their support and patience, especially my wife Adri and our children.

TABLE OF CONTENTS

NOTATION, NOMENCLATURE AND ABBREVIATIONS

NOTATION

The following conventions are adhered to :

A decimal comma is used in the text.
A decimal point is used in the figures.
Boldface symbols indicate either a vector or a tensor.

NOMENCLATURE

Roman alphabet

a	coefficient
A	area
b	half–gap thickness
c_p	specific heat
d	increment
f	body force component, fractional volume of fluid
k	thermal conductivity
p	pressure
q	flow rate
s	seconds
SS	source term
T	temperature
T_g	glass transition temperature
t	time
u,v,w	cartesian velocity components
V	volume
V_s	specific volume
x,y,z	cartesian coordinate directions

Greek alphabet

∂	derivative
∇	del operator vector
η	non–Newtonian viscosity
η_0	zero–shear–rate viscosity
$\dot{\gamma}$	shear rate
μ	Newtonian viscosity
μ'	second coefficient of viscosity
ρ	density
τ	shear stress
δ	unit tensor
Γ	diffusion coefficient
Δ	increment, variation
κ	coefficient of bulk viscosity
Π	stress tensor

Subscripts

W	grid node left of the one currently under consideration
w	centre of cell face to left of grid node under consideration
N	grid node above the one currently under consideration
n	centre of cell face above the grid node under consideration
S	grid node below the one currently under consideration
s	centre of cell face below the grid node under consideration
E	grid node right of the one currently under consideration
e	centre of cell face to right of grid node under consideration
P	refers to the grid node currently under consideration
nb	refers to all four the neighbouring grid nodes
p	constant pressure
T	constant temperature
l	liquid phase
s	solid phase

Superscripts

*	tentative or guessed value
′	correction
‾	gap–averaged value
≈	dimensionless variable
t	present time level
t–1	previous time level
P	pressure
u	x–direction velocity
v	y–direction velocity
T	temperature

ABBREVIATIONS

FAN	flow analysis network
GHS	generalized Hele–Shaw
GN	generalized Newtonian
MAC	Marker and Cell
PC	polycarbonate
PISO	pressure–implicit split–operator algorithm
PP	polypropylene
PS	polystyrene
SIMPLE	semi–implicit method for pressure–linked equations
TDMA	tridiagonal matrix algorithm
VOF	fractional volume of fluid
WLF	Williams Landel and Ferry

LIST OF FIGURES

CHAPTER 1

1 INTRODUCTION

1.1 Background to injection moulding

1.1.1 Plastics injection moulding in perspective

Injection moulding is one of the major basic converting processes in the plastics industry. It is used to convert approximately 16% of the 90 million tons of plastics used world–wide each year. It is, however, a process which is far more important to the plastics industry than the 16% would indicate by virtue of the following :

- From a technology point of view injection moulding is at the forefront in the development of new polymers, new markets for plastics and the steadily increasing performance parameters of both plastics and plastic products.
- Items ranging in size from very small to very large can be produced by means of injection moulding.
- The added value achieved in the injection moulding process is considerably higher than in the other high–volume plastics conversion processes.

In the Republic of South Africa injection moulding accounts for approximately 17% of the volume of material converted annually but 22% of the total value of sales. In 1991, 575 000 tons of virgin polymer were converted with another 90 000 tons of recycled material. Total sales value of this converted product amounted to R6 000 million (Naudè, 1992).

Injection moulding technology has developed rapidly since the first hand–operated machine was built in 1930. Today injection moulding is an automated process. Machine parameters are measured in–time and injection moulding machines are close–loop computer controlled. The manufacture of products with very small tolerance requirements, products with complex geometries or very large products, all require advanced product and mould design technology.

The subject that deals with the computer simulation of fluid flow and heat transfer problems, which is also present during the plastics injection moulding process, is known as Computational Fluid Dynamics (CFD). CFD is a rapidly developing subject. This development is due to computer developments and the rapid development of new and improved numerical algorithms. Much research is currently being done to apply CFD to a wide range of industrial processes, including injection moulding.

1.1.2 Properties of polymer melts

Thermoplastic polymers are weakly compressible viscoelastic materials with temperature– and pressure–dependent physical properties. The basic principles governing the processing of thermoplastic materials were already established during the early 1950's. However, the complexity of the mathematical models has resulted in extensive research to develop simplified models.

In general, polymer melts have densities of approximately 1000 kg/m^3, low thermal conductivity, approximately 0,1 $W/m^\circ C$, and high viscosity, typically $10^2 - 10^4$ Ns/m^2. The density and low thermal conductivity give rise to diffusivities of the order of 10^{-7} m^2/s and result in long heating and cooling times (Powell, 1983). The high viscosities result in very low Reynolds numbers which means that the flow is always laminar. The Reynolds numbers for polymer melt flow is typically much less than one.

Polymer melts are viscoelastic. This means that under certain circumstances the response to stress is essentially viscous and under other circumstances the response is essentially elastic. Polymers undergo a phase change from solid to liquid over a finite temperature range and not at one particular temperature. Below this range, their behaviour is that of elastic solids showing some viscoelasticity in the form of time–dependent properties such as relaxation. Above the melting range, polymer melts may be regarded as highly viscous liquids exhibiting some elastic effects.

The relationship between the stress and shear rate of a polymer melt can be modelled with either an inelastic or a viscoelastic model. An inelastic model would be used to simulate viscous behaviour in steady shear flow. A viscoelastic model would be used to predict the time–dependent behaviour such as stress relaxation of viscoelastic fluids in unsteady flow.

The shear viscosity and the density of polymer melts are both temperature– and pressure–dependent. The viscosity is also dependent on the shear rate. Equations which give the relationship between the thermodynamic properties and models which describe the viscosity mathematically, are discussed in section 1.2.2.

The fountain effect is a property of polymer melts flowing through a thin rectangular cavity and can be described as follows. Material passes through the fountain region as it is transported from the hot core region to the cold layer developing at the wall behind the advancing melt front. The fountain region refers to the region in the vicinity of the advancing flow front. Although the direct effect of the fountain region upon the overall pressure drop will be small for thin cavities, it may contribute to the developing temperature field.

1.1.3 Description of the injection moulding process

Injection moulding is a process for producing plastic products by injecting a molten polymer into a closed mould cavity under high pressure. The mould is continuously cooled to keep it at an almost constant temperature which is well below the polymer melting temperature.

From a processing or machine setting point of view the injection moulding process can be divided into a filling stage and a holding or packing stage. The hydraulic system of the injection moulding machine is set to change over from injection pressure to holding pressure approximately when the mould is completely filled. The holding pressure forces more material into the mould after it has been filled. This packing process compresses the material to compensate for shrinkage of the molten material due to cooling which takes place through heat exchange with the solid walls of the colder mould. As soon as the injected molten material comes in contact with the mould a solidified skin is formed. The material then solidifies progressively inwards due to the continuous cooling. After the gate (a small opening in the cavity through which the injected material enters the cavity) has solidified, no more material can enter the cavity. When the product has solidified sufficiently it is ejected from the mould.

To produce an injection moulded plastic product involves more than the actual process of injection moulding. First the product has to be designed, taking into account that it will be injection moulded. Then the mould is designed, including the design of a runner system, gate, cooling channels and ejecting mechanism which are basic features of a mould. After the mould has been machined and assembled it is installed on an injection moulding machine. Then the processing parameters are set on the computer which controls the machine.

To design an accurate mould, the mould designer has to be able to

predict several aspects of the injection moulding process. Most important are the mould–filling pattern, injection pressure, maximum shear stress, part solidification and shrinkage. The predicted flow path of the material is used to locate and dimension the gating system of the mould and to determine the position of weld lines. The mould is dimensioned by taking the estimated shrinkage during cooling into account. The flow of the plastic into the mould also has a pronounced effect on the strength and the appearance of the product. As dimensional and strength requirements for plastic products have become more stringent and as injection moulds have become more complex and expensive, the designer can no longer rely only on his practical experience. Consequently, computer simulation models have been developed during recent years to assist in the process of designing plastic products and injection moulds. Today the simulation of the injection moulding process plays an important role in advanced injection mould design.

1.1.4 Simulation of the injection moulding process

For the purposes of the present study the definition of the injection moulding process will be limited to the process starting with the injection of the molten polymer into the mould up to the point where the product has cooled down sufficiently to be ejected from the mould.

The injection moulding process can be divided into an injection and a holding stage. The change–over between injection pressure and holding pressure is set on the machine as a function of either pressure or the volume of the material injected into the mould. The change–over point does not necessarily coincide with the instant when the mould is filled, and packing may already commence under injection pressure. Although this change–over point can be easily determined physically, it would be difficult to simulate it numerically.

We divide the injection moulding process, from a numerical simulation point of view, into a filling stage and a post–filling stage, as compared

to the injection and holding stages. The filling stage is the period from the beginning of the injection moulding process until the mould cavity is completely filled. The post–filling stage commences at the instant when the mould is completely filled. Since the actual flow of the melt is simulated, the change–over point between the two stages defined in this way can be accurately determined numerically.

The post–filling stage includes the time after filling during which material still flows into the mould until the gate solidifies or the melt becomes stationary, and the time between commencement and termination of the holding pressure. It also includes part of the cooling time. As indicated in Figure 1.1 these time spans overlap since the gate can solidify at any time after commencement of the holding pressure and not necessarily when the pressure becomes zero.

For simulation purposes the packing time, during which more material

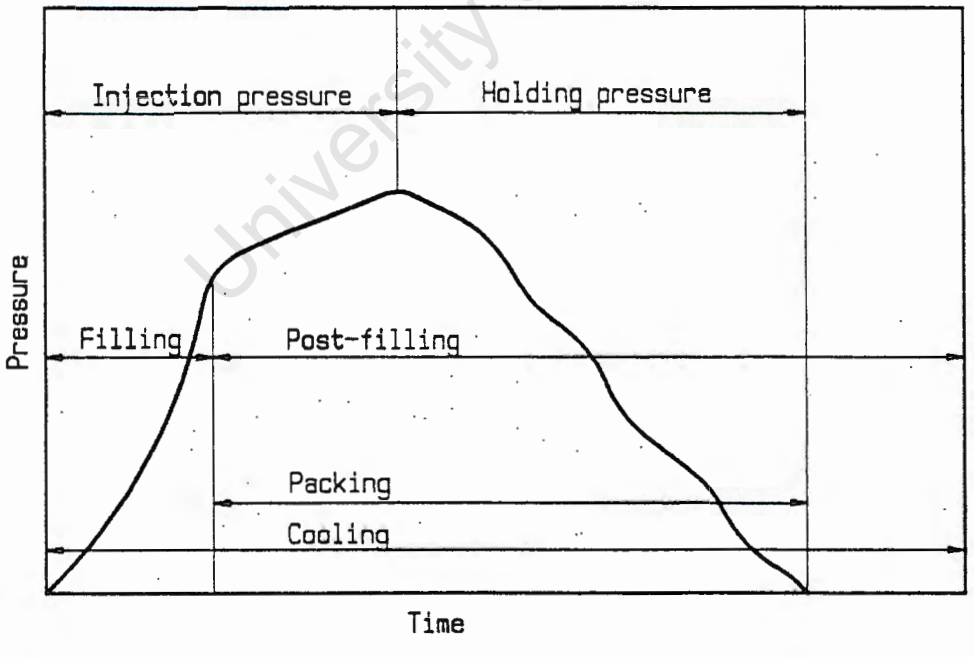

FIGURE 1.1 The injection moulding cycle.

flows into the cavity, is defined as the time from mould filling until the melt becomes stationary, at which stage the holding pressure at the inlet is terminated. After the holding pressure has been terminated the melt is stationary and the cooling can be modelled as one–dimensional heat transfer through the thickness.

Comprehensive research has been performed to enable researchers to simulate numerically the filling stage. Several commercial codes have been developed as a result of this research. The main objectives of the numerical simulation of the filling stage are to assist designers in

i) determining the appropriate number and location of gates;
ii) sizing the length and cross–sectional area of the runner system (channels through which the injected material gets delivered to the gate);
iii) locating vents in the cavity to prevent scorching which can occur if the air in the cavity gets trapped and heated up due to compression;
iv) determining appropriate processing conditions for the given material and mould; and
v) avoiding weld lines which are formed where two flow fronts meet.

Simulation of the filling stage has already been developed to such an extent that the emphasis has shifted to the post–filling stage. There is, however, still scope for further research of the filling stage since existing simulations are based on simplifications necessitated by the complexities inherent in polymer melt flow.

Much of the research on injection moulding simulation has focussed on only one of the stages. The simplifications that can be made in the simulation models are not the same for the two stages. This is due to the difference in flow characteristics and cooling effects in the filling and post–filling stages.

1.2 Literature survey

1.2.1 Numerical models

1.2.1.1 Filling stage

Many researchers report on simulation models based on Hele–Shaw flow, for which only one hydrodynamic variable, the pressure (p), is solved. Before reviewing the literature reporting on Hele–Shaw based models, the approximations leading up to the generalized Hele–Shaw approximations are discussed briefly.

An assumption in the literature that is often used for polymeric systems is the creeping flow assumption, i.e. that the viscous forces are considerably greater than the inertia forces. Creeping viscous flows in slowly varying, relatively narrow gaps are usually handled with the lubrication approximation. The following assumptions (Lee & Castro, 1989) are made in standard lubrication theory :

i) The fluid is incompressible and Newtonian.
ii) The flow is steady, isothermal and laminar.
iii) The inertial forces resulting from the acceleration of the fluid are negligible compared to the viscous shear forces.
iv) The gap height is very small compared to other dimensions.
v) The gap height h varies very slowly with x and z.
vi) There is no slip at the wall surfaces.

The only assumptions that are not valid during the filling stage of injection moulding are the assumptions of a Newtonian fluid and isothermal flow. However, if the x and z velocities vanish at the upper and lower boundaries of the gap (where y=+b and y=–b), the restriction of a Newtonian fluid can be relaxed so as to incorporate the lubrication approximation.

To use the lubrication approximation for mould filling, the viscoelastic

effects and normal stress effects must be negligible. The latter requirement is reasonable since shear flow is dominant in the mould–filling process. It is clear from the first requirement that the lubrication approximation cannot be used if we want to include viscoelastic effects. However, the generalization of classical lubrication theory to non–isothermal, non–Newtonian flow, called the generalized Hele–Shaw formulation, has according to Güceri (1989) become the standard way to formulate injection mould filling problems.

Richardson (1972) was the first to suggest a solution method for a Hele–Shaw type of flow of a Newtonian fluid between parallel plates produced by the injection of fluid. Broyer et al. (1975) report on the development of a theoretical model for the cavity–filling process applicable to non–Newtonian incompressible flow in narrow gap cavities. Their major contribution was to extend previous work to include non–Newtonian fluids.

The generalized Hele–Shaw model introduced by Hieber and Shen (1980) provides simplified governing equations for non–isothermal, non–Newtonian and inelastic creeping flows in thin cavities. Besides the usual lubrication approximations, the velocity component in the thickness or gap direction is also neglected. Therefore the pressure is a function only of the other two spatial variables. The inertial forces are considered to be much smaller than the viscous forces. Hieber and Shen employ a hybrid numerical scheme in which the planar coordinates are described in terms of finite elements (triangular elements and quadratic shape functions are employed for p) and the gap–wise and time derivatives are expressed in terms of finite differences. The numerical solution of the field equation for pressure is carried out by successive under–relaxation. In advancing the melt front they neglect the fountain effect and treat the melt front as being flat in the gapwise direction, which is perpendicular to the flow direction. Once the pressure and temperature fields have been determined at the current time, the two

velocity components at the vertex nodes along the current melt front can be evaluated. For a given time step, these fluid particles are accordingly advanced to form the new melt front. If we compare this hybrid formulation with preceding work it is much more suitable for handling cavities of a more general planar geometry.

Wang and Hieber (1988) report on advances to simulate the filling stage in terms of the melt viscosity of an incompressible fluid using thin two–dimensional finite elements. They describe the filling stage as creeping, shear–dominated flow which might also be treated in terms of classical Hele–Shaw flow as generalised to a non–Newtonian, non–isothermal, non–steady situation. They extend the method of Hieber and Shen (1980) by employing a fixed finite element grid and control volumes. They use triangular finite elements and join the centroids of the elements to the midpoints of the three corresponding sides, thereby creating polygonal control volumes. The purpose of creating these control volumes is to make the melt–front advancement amenable to an automated algorithm.

Dupret and Vanderschuren (1988) report on the calculation of the temperature field during the filling stage. They consider the creeping flow of an incompressible generalized Newtonian fluid using two–dimensional finite elements with polynomial approximation of the temperature in the thickness direction normal to the walls. Following Schlichting (1979) they use the Hele–Shaw formulation. The resulting system of equations is two–dimensional for the pressure field and remains three–dimensional for the temperature field. Since they concentrate on non–isothermal effects during the filling stage, their contribution is the prediction of three–dimensional thermal effects during the filling of a thin cavity of arbitrary shape.

The application of fully developed Hele–Shaw flow gives rise to errors in the entrance region, and is also unsatisfactory in the presentation of the

front region, according to Kamal and Lafleur (1982). In an attempt to develop a model to represent both the entry and the fully developed regions they make assumptions which are less restrictive than for Hele–Shaw flow. These assumptions, which are physically representative of a non–Newtonian fluid flowing in a thin, rectangular cavity, are :

i) The fluid motion is laminar.
ii) Body forces are negligible.
iii) The unsteady terms in the momentum and continuity equations are neglected in view of the comparatively long duration of the flow.
iv) There is no velocity component in the z direction.

Kamal et al. (1988) present a two–dimensional model, based on the solution of the two–dimensional Navier–Stokes equations, to simulate unsteady free–surface flow and transient cooling during the filling of a rectangular cavity. They consider a thin cavity and neglect variations in the z direction. Assuming that the polymer melt is incompressible and that body forces are negligible they solve for u, v and p from the momentum and energy equations. The objectives are to incorporate phenomena such as viscoelasticity, crystallinity and the shape of the melt front and to determine their effects on the structure of the flow field.

Le Grange (1990) presents a finite volume numerical model for solving polymer melt flow in injection moulds. The continuity, momentum and energy equations are considered in terms of general curvilinear coordinates in two dimensions and the three hydrodynamic variables p, u and v are solved. Only incompressible flow is considered and the power law is used to model the viscosity.

1.2.1.2 Modelling the movement of the flow front

Various methods have been developed for modelling the moving boundary in injection mould filling. The Marker–and–Cell (MAC)

method (Browne, 1978) was originally developed to study transient incompressible viscous flows with free surfaces in the field of hydraulics. According to Wang and Lee (1989) an extended version of MAC simulates the fountain flow effect of non–Newtonian fluid flow applied to a two–dimensional isothermal filling process of simple geometries, i.e. parallel plate and radial flows. The MAC method utilizes a fixed or Eulerian mesh for the finite difference calculations and a Lagrangian set of marker particles to delineate the moving free surfaces. For better solution accuracy a staggered grid system is used in which the velocity components are located at the centres of the cell sides and the other variables at the cell centres. First, the coordinates of marker particles representing the fluid domain, are stored. After the velocity field of the fluid flow has been calculated, marker particles are then moved with a weighted average of the four nearest cell velocities. At this time all cells are properly flagged as empty, full or surface cells depending on the distribution of marker particles. This cell information is used to define the boundaries of the flow domain for the next time cycle. This technique has been especially useful in analyzing the fountain flow phenomenon in the x–y plane. However, it is difficult to use the MAC method to simulate the filling process of complex moulds without making major extensions.

The flow analysis network (FAN) approach (Broyer et al., 1975) extended the MAC concept into the low Reynolds number flow regime, using lubrication theory in the x–y plane instead of the Navier–Stokes equations. In terms of free surface tracking, FAN uses the flux calculations at the boundary of each control volume to check the fraction of fill in order to trace free surfaces instead of tracking marker particles. They also assume that the fluid in each element is concentrated at the centre, or node, of the element. The pressure is calculated using the conservation–of–mass principle. With the pressure known, the flow rates into the front nodes can be calculated. A parameter, f, gives the element volume fraction into which the fluid is

allowed to flow. They report that the region of the fluid front where the flow is not developed (i.e. where the Hele–Shaw assumption does not hold) constitutes a small portion of the fluid inside the mould and that the pressure drop across the fluid front is usually very small and its influence on the total flow field is negligible. Therefore it is assumed that the velocity profiles through the whole flow field are fully developed. One limitation of this control volume technique is that time steps must be controlled to ensure that the free surfaces pass only one layer of control volumes in one time step. A scheme to correlate the time steps and the flow front control volumes was implemented in the FAN programme. The use of a global coordinate system and multi–dimensional indexing within the context of the finite difference method causes two major problems in using the technique to simulate mould filling : firstly, in addition to the tedious layflat technique, a great amount of additional data on the joint nodes which connect the planes of the model must be entered. Secondly, there are two different indices associated with each connecting node, representing its identity in two different planes. These two indices have to be individually specified by the user in order to form a global matrix for the unknowns. The intrinsic nature of the finite element approach eliminates these constraints, giving it an advantage over the finite difference technique in this application.

The fractional volume of fluid (VOF) method developed by Hirt and Nichols (1981) is based on the same concept of checking the fraction of fill in order to trace free surfaces instead of tracking marker particles, but they employ a finite difference technique in their solution procedure. The VOF method is a simple and efficient means for numerically treating free boundaries embedded in a calculational mesh of Eulerian cells. It is shown to be more flexible and efficient than other methods for treating complicated free boundary configurations. It uses a minimum of stored information, treats intersecting free boundaries automatically and can be readily extended to three–dimensional calculations.

Wang and Lee (1989) describe a mixed finite element and control volume approach for injection mould filling. In this numerical algorithm, the finite element formulation for the fixed mesh of linear triangular elements has been derived using local coordinates, and the control volume approach is used only to define the flow fronts. The method is limited to generalized Hele–Shaw flow.

1.2.1.3 Post–filling stage

The stage of the injection moulding process during which the mould cavity is packed under pressure and during which most of the cooling takes place, is referred to in the literature as the holding pressure stage (Michaeli & Lauterbach, 1989) or the packing–cooling stage (Huilier et al. 1988b) or the post–filling stage (Hieber et al. 1986). We will refer to it as the post–filling stage.

The basic approach for the simulation of packing during the post–filling stage is the same as for the filling stage except for the boundary conditions. The continuity, momentum and energy equations are simplified, using the following set of assumptions :

i) The fluid is weakly compressible.
ii) The fluid motion is laminar.
iii) Body forces are negligible.
iv) Velocity components in the thickness direction are negligible.
v) The effect of the pressure terms in the energy equation is negligible.

During cooling in the post–filling stage, i.e. after the gate has solidified or the melt has become stationary, no additional material enters the cavity. Since there is no more fluid motion, the problem can be approximated as one–dimensional heat transfer by conduction, through the thickness of a polymer melt contained between two cooling plates.

According to Lafleur and Kamal (1986), relatively little experimental or

theoretical work had been carried out before 1986 with regard to the post–filling stage. Following is a review of some of the development work since 1986.

Lafleur and Kamal (1986) assume that the bulk of the polymer cools very little during the filling stage as well as during packing in the post–filling stage, but next to the mould surface there will be a rapidly cooling thin skin of polymer. The partial differential equations are simplified, using the abovementioned assumptions, and solved using a finite difference method together with the MAC technique. This model solves for u, v and p. During the cooling time after packing no flow takes place, reducing the complexity of the mathematical treatment considerably. The momentum and continuity equations are not required and the energy equation is simplified by the absence of the generation of viscous heating and by neglecting convection terms and the effect of the pressure drop.

Huilier et al. (1988a) assume the unsteady compressible flow of the post–filling stage to be incompressible during one time step. After each time step the compressibility of the polymer melt is readjusted by a mass balance. The pressure is then calculated from the temperature and density through an equation of state. They use a finite difference scheme to solve the momentum and energy equations simultaneously for flow in elementary geometries (thin plates, disks or cylinders). The packing in the post–filling stage is considered as a dynamic non–isothermal flow process and the cooling as a static (no flow) process. The decrease in the melt cross–section due to solidification during cooling is not taken into account.

Huilier et al. (1988b) report on the study of transient, non–isothermal and weakly compressible flow of a non–Newtonian fluid into a cavity which is already filled and cooled at low temperature. They consider a thin rectangular cavity and use a finite volume method, applied to a

space–staggered grid, to simultaneously solve the continuity, momentum and energy equations. Since the cavity is thin they assume the pressure to be constant through the thickness and the velocity field to be one–dimensional. The post–filling stage is divided into two parts. Compressible flow and cooling without flow after the gate has frozen. The filling stage is not modelled.

Chiang et al. (1991a) employ a unified theoretical model to simulate the filling and post–filling stages. The analysis is based on a hybrid finite element/finite difference numerical solution. They consider generalized Hele–Shaw flow for a purely viscous fluid of variable density under non–isothermal conditions. The same model also simulates the post–filling stage. Although variable–density effects are negligible during the filling stage, compressibility is taken into account during both stages since, in more complex models, parts of the cavity may fill and experience variable–density effects while other parts of the mould are still unfilled.

1.2.1.4 Solution algorithms

To solve the differential equations of the numerical model, a solution method is required. Most models employ either a finite element method or a hybrid scheme in which finite elements are used to describe variations in the planar coordinates and finite differences are used for variations in the gapwise direction and in time. However, finite difference methods are also well suited to solve fluid flow problems. Finite difference methods are, from a mathematical point of view, less complex and generally less computationally intensive than finite elements.

The finite difference method is older and easier to learn and use (Güceri, 1989) than the finite element method. Finite difference methods originated in the 1930's for hand calculation. Their use expanded rapidly with the development of digital computers. Despite

their limitations, traditional finite difference techniques still represent the most developed and best understood numerical procedure for solving partial differential equations. They also form the basis of more contemporary finite difference methods which can handle a wide variety of complex problems. Traditional finite difference techniques lack the ability to model complicated shapes. Later developments have included coordinate transformations which make numerical grid generation possible. This has led to the development of finite volume methods which can handle complex geometries, thus making them comparable to finite element methods in geometry flexibility, while they retain the characteristic of finite difference methods of being less computationally intensive than finite element methods.

Philipon et al. (1986) have employed the finite difference method to simulate two–dimensional mould filling. They describe a complex mould using the lay–flat technique and three kinds of elementary geometries. In each elementary geometry and at each time step the mechanical and thermal equations are solved throughout the thickness of the mould using implicit finite difference discretization. Although the results are reported to be in good agreement with experimental measurements, this model requires much manual pre–processing to prepare the geometric input data. The limited usage of this approach is due to its lack of front tracking capability (Wang & Lee, 1989).

Kamal et al. (1988) developed a comprehensive two–dimensional mathematical model to evaluate the effects of viscoelasticity, non–isothermality and fountain flow on the structure of the flow field in a rectangular cavity. The equations were solved using the MAC method. The rectangular cavity between the centre line and the mould wall was discretized in the plane between the flow direction and the gap–wise direction, for the finite difference representation of the model equations. They solve for u, v and p in this two–dimensional model.

1.2.2 Constitutive equations

The constitutive equations should include an equation of state describing the relationship between the thermodynamic properties of the molten material. It should also include a viscosity model to describe the relationship between the thermodynamic properties, the shear rate and the viscosity. Various equations of state and viscosity models have been developed and reported in the literature.

1.2.2.1 Equations of state

Theoretical equations of state, based on statistical mechanics, have been developed for polymers in general, as reported by Kamal and Ryan (1989). However, for most polymer–processing applications, empirical equations of state have been generally used due to their computational simplicity and the necessity for determining relatively few adjustable parameters. We will therefore only discuss empirical equations as reported in the literature.

The most common approximation employed by researchers to simplify the equations used for the filling stage is that of incompressibility, in which case no equation of state is required. However, during the post–filling stage compressibility effects have to be taken into consideration. Kamal and Lafleur (1986) used experimental data obtained directly from the pressure–volume–temperature (pVT) diagram. An equation of state with a wide range of applicability is, however, required to be able to model different polymer materials.

According to Kamal and Lafleur (1982) the most widely used equation of state for polymer melts is the Spencer–Gilmore equation which is a modified form of Van der Waal's equation. It has the simple form

$$(p + a)\,(V_s - b) = \frac{R}{M}\,T\,, \qquad (1.1a)$$

where V_s is the specific volume, a, b and M are arbitrary material constants and R is the gas constant.

Hieber et al. (1986) employ an equation of state based on the Spencer–Gilmore equation. It is used to incorporate compressibility effects in the post–filling stage of a one–dimensional filling simulation of a strip cavity :

$$(p + p')\left(\frac{1}{\rho} - \frac{1}{\rho'}\right) = R'T, \qquad (1.1b)$$

where p', ρ' and R' are constants for a given material. They compare the results obtained for Polystyrene (PS) and Polypropylene (PP) but give the material constants required in the Spencer–Gilmore equation only for PS.

Various workers have introduced non–linear equations of state based on the empirical equation of P.G. Tait (1900: Physics and Chemistry of the Voyage of H.M.S. Challenger as referenced by Wood, 1964) originally proposed to represent the volume–pressure relationship for sea water :

$$V_s(p,T) = f(T)\cdot(1 - c_t\cdot\ln(1 + p/g(T))) \quad , \qquad (1.2)$$

where c_t is a constant and f(T) and g(T) are functions of the temperature.

Breuer and Rehage (1967) noted the apparent linear dependence of volume upon temperature and proposed, starting with the Tait equation, the relationship

$$V_s = V_0 + \phi_0\, T - \frac{k_0}{a}(1 + bT)\cdot\ln(1 + ap) \quad , \qquad (1.3)$$

where a and b are adjustable parameters and V_0, ϕ_0 and k_0 are,

respectively, the specific volume, the slope of the V_s–T curve and the derivative $\left[\frac{\partial V_s}{\partial p}\right]_T$, all evaluated at 0°C and zero pressure.

According to Huilier et al. (1988b) the equation of Tait is a good representation of the thermodynamic behaviour of amorphous polymers, since it approximates the pVT diagram well. They used the Tait equation (1.2) with $f(T) = a \cdot T + b$ and $g(T) = c \cdot e^{-dT}$ where c_t, a, b, c and d are constant material coefficients. Each of the coefficients a, b, c and d has two values, the value used depending on whether the temperature lies above or below the glass–transition temperature, T_g , i.e. the temperature at which the material softens and the modulus of elasticity drops by several orders of magnitude (Powell, 1983).

Since the actual pVT diagrams for molten polymers do not give a linear relationship between pressure and density, as some other workers assume, Huilier et al. (1988a) have decided to choose the empirical Tait equation which, according to them, smoothes the pVT diagrams. They use the same functions and constants given in the previous paragraph and state that this equation is simple and describes, for amorphous polymers, changes of specific volume in the liquid or molten state with good accuracy. It is also satisfactory for the glassy or rigid state (where $T<T_g$) if thermal history is omitted.

Chiang et al. (1991a) model the specific volume with a double–domain Tait equation which is the same as equation (1.2) but which is capable of describing both the liquid and solid regions. This is achieved by representing f(T) and g(T) by different equations depending on whether T is larger or smaller than T_g, where T_g is assumed to be a linear function of pressure.

The appropriate choice of an equation of state depends upon the nature of the information desired (e.g. the specific volume, thermal expansion coefficient or compressibility coefficient) and the accuracy required by

the user. For the purpose of numerical flow simulation we require only the density (i.e. the inverse of specific volume), as a function of pressure and temperature in the transport equations.

1.2.2.2 Viscosity models

Viscosity of a polymer melt depends not only on the pressure and temperature, but it also has a very strong dependence on the shear rate, resulting in a shear–thinning effect. This means that high shear rates, e.g. near the boundaries of the cavity where no–slip boundary conditions are assumed, will result in a low local viscosity (i.e. the material becomes "thin").

For many polymer melts, the logarithm of viscosity plotted as a function of the logarithm of strain rate exhibits linear behaviour over a range of strain rates typically encountered in polymer processing operations (Kamal & Ryan, 1989). This observation suggested the use of a simple power–law expression between shear stress and shear rate :

$$\tau = m(T)\dot{\gamma}^{n(T)} \quad . \tag{1.4}$$

The consistency index m and the power–law index n depend on the particular fluid and on the temperature but not on the strain rate. For a Newtonian fluid n=1 and for a shear–thinning material n<1. Typical values of n for polymer melts lie between 0,20 and 0,35 (Wang & Hieber, 1987). Since viscosity is defined by $\eta = \tau/\dot{\gamma}$, the viscosity model can be written as

$$\eta = m\dot{\gamma}^{n-1} \quad , \tag{1.5}$$

where again m and n are functions of T.

Dupret and Vanderschuren (1988) used the power law in their calcula–

tion of the temperature field during the filling stage for an incompressible, non–Newtonian fluid. They suggest that a fairly good approximation for m(T) is the experimental viscosity law,

$$m(T) = m_0 e^{-aT}, \tag{1.6}$$

under the assumption that the thermal conductivity, specific heat and specific mass do not depend on temperature ; here m_0 and a are constants.

Hieber et al. (1983) give the temperature dependence of m as

$$m(T) = A \exp\left[\frac{T_a}{T}\right] , \tag{1.7}$$

in their numerical investigation of the filling of thin cavities with an inelastic **power–law** fluid. They report good agreement between the predictions and measurements for the shape of the melt front, the location of weld lines and the pressures in the cavity.
Wang and Hieber (1988) report that the **power–law** approximation remains valid throughout the post–filling stage since the stress levels during cooling are still high due to very high viscosities at low temperatures, even though the flow rates may be low. For the post–filling stage they therefore extend the inelastic modelling of the filling stage by incorporating compressibility.

In their literature review Huilier et al. (1988b) report that all previous models for simulating the packing stage assume the viscosity to be pressure–independent. This is also true of the power–law model. They took pressure effects into account, using an exponential relation

$$\eta = \eta_0 \exp(p/p_0) \quad , \tag{1.8}$$

where p/p_o is the pressure correction on viscosity, (typically for PS p_o = 30MPa) and the zero–shear–rate viscosity, $\eta_0(\dot{\gamma},T)$, is calculated by interpolation from flow curves. They state that since it has been established that viscosity is the most important physical parameter controlling packing (Huilier et al. 1988a), pressure effects on viscosity are not negligible, considering the high level of pressures occurring during packing.

Although the algebraic simplicity of the power–law model and the small number of material parameters make it attractive for engineering calculations, the most serious limitation is that it does not describe the portion of the viscosity curve near $\dot{\gamma} = 0$ where $\eta = \eta_0$. Various empiricisms have been developed.

The Carreau model has been very successful in correlating experimental viscosity data and is relatively easy to use, according to Kamal and Ryan (1989). This model is given by

$$\frac{\eta - \eta_0}{\eta_0 - \eta_\infty} = [1 + (\lambda \dot{\gamma})^2]^{\frac{n-1}{2}} \quad , \tag{1.9}$$

where η_∞, is the upper limiting Newtonian viscosity and λ is a time constant.

Mavridis et al. (1986) report that the results of their simulation of purely viscous fluid flow in two–dimensional channels and tubes are indistinguishable at high shear rates if they use the power–law and Carreau models respectively. Furthermore, simulations of power–law and Carreau fluids produce essentially the same quantitative results as those obtained for Newtonian fluids for planar flow.

Schmidt and Menges (1986) added the temperature dependence of

viscosity to the **Carreau** model, using the temperature shift function or WLF function (Williams, Landel & Ferry, 1955). The five material constants required in this model are, however, not readily available for different materials.

Another popular empirical viscosity model (Kamal & Ryan, 1989) is the **modified Cross** expression (Cross, 1979) given by

$$\eta = \frac{\eta_0}{1 + [\eta_0 \dot{\gamma}/\tau^*]^{1-n}} , \qquad (1.10)$$

where τ^* is a material constant characterizing the shear–stress level related to the transition between the Newtonian and power–law regimes. This model gives a smooth transition between the Newtonian (zero–shear–rate viscosity) and power–law limits. Wang and Hieber (1988) employ the modified **Cross** model since the power–law model is valid only for polymer melts for which the Newtonian viscosity limit is reached at very low shear rates.

Polycarbonate, (PC) for instance, has a shear–thinning transition at 10^3 s^{-1} (at T = 290° C) and the power–law model would over–estimate the shear viscosity at lower shear rates. These authors incorporate temperature and pressure dependence resulting in a 5–constant model for the filling stage and a 7–constant model (using the WLF functional form) for the post–filling stage. They report that the two viscosity models give essentially the same results (which are also in very good agreement with the measurements) for the filling stage. During the post–filling stage the 5–constant model under–predicts the required pressure drop whereas the 7–constant model describes the data quite well.

1.3 Objective of this study and approach to be followed

1.3.1 Objective

The objective of this study is to determine the influence of the Hele–Shaw approximations on the simulation of the injection moulding process by comparing the results of two models in which different approaches are used. A two–dimensional numerical model based on the Hele–Shaw formulation, and a model based on the Navier–Stokes equations without the Hele–Shaw approximations, will be developed. The solutions obtained with these two approaches will be compared within the framework of the same finite volume discretization method and the same constitutive equations generalized to non–Newtonian materials.

1.3.2 Approach

A two–dimensional generalized Hele–Shaw (GHS) model based on the Hele–Shaw formulation and generalized to non–Newtonian flow under non–isothermal conditions will be developed. The movement of the flow front will be included in the simulation of polymer melt flow in the filling stage. The post–filling stage will be simulated by using the values obtained at the end of the filling stage as input. Constitutive equations, generalized to non–Newtonian materials, will be used to model the weakly compressible, non–Newtonian flow of an amorphous polymer melt. A finite volume method will be used to discretize the governing equations, as compared to finite element methods used in most other reported models. One of the Hele–Shaw approximations for a thin cavity, representing part of an injection mould, is to assume that the pressure is constant through the thickness. Therefore the two–dimensional finite volume grid, used to solve for the pressures, lies on the x–z plane through the centre of the cavity. The other variables are calculated in a three–dimensional grid.

A two–dimensional generalized Newtonian (GN) model solving the Navier–Stokes equations without the Hele–Shaw approximations will be

developed. The purpose of developing the GN model is to compare the approach used in this model with that of the GHS model. Due to the restrictions of the GN model a one–dimensional plane flow problem is used for the comparisons. The governing equations used in the GN model will also be discretized with a finite volume method. The two–dimensional calculational plane, lying in the x–y plane, is a section through the thickness of the above–mentioned cavity. The set of discretized equations will be solved using the PISO algorithm. To achieve the objective of comparing the approaches used in the GHS and GN models, the same constitutive equations, generalized to non–Newtonian materials, and the same finite volume method as in the GHS model will be used in the GN model. The comparisons will be done without including the movement of the flow front in the numerical models. The modelling of the flow front used in the GHS model assumes that the flow front does not vary in the thickness direction since the pressures are constant through the thickness. In the GN model, the pressures are calculated as a function of the thickness direction and the velocities are solved simultaneously with the pressures. Therefore the same modelling of the flow front as used in the GHS model cannot be incorporated in the GN model which does not include the Hele–Shaw approximations. Since the objective is to compare the two models within the same framework, flow without the movement of the flow front is considered. The fundamental solution method used in the GHS method does not change if the flow front is not included in this model. Therefore continuous flow through a cavity with an open outlet is simulated to achieve the objective of comparing the approaches used in the two models and to determine the effect of the Hele–Shaw approximations.

The influence of the Hele–Shaw approximations will be determined by first comparing steady–state solutions obtained with the GHS and GN models for continuous flow through a cavity with an open outlet. Although a steady–state solution does not represent the actual flow in

the cavity, it can be used to confirm the compatibility of specific features of the GHS and GN models.

Transient solutions obtained with the two models will be compared to determine the influence of the Hele–Shaw approximations on the time–dependent pressure development for two specific flow cases. The influence on the other variables will be determined by comparing the results at a time equal to the filling time of the cavity. The difference in the results obtained with the two models is an indication of the influence of the Hele–Shaw approximations on the solutions of these two flow cases. Parametric studies will also be done to compare the solutions of the GHS and GN models for a wider range of flow cases.

Once the objective of determining the effect of the Hele–Shaw approximations has been achieved, the simulation of the injection moulding process will be demonstrated using the GHS model. Firstly, a one–dimensional flow case is simulated to demonstrate the filling stage with movement of the flow front and the post–filling stage with packing and cooling. For this purpose the constitutive equations in the GHS model will be refined to represent the material characteristics more accurately during the post–filling stage. The effect of the specified holding pressure on the pressure development during the post–filling stage will also be shown. A refinement to include both the solid and liquid phase densities was developed for the GHS model as reported in the literature. Since the Hele–Shaw approximations are not included in the GN model, the refinement could not be incorporated in this model. The refinement described here therefore has had to be left out of the GHS model used in the comparisons described above. Secondly, the simulation of a two–dimensional flow case will be demonstrated. For this purpose an injection moulded part with a single sprue gate as inlet will be considered.

1.4 Layout of the rest of the thesis

In **chapter 2** the Hele–Shaw formulation of the governing equations is derived for polymer melts. The governing equations of the generalized Hele–Shaw (GHS) model are discretized in a two–dimensional Cartesian coordinate system using a finite volume approach. Solution algorithms are given and the modelling of the filling and post–filling stages are demonstrated with example calculations.

A generalized Newtonian (GN) model for solving the two–dimensional Navier–Stokes equations is developed in **chapter 3** for the purpose of comparing it with the GHS model. The governing equations, which include the full momentum equations, are discretized with a finite volume method in a two–dimensional Cartesian coordinate system. The solution of the set of discretized equations using the PISO algorithm is described.

In **chapter 4** the GHS and GN models, using the different approaches described in the previous chapters, are compared to determine the influence of the Hele–Shaw approximations. For this purpose two specific flow cases, i.e. flow through a cavity with an open outlet and the flow in the post–filling stage, are considered. The steady–state solutions of the first flow case are obtained to determine the compatibility of specific features of the two models. The transient solutions are compared to determine the influence of the Hele–Shaw approximations on the solutions of these two flow cases. Parametric studies are done to compare the solutions of the GHS and GN models for a wider range of flow cases.

The constitutive equations are refined in **chapter 5** and incorporated in the GHS model. The refined GHS model is used to represent the material characteristics more accurately during the post–filling stage. Both the solid and liquid phase densities are included, one–dimensional heat transfer during cooling is calculated and the increased temperature

sensitivity of the viscosity at low temperatures is taken into account. The examples treated in this chapter are the simulation of one–dimensional flow with movement of the flow front in the filling stage, a comparison of the solutions of the post–filling stage using two viscosity models, and the simulation of a two–dimensional flow case.

Chapter 6 is the closure in which the conclusions reached in this study are discussed. Further work that can be done in this research area is also discussed briefly.

CHAPTER 2

2 A NUMERICAL MODEL USING THE HELE–SHAW FORMULATION

2.1 Introduction

In this chapter the theoretical background is given for a numerical model using the Hele–Shaw formulation. The simulation model described in this chapter is a generalized Hele–Shaw (GHS) model since it extends classical Hele–Shaw flow to non–Newtonian fluids under non–isothermal conditions. A finite volume approach is used in the discretization process as compared to finite elements used in most other Hele–Shaw based numerical models reported in the literature. The finite volume approach is easier to apply than finite elements since the discretized equations are less complex.

The Hele–Shaw formulation of the goveroning equations is derived for polymer melts which are weakly compressible. A non–dimensional form of these equations is also derived. Modelling of the movement of the flow front in the filling stage is included. Since other researchers assume incompressibility in the filling stage the simplified equations for constant density are also given. Simplifications of the governing equations reported in the literature are discussed.

The discretization of the governing equations in a two–dimensional Cartesian coordinate system with a fixed grid is explained. The solution algorithms for different flow cases are given.

To enhance understanding of the numerical model and for the purpose of comparisons, constitutive equations which are computationally simple are employed in this model. Example calculations of the filling– and post–filling stages and of continuous flow through a cavity with an open outlet are given to demonstrate results obtained with the GHS model.

2.2 Governing equations

Anderson et al. (1984) describe a general deformation law which relates the stress tensor to the pressure, p, and the velocity components in a Newtonian fluid. They give this relationship in compact tensor notation as follows :

$$\Pi_{ij} = -p\delta_{ij} + \mu \left(\frac{\partial u_i}{\partial x_j} + \frac{\partial u_j}{\partial x_i}\right) + \mu' \frac{\partial u_k}{\partial x_k} \delta_{ij} \quad (i,j = 1,2,3) , \quad (2.1)$$

where Π_{ij} is the stress tensor; δ_{ij} is the Kronecker delta, defined by $\delta_{ij} = 1$ if $i = j$ and $\delta_{ij} = 0$ if $i \neq j$; u_1, u_2 and u_3 are the components of the velocity vector; x_1, x_2 and x_3 are the components of the position vector; μ is the coefficient of viscosity and μ' is the second coefficient of viscosity. Here and henceforth the summation convention for repeated indices is used. The two coefficients of viscosity are related to the coefficient of bulk viscosity (κ) by the expression

$$\kappa = \frac{2}{3}\cdot\mu + \mu' . \quad (2.2)$$

κ is negligible except in the study of the structure of shock waves and in the absorption and attenuation of accoustic waves (Anderson et al., 1984). Consequently, since shock waves are not present, $\kappa = 0$ and the second coefficient of viscosity becomes

$$\mu' = -\frac{2}{3}\cdot\mu \quad (2.3)$$

and the stress tensor is written as

$$\Pi_{ij} = -p\delta_{ij} + \mu \left[\left(\frac{\partial u_i}{\partial x_j} + \frac{\partial u_j}{\partial x_i}\right) - \frac{2}{3} \frac{\partial u_k}{\partial x_k} \delta_{ij}\right] \quad (i,j = 1,2,3). \quad (2.4)$$

The stress tensor can also be separated by writing

$$\Pi_{ij} = - p\delta_{ij} + \tau_{ij} \ , \tag{2.5}$$

where τ_{ij} is the viscous stress tensor which, in a Cartesian coordinate system, can be written as a set of scalar equations :

$$\tau_{xx} = \frac{2}{3} \mu \left(2\frac{\partial u}{\partial x} - \frac{\partial v}{\partial y} - \frac{\partial w}{\partial z}\right) \tag{2.6}$$

and

$$\tau_{xy} = \mu \left(\frac{\partial u}{\partial y} + \frac{\partial v}{\partial x}\right) = \tau_{yx} \ , \tag{2.7}$$

with similar equations for τ_{yy}, τ_{zz} and τ_{xz} and τ_{yz}.

In a Cartesian coordinate system, after substituting the stress in the momentum and energy equations, the three–dimensional Navier–Stokes equations can be expressed as the following system of scalar equations (Anderson et al., 1984) :

Continuity equation

$$\frac{\partial \rho}{\partial t} + \frac{\partial}{\partial x} (\rho u) + \frac{\partial}{\partial y} (\rho v) + \frac{\partial}{\partial z} (\rho w) = 0 \ . \tag{2.8}$$

Momentum equations

$$\frac{\partial}{\partial t} (\rho u) + \frac{\partial}{\partial x} (\rho u^2) + \frac{\partial}{\partial y} (\rho uv) + \frac{\partial}{\partial z} (\rho uw)$$

$$= - \frac{\partial p}{\partial x} + \frac{\partial}{\partial x} \left[\frac{2}{3} \mu \left(2 \frac{\partial u}{\partial x} - \frac{\partial v}{\partial y} - \frac{\partial w}{\partial z}\right)\right] + \frac{\partial}{\partial y} \left[\mu \left(\frac{\partial u}{\partial y} + \frac{\partial v}{\partial x}\right)\right]$$

$$+ \frac{\partial}{\partial z} \left[\mu \left(\frac{\partial w}{\partial x} + \frac{\partial u}{\partial z}\right)\right] + \rho f_x \ , \tag{2.9a}$$

$$\frac{\partial}{\partial t}(\rho v) + \frac{\partial}{\partial x}(\rho uv) + \frac{\partial}{\partial y}(\rho v^2) + \frac{\partial}{\partial z}(\rho vw)$$

$$= -\frac{\partial p}{\partial y} + \frac{\partial}{\partial x}\left[\mu\left(\frac{\partial v}{\partial x} + \frac{\partial u}{\partial y}\right)\right] + \frac{\partial}{\partial y}\left[\frac{2}{3}\mu\left(2\frac{\partial u}{\partial y} - \frac{\partial u}{\partial x} - \frac{\partial w}{\partial z}\right)\right]$$

$$+ \frac{\partial}{\partial z}\left[\mu\left(\frac{\partial v}{\partial z} + \frac{\partial w}{\partial y}\right)\right] + \rho f_y \,, \qquad (2.9b)$$

$$\frac{\partial}{\partial t}(\rho w) + \frac{\partial}{\partial x}(\rho uw) + \frac{\partial}{\partial y}(\rho vw) + \frac{\partial}{\partial z}(\rho w^2)$$

$$= -\frac{\partial p}{\partial z} + \frac{\partial}{\partial x}\left[\mu\left(\frac{\partial w}{\partial x} + \frac{\partial u}{\partial z}\right)\right] + \frac{\partial}{\partial y}\left[\mu\left(\frac{\partial v}{\partial z} - \frac{\partial w}{\partial y}\right)\right]$$

$$+ \frac{\partial}{\partial z}\left[\frac{2}{3}\mu\left(2\frac{\partial w}{\partial z} - \frac{\partial u}{\partial x} - \frac{\partial v}{\partial y}\right)\right] + \rho f_z \,. \qquad (2.9c)$$

Energy equation

$$c_p\frac{\partial}{\partial t}(\rho T) + c_p\frac{\partial}{\partial x}(\rho uT) + c_p\frac{\partial}{\partial y}(\rho vT) + c_p\frac{\partial}{\partial z}(\rho wT)$$

$$-\left[\frac{\partial p}{\partial t} + \frac{\partial}{\partial x}(up) + \frac{\partial}{\partial y}(vp) + \frac{\partial}{\partial z}(wp)\right]$$

$$= \frac{\partial}{\partial x}\left(k\frac{\partial T}{\partial x}\right) + \frac{\partial}{\partial y}\left(k\frac{\partial T}{\partial y}\right) + \frac{\partial}{\partial z}\left(k\frac{\partial T}{\partial z}\right) + SS \,. \qquad (2.10)$$

If the coefficient of bulk viscosity, κ, is ignored, as described above, the dissipation function, SS, becomes

$$SS = \mu\left[2\left(\frac{\partial u}{\partial x}\right)^2 + 2\left(\frac{\partial v}{\partial y}\right)^2 + 2\left(\frac{\partial w}{\partial z}\right)^2 + \left(\frac{\partial v}{\partial x} + \frac{\partial u}{\partial y}\right)^2\right.$$

$$\left. + \left(\frac{\partial w}{\partial y} + \frac{\partial v}{\partial z}\right)^2 + \left(\frac{\partial u}{\partial z} + \frac{\partial w}{\partial x}\right)^2 - \frac{2}{3}\left(\frac{\partial u}{\partial x} + \frac{\partial v}{\partial y} + \frac{\partial w}{\partial z}\right)^2\right] \,. \qquad (2.11)$$

The governing equations are generalized to non–Newtonian fluids (Hieber & Shen, 1980) by replacing the Newtonian viscosity, μ, with a non–Newtonian viscosity, η, which depends on the pressure, temperature and shear rate. Using the Hele–Shaw approximations, these equations are simplified in section 2.2.1, resulting in the generalized Hele–Shaw (GHS) numerical model.

2.2.1 Weakly compressible flow

Weakly compressible flow can be defined as flow in which no shock waves occur and in which changes in density are small compared to density changes in flow cases which are defined as compressible.

Consider a thin cavity with the origin of the coordinate system on the plane of symmetry as shown in Figure 2.1. The polymer melt flows between two parallel plates or fixed walls which are both parallel to the x–z plane. The y direction, is the gap–wise or thickness direction. We define b as the constant half–gap dimension such that $y = \pm b$ at the fixed walls.

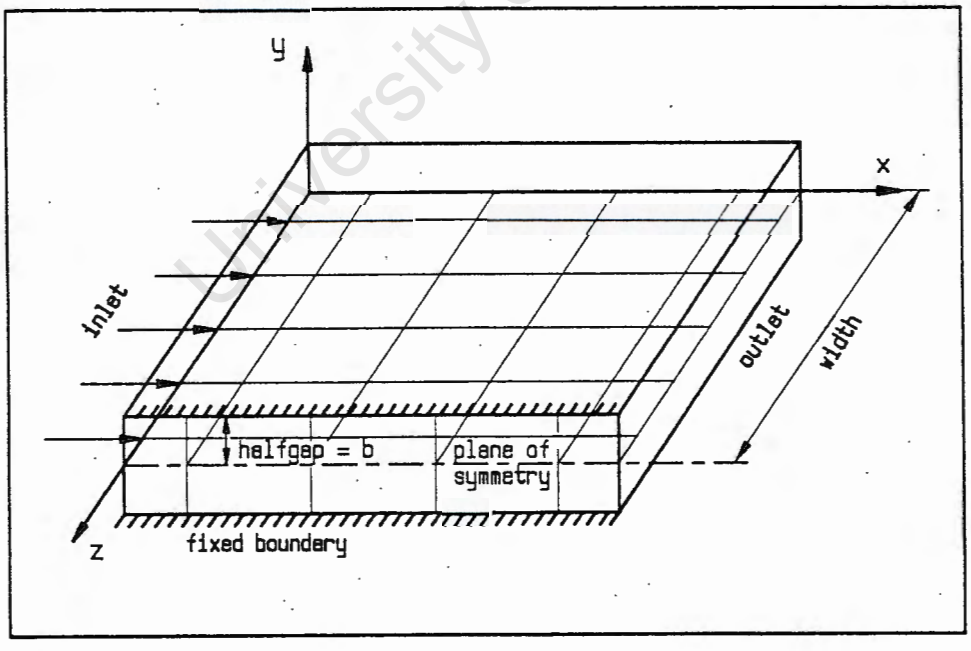

FIGURE 2.1 Cartesian coordinate system and calculational plane

The continuity and momentum equations can be simplified using the Hele–Shaw approximations (Schlichting, 1968) and approximations which are appropriate for thin geometries and highly viscous fluids :

a) the velocity component in the y direction is negligible;
b) pressure is a function of x and z only;
c) inertial forces are negligible compared to the viscous forces;
d) the velocity gradients in the x and z directions are negligible compared to the velocity gradients in the y direction.

The **momentum equations** (2.9) therefore reduce to

$$\frac{\partial p}{\partial x} = \frac{\partial}{\partial y}\left(\eta \frac{\partial u}{\partial y}\right) , \tag{2.12}$$

$$\frac{\partial p}{\partial z} = \frac{\partial}{\partial y}\left(\eta \frac{\partial w}{\partial y}\right) , \tag{2.13}$$

and

$$\frac{\partial p}{\partial y} = 0 . \tag{2.14}$$

Since p is independent of y and the velocity can be assumed to be symmetric with respect to y, equations (2.12) and (2.13) may be integrated to give, respectively,

$$y \frac{\partial p}{\partial x} = \eta \frac{\partial u}{\partial y} \tag{2.15}$$

and

$$y \frac{\partial p}{\partial z} = \eta \frac{\partial w}{\partial y} . \tag{2.16}$$

Another integration of (2.15) gives

$$u(y) = \int_0^y \frac{\partial p}{\partial x} \cdot \frac{\xi}{\eta} \, d\xi + u_0 , \tag{2.17}$$

where u_0 is the velocity at the plane of symmetry $y = 0$. Here and henceforth the dependence of velocity on x and z is not indicated explicitly, for convenience.

For a non–slip boundary condition the velocity is zero at the fixed boundary $y = b$, giving

$$u(b) = \frac{\partial p}{\partial x} \int_0^b \frac{\xi}{\eta} \, d\xi + u_0 = 0 . \tag{2.18}$$

Therefore $$u_0 = - \frac{\partial p}{\partial x} \int_0^b \frac{\xi}{\eta} \, d\xi . \tag{2.19}$$

Substitution of (2.19) into (2.17) gives

$$u(y) = - \frac{\partial p}{\partial x} \int_y^b \frac{\xi}{\eta} \, d\xi . \tag{2.20}$$

Similarly $$w(y) = - \frac{\partial p}{\partial z} \int_y^b \frac{\xi}{\eta} \, d\xi . \tag{2.21}$$

Equations (2.20) and (2.21) are used to calculate the velocity profiles through the thickness at any point on the x–z plane after the pressure, which is the primary variable, has been determined.

By neglecting the velocity, v, in the y direction, the **continuity equation** (2.8) reduces to

$$\frac{\partial \rho}{\partial t} + \frac{\partial}{\partial x} (\rho u) + \frac{\partial}{\partial z} (\rho w) = 0 . \tag{2.22}$$

To solve for the pressure, equation (2.22) is first written in terms of the

average density through the thickness, $\bar{\rho}$, and the thickness averaged density times velocity i.e. $\overline{\rho u}$ and $\overline{\rho w}$. These thickness averaged variables are defined by

$$\bar{\rho} = \frac{1}{b} \int_0^b \rho \, dy \, , \tag{2.23a}$$

$$\overline{\rho u} = \frac{1}{b} \int_0^b (\rho u) \, dy \, , \tag{2.23b}$$

$$\overline{\rho w} = \frac{1}{b} \int_0^b (\rho w) \, dy \, . \tag{2.23c}$$

Integration of (2.22) across the half gap and the use of equations (2.23) gives the thickness averaged continuity equation

$$\frac{\partial}{\partial t} (\bar{\rho} b) + \frac{\partial}{\partial x} (b\overline{\rho u}) + \frac{\partial}{\partial z} (b\overline{\rho w}) = 0 \, . \tag{2.24}$$

Substitution of (2.20) into (2.23b) gives

$$b\overline{\rho u} = - \frac{\partial p}{\partial x} \int_0^b \rho \, (\int_y^b \frac{\xi}{\eta} \, d\xi) \, dy$$

$$= - \tilde{S} \frac{\partial p}{\partial x} \, , \tag{2.25}$$

where $$\tilde{S} = \int_0^b \rho \, (\int_y^b \frac{\xi}{\eta} \, d\xi) \, dy \, . \tag{2.26}$$

Similarly $$b\overline{\rho w} = - \tilde{S} \frac{\partial p}{\partial z} \, . \tag{2.27}$$

Substitution of (2.25) and (2.27) into (2.24) gives (similar to Chiang et al., 1991a) :

$$\frac{\partial}{\partial t}(\bar{\rho}b) - \frac{\partial}{\partial x}\left(\tilde{S}\frac{\partial p}{\partial x}\right) - \frac{\partial}{\partial z}\left(\tilde{S}\frac{\partial p}{\partial z}\right) = 0 \,, \qquad (2.28)$$

which is the governing equation used to solve for the pressures.

In order to derive a non–dimensional form of equation (2.28), the following dimensionless variables are defined :

$$\bar{\bar{x}} = \frac{x}{L} \,, \quad \bar{\bar{y}} = \frac{y}{L} \,, \quad \bar{\bar{z}} = \frac{z}{L} \,, \qquad (2.29a,b,c)$$

$$\bar{\bar{u}} = \frac{u}{U} \,, \quad \bar{\bar{w}} = \frac{w}{U} \,, \qquad (2.30a,b,c)$$

$$\bar{\bar{p}} = \frac{p}{\rho_c U^2} \,, \quad \bar{\bar{\eta}} = \frac{\eta}{\eta_0} \,, \quad \bar{\bar{\rho}} = \frac{\rho}{\rho_c} \,, \quad \bar{\bar{\bar{\rho}}} = \frac{\bar{\rho}}{\rho_c} \,, \qquad (2.31a,b,c,d)$$

$$\bar{\bar{t}} = \frac{tU}{L} \,. \qquad (2.32)$$

Here L is a characteristic length, U is a characteristic velocity and ρ_c is the constant melt density. The Newtonian base value of the viscosity, η_0, is the viscosity at zero shear rate, atmospheric pressure and at a reference melt temperature. In this case we choose the melt temperature to be 100°C above the glass transition temperature. The half–gap dimension, b, in the y direction is chosen as characteristic length and the inlet velocity as the characteristic velocity. The Reynolds number is defined by

$$R_e = \frac{Ub\rho_c}{\eta_0} \,. \qquad (2.33)$$

The dimensionless variables are introduced into equations (2.26) and (2.28) by substitution to give

$$\tilde{S} = b^3 \rho_c \int_0^1 \bar{\bar{\rho}} \left(\frac{1}{\eta_0}\int_{\bar{y}}^1 \bar{\bar{\xi}}/\bar{\bar{\eta}}\, d\bar{\bar{\xi}}\right) d\bar{\bar{y}} , \tag{2.34}$$

which can be rewritten as

$$\tilde{S} = \frac{b^3\rho_c}{\eta_0}\cdot\bar{\bar{S}} , \tag{2.35}$$

or $$\tilde{S} = \frac{b^2 R_e}{U}\cdot\bar{\bar{S}} , \tag{2.36}$$

where $$\bar{\bar{S}} = \int_0^1 \bar{\bar{\rho}} \left(\int_{\bar{y}}^1 \bar{\bar{\xi}}/\bar{\bar{\eta}}\, d\bar{\bar{\xi}}\right) d\bar{\bar{y}} . \tag{2.37}$$

After rearrangement, equation (2.28) becomes

$$\frac{\partial}{\partial \bar{\bar{t}}}(\bar{\bar{\rho}}) - \frac{\partial}{\partial \bar{\bar{x}}}\left(\bar{\bar{S}}\frac{\partial \bar{\bar{p}}}{\partial \bar{\bar{x}}}\right)\cdot R_e - \frac{\partial}{\partial \bar{\bar{z}}}\left(\bar{\bar{S}}\frac{\partial \bar{\bar{p}}}{\partial \bar{\bar{z}}}\right)\cdot R_e = 0 . \tag{2.38}$$

Because of the particular form of the constitutive equations, which will be discussed in section 2.4.2, an additional constant is introduced alongside the Reynolds number. This constant, $\bar{\bar{\tau}}^*$, is the dimensionless form of the constant, τ^*, which is used in the Cross model, equation (1.10). This equation can be written in non–dimensional form as

$$\bar{\bar{\eta}} = \frac{\eta}{\eta_0} = \frac{1}{1 + [\bar{\bar{\gamma}}/(\bar{\bar{\tau}}^* R_e)]^{1-n}} , \tag{2.39}$$

where $$\bar{\dot{\gamma}} = \frac{\dot{\gamma} b}{U} , \tag{2.40}$$

and $$\bar{\tau}^* = \frac{\tau^*}{\rho_c U^2} . \tag{2.41}$$

Therefore, when the Cross model is used as constitutive equation, there are two parameters, R_e and $\bar{\tau}^*$, that define the problem as will be shown in chapter 4.

The **energy equation** is a simplification based on the thin–gap approximation (Hieber & Shen, 1980), which neglects thermal convection in the thickness direction and thermal conduction in the direction of flow. The velocity component, v, is neglected in two–dimensional flow. The velocity gradients in the x and z directions are negligible for Hele–Shaw flow and the thermal conductivity is assumed to be constant. After substitution of the continuity equation, the simplified **energy equation** (2.10) becomes

$$\rho c_p \left(\frac{\partial T}{\partial t} + u \frac{\partial T}{\partial x} + w \frac{\partial T}{\partial z}\right) - \left[\frac{\partial p}{\partial t} + \frac{\partial}{\partial x}(up) + \frac{\partial}{\partial z}(wp)\right]$$

$$= k \frac{\partial^2 T}{\partial y^2} + \eta \left[\left(\frac{\partial u}{\partial y}\right)^2 + \left(\frac{\partial w}{\partial y}\right)^2\right] . \tag{2.42}$$

For polymer materials the terms involving pressure can be neglected (Lafleur & Kamal, 1986) and the **energy equation** reduces to the formulation given by Wang and Hieber (1987) :

$$\rho c_p \left(\frac{\partial T}{\partial t} + u \frac{\partial T}{\partial x} + w \frac{\partial T}{\partial z}\right) = k \frac{\partial^2 T}{\partial y^2} + \eta \dot{\gamma}^2 , \tag{2.43}$$

where $\dot{\gamma}$, the shear rate, is defined by

$$\dot{\gamma} = \left[\left(\frac{\partial u}{\partial y}\right)^2 + \left(\frac{\partial w}{\partial y}\right)^2\right]^{1/2} . \tag{2.44}$$

The **movement of the flow front** is modelled similarly to the volume of fluid (VOF) method described by Hirt and Nichols (1981). The flow front is modelled with a continuity equation for the fractional volume of fluid, f, which is present in each control volume. This equation is derived by doing a mass balance. The total inflow into a control volume is equated to the change in the mass contained in the volume. The mass is given by $(f\overline{\rho})dxdz$ which is the product of the thickness averaged density, $\overline{\rho}$, the area, dxdz, and f, the fraction of the volume which is already filled. For a control volume the total inflow minus outflow in the x direction is

$$f\overline{\rho u}dz - [f\overline{\rho u}dz + \frac{\partial}{\partial x}(f\overline{\rho u}dz)dx] \ , \tag{2.45}$$

and the total inflow minus outflow in the z direction is

$$f\overline{\rho w}dx - [f\overline{\rho w}dx + \frac{\partial}{\partial z}(f\overline{\rho w}dx)dz] \ , \tag{2.46}$$

where $\overline{\rho u}$ and $\overline{\rho w}$ are given by (2.23b) and (2.23c).

Setting the sum of (2.45) and (2.46), which is the total flux for the volume, equal to the time derivative of the mass in the volume and dividing by the area dxdz we obtain the continuity equation

$$\frac{\partial(\overline{\rho}f)}{\partial t} + \frac{\partial(\overline{\rho u}f)}{\partial x} + \frac{\partial(\overline{\rho w}f)}{\partial z} = 0 \ . \tag{2.47}$$

To model the movement of the flow front, using equation (2.47), f is set equal to 0 at all the nodes except at the inlet where a fixed value of 1 is specified for f. A value of 1 indicates that the control volume is completely filled and a value of 0 indicates that it is empty. Therefore only the control volumes at the inlet are filled with polymer at time

$t = 0$. New values for f are calculated for each time–step. Values of f near the flow front are "smeared", i.e. they range between 0 and 1 over a number of control volumes in the flow direction. The points where f has a value of $^1/_2$ obtained by interpolating between nodes represent the position of the flow front. These points are required to solve for the pressures. In front of the flow front p will remain atmospheric. Behind the flow front p is solved from equation (2.28).

2.2.2 Incompressible flow

Several researchers (Wang & Hieber, 1988, Dupret & Vanderschuren, 1988, Kamal et al., 1988) reported that they assume incompressibility in the filling stage. Incompressible flow is modelled by setting ρ = constant in the continuity equation.

The **continuity equation** for incompressible flow is therefore given by

$$\frac{\partial u}{\partial x} + \frac{\partial w}{\partial z} = 0 \; . \tag{2.48}$$

In the case of constant density (ρ_0), $\tilde{S}$ in (2.28) reduces to $\rho_0 \cdot S$ where

$$S = \int_0^b \left(\int_y^b \frac{\xi}{\eta} \, d\xi \right) dy \tag{2.49}$$

and the governing equation for incompressible Hele–Shaw flow becomes

$$\frac{\partial}{\partial x} \left(S \frac{\partial p}{\partial x} \right) + \frac{\partial}{\partial z} \left(S \frac{\partial p}{\partial z} \right) = 0 \tag{2.50}$$

2.2.3 Simplifications

The governing equation (2.50), for incompressible Hele–Shaw flow, contains S, given by equation (2.49). Another expression for S, used by Hieber and Shen (1980), can be derived by first integrating by parts which gives

$$\int_0^b u\, dy = uy\Big|_0^b - \int_0^b y \left(\frac{\partial u}{\partial y}\right) dy . \tag{2.51}$$

Then, since u(b) = 0 for a non–slip boundary condition, the first term on the right–hand–side vanishes. After rewriting equation (2.15) as

$$\frac{\partial u}{\partial y} = \frac{\partial p}{\partial x}.\frac{y}{\eta} , \tag{2.52}$$

subsititution of (2.52) into (2.51) gives

$$\int_0^b u\, dy = -\int_0^b \frac{\partial p}{\partial x}.\frac{y^2}{\eta}\, dy , \tag{2.53}$$

or

$$b\bar{u} = -\frac{\partial p}{\partial x}\int_0^b \frac{y^2}{\eta}\, dy . \tag{2.54}$$

From (2.25), with $\rho = \rho_0$ and $\tilde{S} = \rho_0 \cdot S$ for incompressible flow ,

$$b\bar{u} = S\,\frac{\partial p}{\partial x} . \tag{2.55}$$

Subsitution of (2.55) into (2.54) gives

$$S = \int_0^b \frac{y^2}{\eta}\, dy . \tag{2.56}$$

Hieber and Shen (1980) have used equation (2.56) for incompressible Hele–Shaw flow. It will be shown, in section 2.8.2.3, that there is a slight deviation in the resulting velocity profiles, obtained with the GHS model developed in this thesis, if S is calculated with equation (2.56) as compared to (2.49). The deviation can be explained by examining the way in which the two versions of S are calculated in the numerical model and comparing it with the calculation of the velocity components.

Set $$I = \int_y^b \frac{\xi}{\eta}\, d\xi \,. \qquad (2.57)$$

Since I appears in equation (2.20) for u and in equation (2.49) for S these two variables will be compatible in the numerical model only if the same numerical integration method is used to solve for I in both equations. However, equation (2.56) cannot be integrated in the same way as (2.20) as will be shown in the next paragraph. Therefore S, calculated from (2.56) is not compatible with u and v. This incompatibility results in the deviation in the velocity profiles.

Equation (2.57) can be written as

$$I = \int_y^b \frac{\xi}{\eta}\, d\xi = \int_0^b \frac{\xi}{\eta}\, d\xi - \int_0^y \frac{\xi}{\eta}\, d\xi \,. \qquad (2.58)$$

Substitution of (2.19) into (2.58) results in

$$I = -(u_0 \,/\, \frac{\partial p}{\partial x}) - \Theta(y) \,, \qquad (2.59)$$

where $$\Theta(y) = \int_0^y \frac{\xi}{\eta}\, d\xi \,. \qquad (2.60)$$

Substitution of (2.59) into (2.49) and (2.20), respectively, gives

$$S = \int_0^b - [(u_0 / \frac{\partial p}{\partial x}) + \Theta(y)]\, dy \qquad (2.61)$$

and $$u_y = u_0 + \frac{\partial p}{\partial x} \cdot \Theta(y) \cdot \qquad (2.62)$$

The grid points in the thickness direction, shown in Figure 2.2, and the trapezoidal rule are used to numerically integrate equations (2.60) and (2.58). The integration of $\Theta(y)$, from which $u_i = u_0 + \frac{\partial p}{\partial x} \cdot \Theta_i$ can be calculated, results in

$$\Theta_1 = 0 \,, \qquad (2.63)$$

$$\Theta_2 = \Theta_1 \quad \text{(from boundary condition)}, \qquad (2.64)$$

$$\Theta_3 = \Theta_2 + \Delta y \cdot (\frac{y}{\eta})_{2+1/2} \qquad (2.65)$$

or $$\Theta_{i+1} = \Theta_i + \Delta y \cdot (\frac{y}{\eta})_{i+1/2} \quad \text{for } i = 2 \text{ to } n-2 \qquad (2.66)$$

and $$\Theta_n = \Theta_{n-1} + \frac{\Delta y}{2} \cdot (\frac{y}{\eta})_{n-1/2} \,, \qquad (2.67)$$

where the subscript i+1/2 indicates the position halfway between grid points i and i+1. The value of a variable at position i+1/2 is equal to the average of the values at grid points i and i+1.

At the fixed boundary $u_n = 0$, which gives

$$u_n = u_0 + \frac{\partial p}{\partial x} \cdot \Theta_n = 0 \,. \qquad (2.68)$$

Therefore $$u_0 = -\frac{\partial p}{\partial x}\cdot\Theta_n \ . \qquad (2.69)$$

In the integration of (2.61) to calculate S, the results of the integration of $\Theta(y)$ and equation (2.69) are used to give

$$S = \int_0^b \Theta \ dy - \int_0^b \Theta(y) \ dy$$

$$= b\ \Theta_n - \sum_{i=2}^{n-1} (\Theta_i\cdot\Delta y) \ . \qquad (2.70)$$

Integration of equation (2.56) using the trapezoidal rule results in

$$S = \sum_{i=2}^{n-1} (\frac{y^2}{\eta})_i\cdot\Delta y \ . \qquad (2.71)$$

S in equation (2.70) is therefore calculated in the same way as u whereas S in equation (2.71) is not.

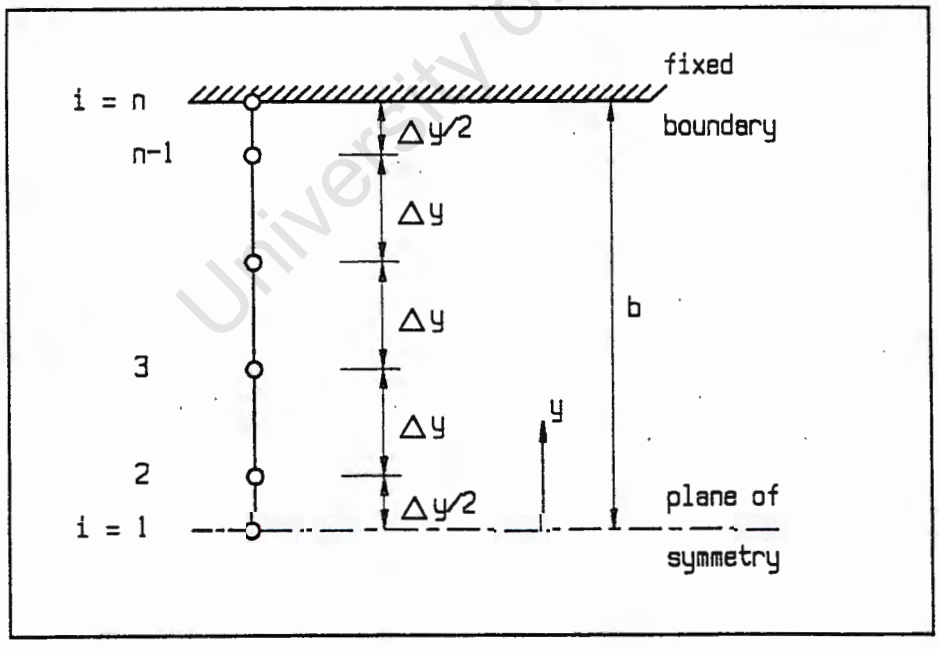

FIGURE 2.2 Grid points in the thickness direction

2.3 Discretization

In the finite volume approach the transport equations are integrated over a control volume or cell. In three dimensions any volume integral can be converted into surface integrals over the six faces of a cell (Bird et.al., 1960). Thus

$$\int\int\int_V \nabla\cdot\mathbf{f}\, dV = \int\int_A \mathbf{f}\cdot d\mathbf{A}\ , \tag{2.72}$$

which can be written as

$$\int_{A_e} f_e dA - \int_{A_w} f_w dA + \int_{A_n} f_n dA - \int_{A_s} f_s dA + \int_{A_t} f_t dA - \int_{A_b} f_b dA\ , \tag{2.73}$$

where, e.g. f_e is the component of f normal to the "e" face of the cell and A_e is the area of that cell face.

In two dimensions each control volume has only 4 faces or boundaries and the finite volume discretization involves the integration of each term in the governing equation using

$$\int_e^w \int_n^s (\text{term})\ dx\ dz\ , \tag{2.74}$$

where e, w, n, s refer to the four control volume boundaries.

A typical two–dimensional control volume and the centre points of its neighbours, as used in this chapter, are shown in Figure 2.3.

For the purpose of comparing the GHS model and the generalized Newtonian (GN) model ,which will be developed in chapter 3, we need

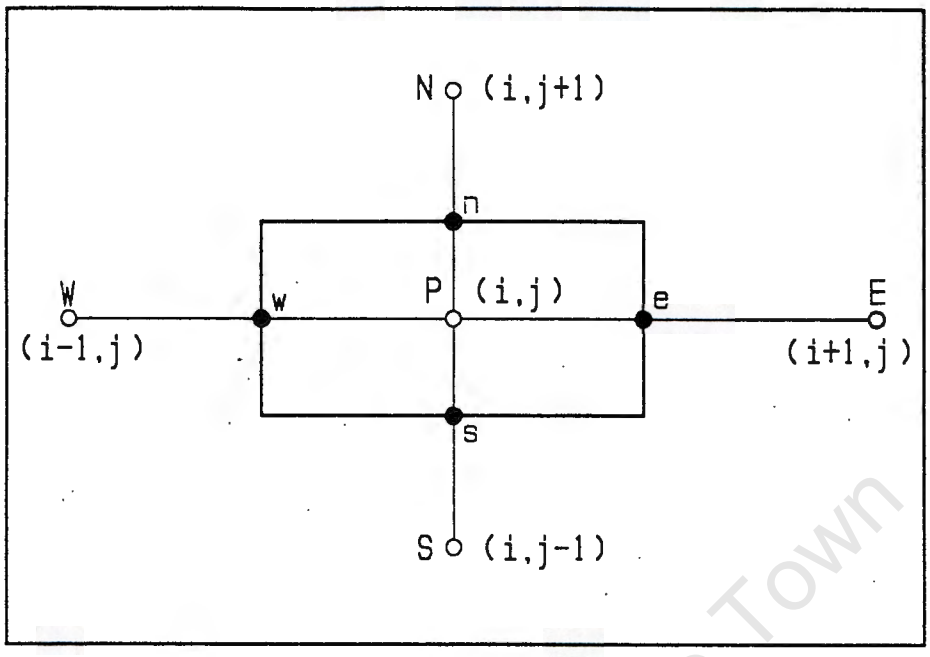

FIGURE 2.3 A typical control volume in the x–z plane where E, W, N and S are the centre points of its neighbours.

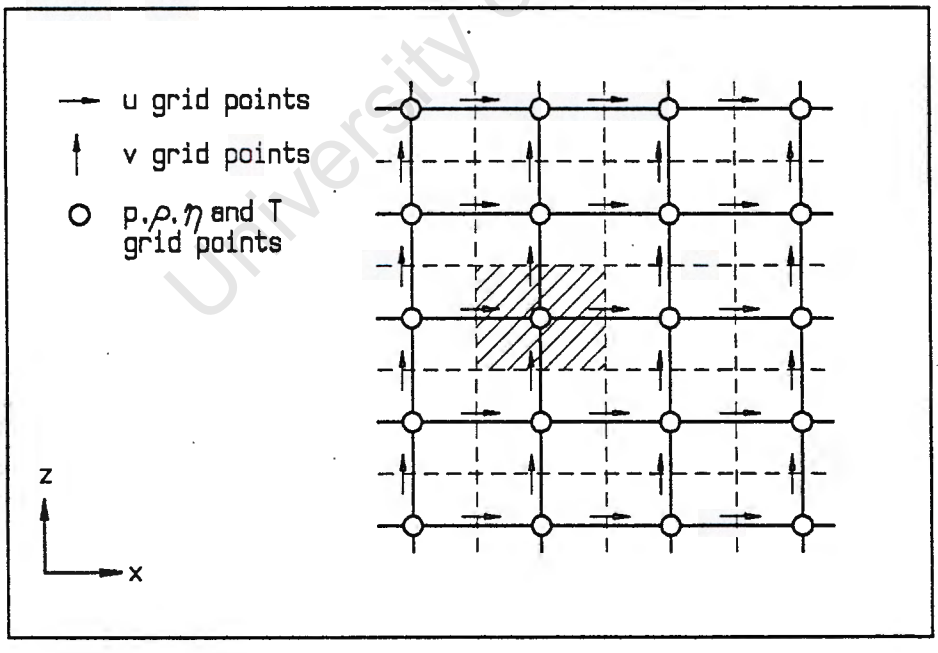

FIGURE 2.4 Two–dimensional grid used in the GHS model.

to calculate the pressures and velocities at corresponding positions on the grid. The GN model is discretized using a staggered grid as explained in section 3.3. We discretize the governing equation of the GHS model at the positions shown on the grid in Figure 2.4 to correspond with the staggered grid used for the GN model.

The governing equation (2.28) used to solve for the pressures is discretized as follows, where the subscripts refer to the positions shown in Figure 2.3 :

$$\Delta x \Delta z \cdot b \cdot \frac{(\bar{\rho}_P^{\,t} - \bar{\rho}_P^{\,t-1})}{\Delta t} - \Delta z \left[\tilde{S}_e \frac{(p_E - p_P)}{\Delta x_e} - \tilde{S}_w \frac{(p_P - p_W)}{\Delta x_w}\right]$$

$$- \Delta x \left[\tilde{S}_n \frac{(p_N - p_P)}{\Delta z_n} - \tilde{S}_s \frac{(p_P - p_S)}{\Delta z_s}\right] = 0 \,, \quad (2.75)$$

where
$$\tilde{S}_e = \tilde{S}_{i,j} \quad (2.76a)$$
$$\tilde{S}_w = \tilde{S}_{i-1,j} \quad (2.76b)$$
$$\tilde{S}_n = (\tilde{S}_{i,j} + \tilde{S}_{i,j+1} + \tilde{S}_{i-1,j} + \tilde{S}_{i-1,j+1})/4 \quad (2.76c)$$
$$\tilde{S}_s = (\tilde{S}_{i,j} + \tilde{S}_{i,j-1} + \tilde{S}_{i-1,j} + \tilde{S}_{i-1,j-1})/4 \,. \quad (2.76d)$$

The discretized equation is rewritten as

$$p_P a_P = p_E a_E + p_W a_W + p_N a_N + p_S a_S + S^p$$

$$= \Sigma\, p_{nb} a_{nb} + S^p, \quad (2.77)$$

where $$a_E = \overline{S}_e \frac{\Delta z}{\Delta x_e} \quad , \tag{2.78a}$$

$$a_W = \overline{S}_w \frac{\Delta z}{\Delta x_w} \quad , \tag{2.78b}$$

$$a_N = \overline{S}_n \frac{\Delta x}{\Delta z_n} \quad , \tag{2.78c}$$

$$a_S = \overline{S}_s \frac{\Delta x}{\Delta z_s} \quad , \tag{2.78d}$$

$$a_T = \frac{\Delta x \Delta z}{\Delta t} b \frac{\partial \overline{\rho}}{\partial p} \quad , \tag{2.78e}$$

$$a_P = a_E + a_W + a_N + a_S + a_T \quad , \tag{2.79}$$

and $$S^p = p_p^{t-1} a_T + \Delta x \Delta z \cdot b \cdot \frac{(\overline{T}_p^t - \overline{T}_p^{t-1})}{\Delta t} \cdot \frac{\partial \overline{\rho}}{\partial \overline{T}} \quad . \tag{2.80}$$

The energy equation (2.43) is also discretized with the finite volume method (Patankar, 1984) using a similar approach as above.

An implicit scheme is used to solve equation (2.77) which calculates the time–dependent pressure development. All the spatial derivative terms in equation (2.77) are evaluated at the current time level. The main advantage of using an implicit scheme is that it is numerically more stable than an explicit scheme (Güceri, 1989). Implicit schemes therefore allow larger time–steps. However, too large a time–step will produce an inaccurate solution even though the computations are stable.

An implicit scheme is also used to solve for the temperatures in the discretized energy equation (Patankar, 1984).

2.4 Constitutive equations

Since the purpose of developing the GHS and GN models in chapters 2 and 3 is to compare them in chapter 4, the same constitutive equations are used in the two models. The equation of state to calculate the density, as well as the viscosity model described here, have been chosen for their computational simplicity. This will enhance understanding of the numerical models. These constitutive equations are adequate for the purpose of comparing the GHS and GN models.

2.4.1 Equation of state

Although compressibility may be neglected to simplify the numerical model for the filling stage, compressibility effects greatly influence the post–filling stage. Since the same constitutive equations are used in the filling– and post–filling stages, compressibility is included in both stages.

The density of a polymer melt is both temperature– and pressure–dependent. To model this dependence, the Spencer–Gilmore equation has been chosen due to its computational simplicity :

$$(p + p')\left(\frac{1}{\rho} - \frac{1}{\rho'}\right) = R'T \ , \qquad (2.81)$$

where p', ρ' and R' are constants for a given material. The constants for polystyrene (PS) reported by Hieber et al., (1986) are :

$$p' = 1{,}86 \times 10^8 \quad \text{Nm/kg}$$
$$\rho' = 1{,}22 \times 10^3 \quad \text{kg/m}^3$$
$$R' = 80{,}0 \quad \text{Nm/kg°K}$$

2.4.2 Viscosity model

Materials of which the viscosity decreases with increasing shear rate are termed pseudoplastic or shear–thinning (Kamal & Ryan, 1989). Virtually all polymer melts exhibit shear–thinning behaviour which can be modelled with the 5–constant Cross model :

$$\eta = \frac{\eta_0}{1 + [\eta_0 \dot{\gamma}/\tau^*]^{1-n}} , \qquad (2.82)$$

where $$\eta_0 = \beta \exp\left(\frac{T_b}{T}\right)\exp(\beta p) . \qquad (2.83)$$

The five constants reported for PS by Chiang et al. (1991b) are :

$n = 0{,}274$

$\tau^* = 2{,}31 \times 10^4$ Pa

$B = 3{,}04 \times 10^{-9}$ Pa.s

$T_b = 13300$ °K

$\beta = 3{,}5 \times 10^{-8}$ Pa^{-1}

For the purposes of this chapter the same constants are used for all the flow cases.

2.4.3 Cooling

During both the filling and post–filling stages of injection moulding the mould wall, which is at a lower temperature than the polymer melt, cools the polymer down. Since the filling stage is completed in a much shorter time than the post–filling stage, the change in the temperatures

in the melt is less pronounced during filling. Even with wall temperatures lower than T_g, the polymer melt will not reach temperatures as low as T_g during the filling stage, except for a very thin layer at the wall or fixed boundary. During the filling stage the polymer is therefore assumed to be in the liquid phase throughout the domain. The equation of state, equation (2.81), and the viscosity model equation (2.82), which are only valid for temperatures above T_g, are therefore adequate for the purpose of developing the GHS and GN numerical models for the filling stage.

For the purposes of this chapter the constant wall temperature at the fixed boundary is specified to be just above T_g for the filling and post–filling stages. This enables us to use the same equation of state and viscosity model for both stages. Furthermore the results obtained by using a wall temperature above T_g are adequate for the purpose of comparing the GHS and GN models.

2.5 Boundary conditions

Since a finite volume approach is used to discretize the governing equation, the primary variable, p, is solved at interior nodes only. Therefore boundary conditions are required to specify the value of p at the boundaries. Since the velocities are derived from p, the values of the velocities at the boundaries will depend on the boundary conditions specified for p except at the inlet where either a constant flow rate or a constant pressure is specified. The other variables are either calculated or specified at the boundaries. The boundary conditions for the filling– and post–filling stages are discussed seperately in the following sections.

2.5.1 Filling stage

Referring to Figure 2.5, the following boundary conditions are specified for the pressure, p, during the filling stage. At the inlet boundary a zero normal gradient is specified for the pressure since the constant inflow is specified at the centre of each control volume at the inlet

which coincides with the first node away from the inlet boundary. At the closed outlet boundary and at all the nodes ahead of the flow front atmospheric pressure is specified. Zero normal pressure gradients are specified at the boundaries in the z direction. This means that there is no flow across the fixed boundary or across the x–y plane of symmetry and that a perfect slip boundary condition is assumed for u at the fixed boundary.

The slip boundary condition at the fixed boundary in the z direction is chosen since, due to the restrictions of the generalized Newtonian model described in the next chapter, a one–dimensional plane flow problem is used for the comparisons. In the derivation of equations (2.20) and (2.21) for the velocity components a non–slip boundary condition is assumed at the fixed boundary in the y direction. Therefore the velocity components at this boundary are specified to be zero . At the x–z plane of symmetry a zero normal gradient is specified for u and w.

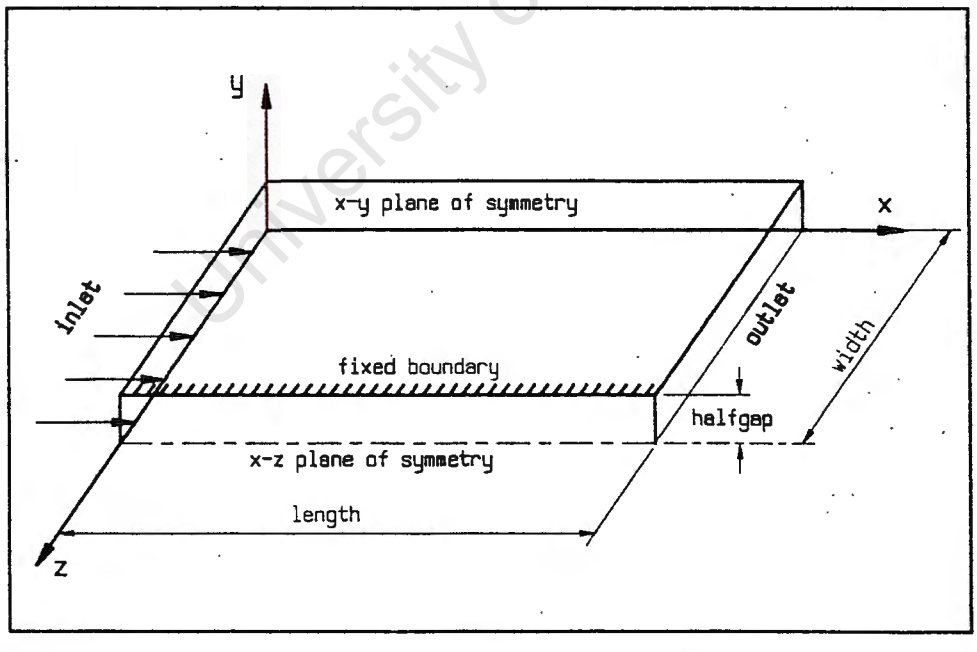

FIGURE 2.5 The boundaries of the cavity.

The boundary conditions for the pressure are incorporated in the discretized governing equation (2.77) as follows. A zero gradient inlet boundary condition is obtained by setting a_W equal to zero for the control volumes at the inlet. The constant inflow is incorporated in (2.77) by adding ρq to $p_P^{t-1}a_T$ in the source term, S^P, where q is the rate of inflow into each control volume at the inlet. The atmospheric pressure specified at the nodes ahead of the flow front and at the outlet boundary is automatically incorporated in (2.77) through the term $p_E a_E$.

Boundary conditions are specified for the temperature, the viscosity and the density on the boundaries where these variables are not calculated. In the x and z directions, zero normal gradients are specified for the viscosity on all four boundaries. In the thickness or y direction no boundary condition is specified at the wall or fixed boundary, where the viscosity is calculated. At the x–z plane of symmetry a zero normal gradient boundary condition is specified. A zero normal gradient is also specified for the density at this plane of symmetry. At all the other boundaries the density is calculated. Zero normal gradients are specified for the temperature at the x–z plane of symmetry, the outlet and both boundaries in the z direction. A constant temperature equal to the temperature of the inflowing melt is specified at the inlet. At the fixed boundary in the y direction a constant temperature equal to the mould temperature is specified. Alternatively a heat transfer coefficient can be specified.

2.5.2 Post–filling stage

The boundary conditions for the pressure in the post–filling stage are not the same as for the filling stage. Referring to Figure 2.5 a constant pressure is specified at the inlet boundary and the corresponding flow rate is calculated. At the closed outlet boundary a zero normal pressure gradient is specified. This means that the pressures at the outlet nodes, which are atmospheric at the end of the filling stage, are

specified to be equal to the pressures at the centres of the control volumes at the outlet. The pressures at the closed outlet therefore increase with each time–step.

The specified holding pressure at the inlet nodes is incorporated in equation (2.77) through the term $p_W a_W$ when the pressures in the control volumes at the inlet are solved. The zero normal gradient outlet boundary condition for the pressure is incorporated in equation (2.77) by setting $a_E = 0$ and $a_P = a_W + a_N + a_S + a_T$ for the control volumes at the outlet.

Since the density depends on the pressure and the temperature, the same zero normal gradient boundary condition has to be specified for the density at the outlet boundary. At the inlet nodes the densities are calculated from the constant values of the holding pressure and the temperatures at these nodes. The other boundary conditions for the post–filling stage are the same as for the filling stage.

2.6 Initial values

2.6.1 Filling stage

The following initial values are specified for the filling stage. Throughout the domain the pressure is atmospheric, the velocity components are zero, the viscosity is set equal to a reference value and the density is equal to the melt density at atmospheric pressure. The temperatures are equal to the temperature of the inflowing melt except at the closed outlet and the fixed boundary where a constant wall temperature is specified. The value of the fractional volume of fluid, f, is zero for all the control volumes except those at the inlet where a value of 1 is specified.

2.6.2 Post–filling stage

The results obtained in the filling stage at the instant of complete filling of the cavity are used as initial values for the post–filling stage. These initial values include a pressure drop through the cavity. The inlet pressure at the instant of filling is used as the constant holding pressure for the post–filling stage. The post–filling stage is simulated until the pressures throughout the cavity are equal to this holding pressure. In practice a holding pressure which is higher than the inlet pressure may be required. In this case the higher value of the holding pressure is specified as the constant pressure at the inlet nodes.

2.7 Solution algorithms

The solution algorithm used in the GHS model will be discussed separately for the filling– and post–filling stages. For the purpose of comparing the GHS and GN models in chapter 4 the solution algorithm and boundary conditions for the case of continuous flow through a cavity with an open outlet will also be given.

The solutions of the three flow problems will be demonstrated in the example calculations in section 2.8. The flow of a polymer melt in a thin rectangular cavity is simulated. The dimensions of the cavity are shown in Figure 2.6. The cavity is fed from the reservoir through the inlet. Only the flow in the cavity, excluding the reservoir, is considered. Due to symmetry about the x–z and x–y planes only one quarter of the actual cavity need to be modelled as will be shown in Figures 2.7, 2.8 and 2.9 for the three flow cases. A grid with 20, 12 and 10 nodes in the x, y and z directions, respectively, is constructed over the domain.

2.7.1 Filling stage

The boundary conditions and initial values for the filling stage have been given in detail in sections 2.5.1 and 2.6.1. A quarter model of the geometry to be used in solving the filling stage is shown in Figure 2.7.

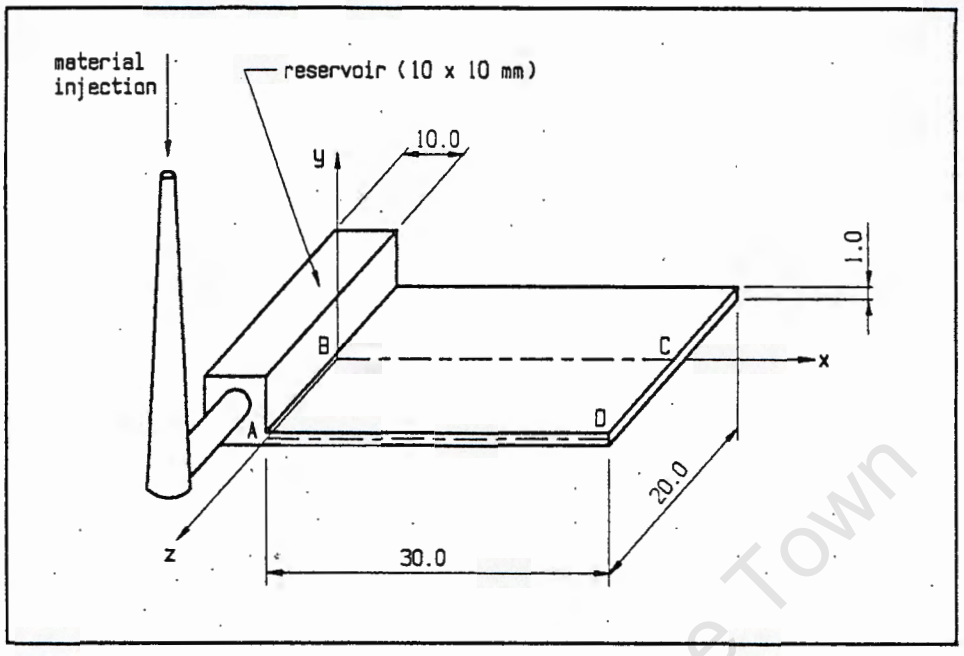

FIGURE 2.6 Geometry of the cavity for an injection moulded part.

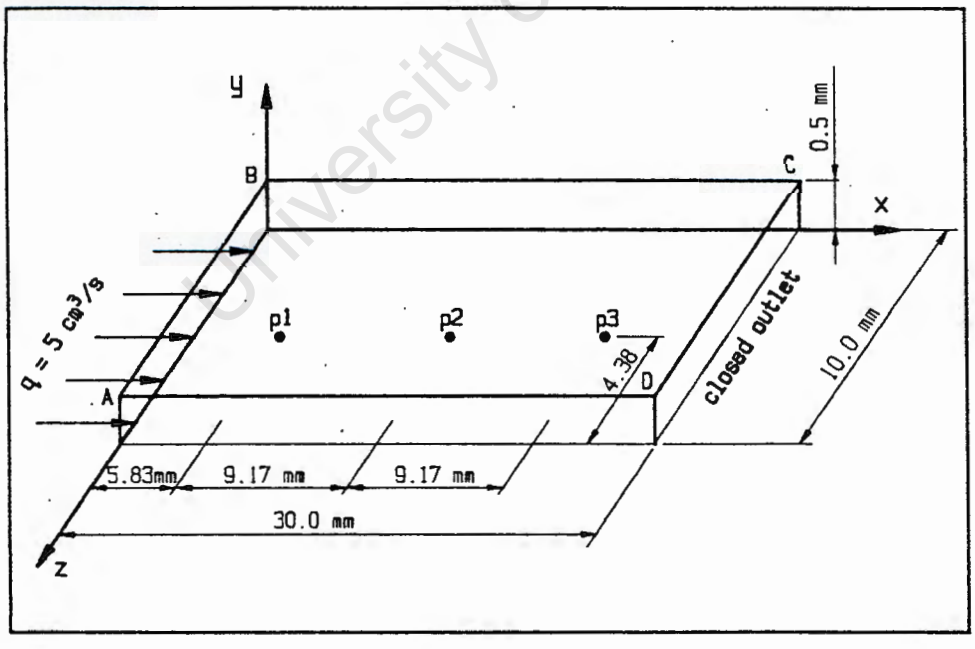

FIGURE 2.7 Dimensions of the model for the filling stage.

The solution algorithm used in the GHS model to obtain a solution of the filling stage can be summarized as follows :

(a) Calculate $\tilde{S}$ at each node from equation (2.26).
(b) Solve for the pressure field from equation (2.28).
(c) Calculate the velocity components, u and w, from equations (2.20) and (2.21).
(d) Solve for the temperatures from equation (2.43).
(e) Calculate the viscosities and densities in the three–dimensional grid using the viscosity model and equation of state in section 2.4.
(f) Calculate the position of the flow front from equation (2.47).
(g) Update the variables at the boundaries using the boundary conditions.
(h) Repeat steps (a) to (g) until a converged solution is obtained for the current time–level.
(i) Repeat the algorithm for the number of time–steps required to fill the cavity.

The solution of equation (2.47) in step (f) determines the position of the flow front and can be considered as a predictor step. Using steps (a) to (e) the pressures and the other variables are calculated at all the nodes behind the predicted flow front. These steps can be considered as corrector steps. Steps (a) to (g) of the solution algorithm are repeated for each time–step until a converged solution is obtained for that specific time–step. The calculations for a time–step are considered to be converged if the changes in the pressure field and the fractional volume of fluid, f, are smaller than the specified convergence criterion.

After each time–step the new position of the flow front is determined by calculating the position where $f = {}^1/_2$. The algorithm is repeated until the values of f at the nodes next to the closed outlet are greater than ${}^1/_2$ and the cavity is considered to be filled.

2.7.2 Continuous flow through a cavity with an open outlet

The movement of the flow front is not included in the GN model as explained in chapter 3. The case of continuous flow through a cavity with an open outlet (see Figure 2.8) is therefore considered for the purpose of comparing the GHS and GN models in chapter 4.

The boundary conditions are the same as for the filling stage except that, since there is no flow front, the pressure is specified to be atmospheric at the outlet nodes only.

Since there is no flow front in this case, the following initial values are specified. At time t_0=0 the cavity is completely filled with material which is stationary and the pressure throughout the domain is atmospheric. The temperatures at all the nodes except at the fixed boundary are equal to the temperature of the inflowing melt. The viscosity is set equal to a reference value and the density is equal to

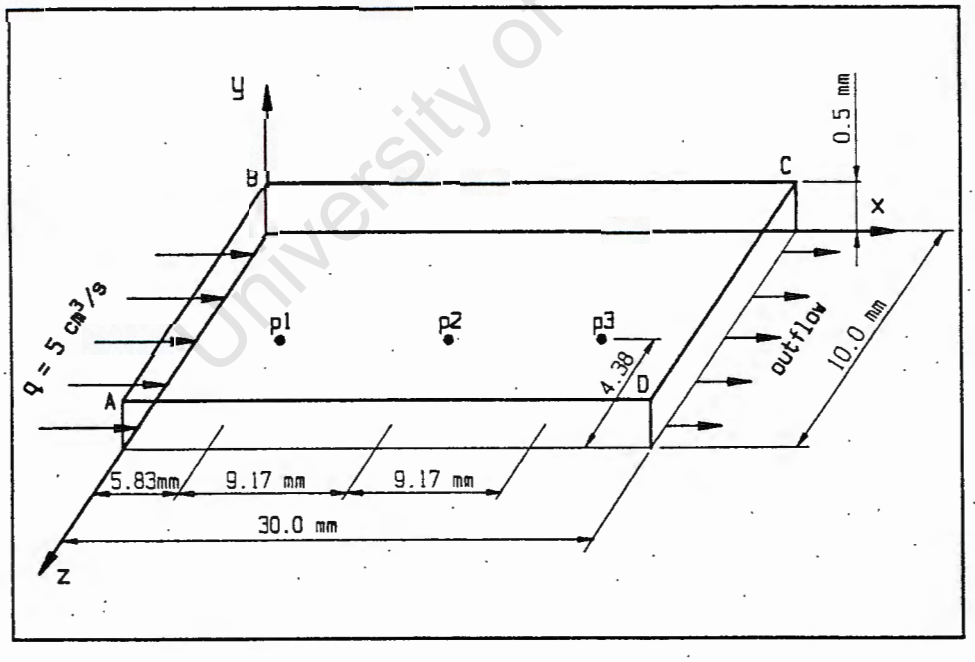

FIGURE 2.8 Geometry of the model for continuous flow through a cavity with an open outlet.

the melt density at atmospheric pressure. Since a constant flow rate is specified at the inlet, the melt in the cavity will increase gradually as from $t=t_0$. The similarity that exists between this flow case and the filling stage will be demonstrated with example calculations in section 2.8.2.2.

To determine the compatibility of specific features of the GHS and GN models in chapter 4 both a transient and a steady–state solution of this flow case will be used. Following are the solution algorithms, used in the GHS model, to obtain these two solutions.

2.7.2.1 Transient solution

The solution algorithm for a transient solution of flow through a cavity, without a flow front and for which a constant inlet velocity is specified, can be summarized as follows :

(a) Calculate $\tilde{S}$ at each node from equation (2.26).
(b) Solve for the pressure field from equation (2.28).
(c) Calculate the velocity components, u and w, from equations (2.20) and (2.21).
(d) Solve for the temperatures from equation (2.43).
(e) Calculate the viscosities and densities in the three–dimensional grid using the viscosity model and equation of state in section 2.4.
(f) Update the variables at the boundaries.
(g) Repeat steps (a) to (f) until a converged solution is obtained for the current time–level.
(h) Repeat for the required number of time–steps to obtain the solution after a specified period of time.

Steps (a) to (f) are repeated for each time–step until a converged solution is obtained for that specific time–step. The calculations for a time–step are considered to be converged if the fractional change in the pressure field is smaller than the specified convergence criterion.

2.7.2.2 Steady–state solution

The solution algorithm for the steady–state solution of continuous flow through a cavity can be summarized as follows :

(a) Calculate $\tilde{S}$ at each node from equation (2.26).
(b) Solve for the pressure field from equation (2.28), without including the time derivatives.
(c) Calculate the velocity components, u and w, from equations (2.20) and (2.21).
(d) Solve for the temperatures from equation (2.43), without the time derivatives.
(e) Calculate the viscosities and densities in the three–dimensional grid using the viscosity model and equation of state in section 2.4.
(f) Update the variables at the boundaries.
(g) Repeat steps (a) to (f) until the steady–state solution converges.

To obtain a steady–state solution, the GHS model is solved iteratively by neglecting the time derivatives in the governing equations (or by specifying an infinite time–step). The flow is therefore approximated as steady–state flow and the converged solution represents a picture of the flow in the cavity at an instant after infinite time has elapsed. Convergence is obtained by repeating steps (a) to (f) until the fractional change in the pressure field is smaller than the specified convergence criterion.

2.7.3 Post–filling stage

The boundary conditions and initial values for the post–filling stage have been given in detail in sections 2.5.2 and 2.6.2. The same geometry with a closed outlet, as for the filling stage, will be used in solving the post–filling stage. A quarter model of the geometry is shown in Figure 2.9 (p. 63).

The solution algorithm used to obtain the transient solution for the post–filling stage can be summarized as follows :

(a) Calculate $\tilde{S}$ at each node from equation (2.26).
(b) Solve for the pressure field from equation (2.28).
(c) Calculate the velocity components, u and w, from equations (2.20) and (2.21).
(d) Solve for the temperatures from equation (2.43).
(e) Calculate the viscosities and densities in the three–dimensional grid using the viscosity model and equation of state in section 2.4.
(f) Update the variables at the boundaries using the boundary conditions.
(g) Repeat steps (a) to (f) until a converged solution is obtained for the current time–level.
(h) Repeat the algorithm until the pressures throughout the domain converge to the same value or until the sum of the time–steps is equal to the the time specified for the post–filling stage.

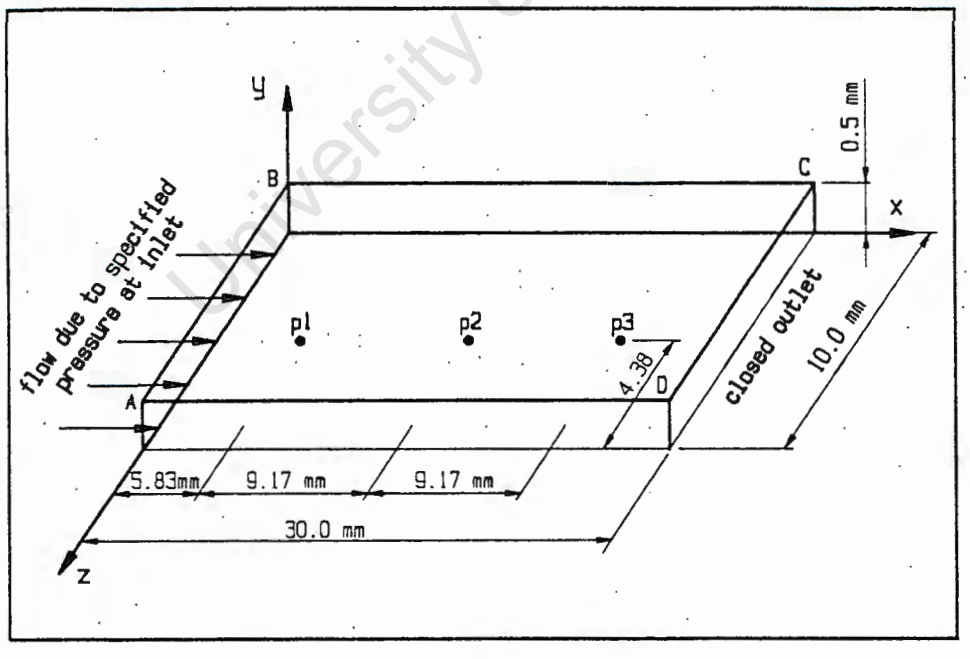

FIGURE 2.9 Dimensions of the model for the post–filling stage

Steps (a) to (f) are repeated for each time–steps until the fractional change in the pressure field is smaller than the convergence criterion and the solution is considered to be converged for that time–step.

2.8 Example calculations

The simulation of polymer melt flow in a thin cavity using the numerical model described in this chapter is demonstrated in the following example calculations. The algorithm was first tested for incompressible Newtonian flow. The results, which are not repeated here, compared well with analytical solutions.

To demonstrate the different features of the numerical model it is sufficient to model the flow in the rectangular cavity shown in Figure 2.6 (p. 58). Since the objective is to compare the GHS model with the GN model in chapter 4, uni–directional flow in the x direction is simulated. The calculational plane for the GHS model lies in the x–z plane. There can be no flow in the y direction. The calculational plane for the GN model is a section through the thickness, with flow in the x–y plane and no flow in the z direction. Therefore, a perfect slip condition is used at the fixed boundary in the z direction to reduce the problem to one–dimensional flow. The cavity is fed from the reservoir through a film gate along the length of the inlet resulting in an essentially straight advancing melt front. If a non–slip boundary condition were specified at the fixed boundary in the z direction, the flow front would only have deviated from a straight line in a small area next to the boundary. The deviation is small and localized since, for Hele–Shaw flow, only the diffusion terms for diffusion in the y direction are included in the momentum equation while the other diffusion terms and all the convection terms are neglected. The resulting flow in the cavity is uni–directional flow in the x direction due to the geometry of the cavity, the boundary conditions and the constant inflow rate at the entrance. As was shown in Figures 2.7, 2.8 and 2.9, the flow in one quarter of the cavity, excluding the reservoir, is considered.

Typical properties of PS are used in the constitutive equations. The material constants for PS used in the viscosity model and equation of state are given in section 2.4. The representative thermal properties for molten PS, as reported by Wang and Hieber (1987), are

melt density	ρ = 940 kg/m^3 (at atmospheric pressure)
thermal conductivity	k = 0,15 J/ms°K
specific heat	c_p = 2100 J/kg m°K

For the purpose of the example calculations, consider the flow of molten PS at 210°C into the cavity at a constant flow rate of 20 cm^3/s. The walls of the cavity are kept at a constant temperature of 110°C which is just above T_g.

2.8.1 Filling stage

Consider weakly compressible, non–Newtonian flow under non–isothermal conditions during the filling of the cavity shown in Figure 2.7 (p. 58). The results due to the movement of the flow front and a comparison between compressible and incompressible flow will be given.

2.8.1.1 Movement of the flow front

The pressure drop along the cavity at different times as the flow front moves through the cavity is shown in Figure 2.10 for compressible flow. Since the pressure in front of the flow front is atmospheric, i.e. 0,1 MPa, the positions of the flow front at different times are given by the points on each graph in Figure 2.10 where p = 0,1 MPa. The positions of the flow front at different times, as it moves through the cavity during the filling stage, are also shown in Figure 2.11. The filling time, which is the time required to fill the cavity, is 0,0315 s.

2.8.1.2 Compressible vs incompressible flow

Different authors have reported a simplified simulation of the filling stage by neglecting compressibility. We determine the effect of this

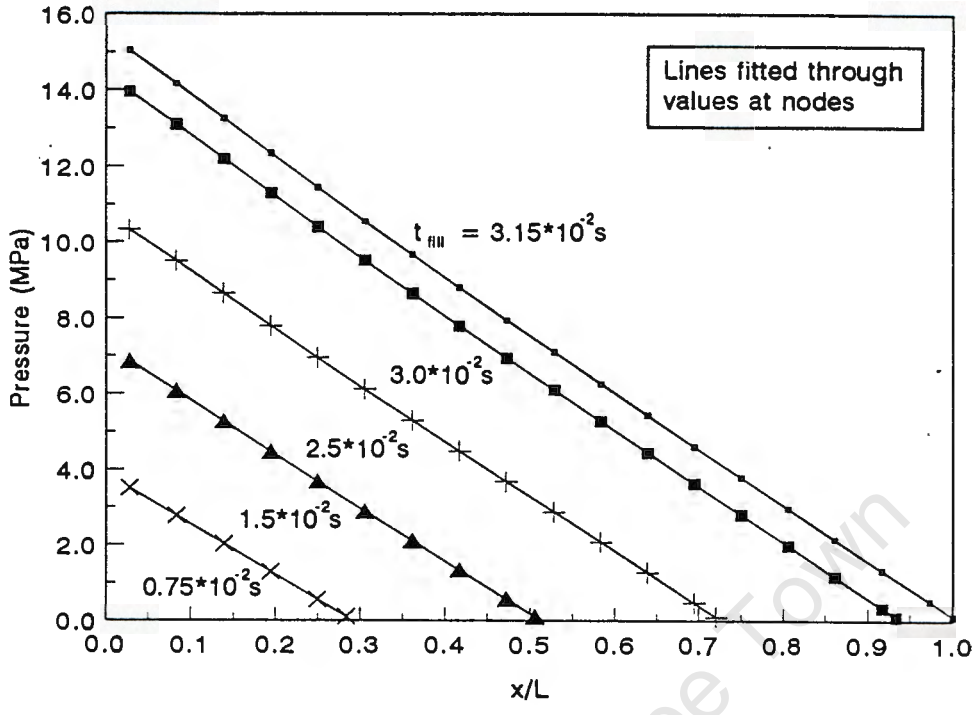

FIGURE 2.10 Change in pressure drop as the flow front moves

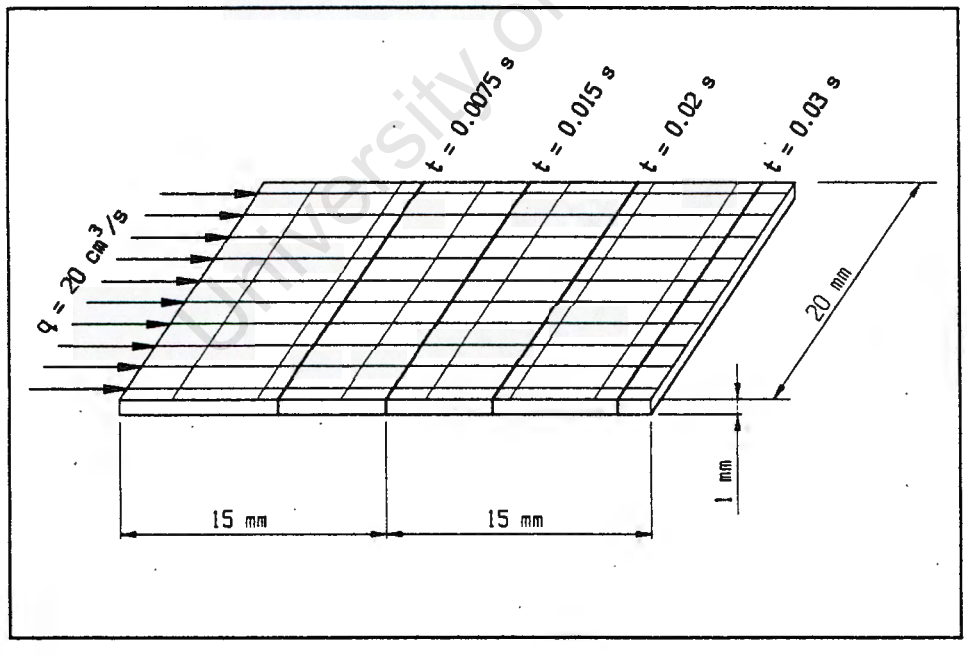

FIGURE 2.11 Movement of the flow front

simplification by comparing the results for compressible and incompressible flow.

The pressure development with time at p1, p2 and p3, for compressible, uni–directional flow in a two–dimensional plane is shown in Figure 2.12 as a solid line. The pressure development for incompressible flow is shown as discrete points at specific time intervals. During the filling stage the influence of compressibility on the pressures in the cavity is negligible as shown in Figure 2.12. The u velocity profile through the thickness at p2, at time t=0,0315 s, is shown in Figure 2.13. The profile for compressible flow are shown as solid lines connecting the calculated nodal values. The u velocities for incompressible flow is shown as the nodal values. The influence of compressibility on the velocity profiles is also small (< 2%).

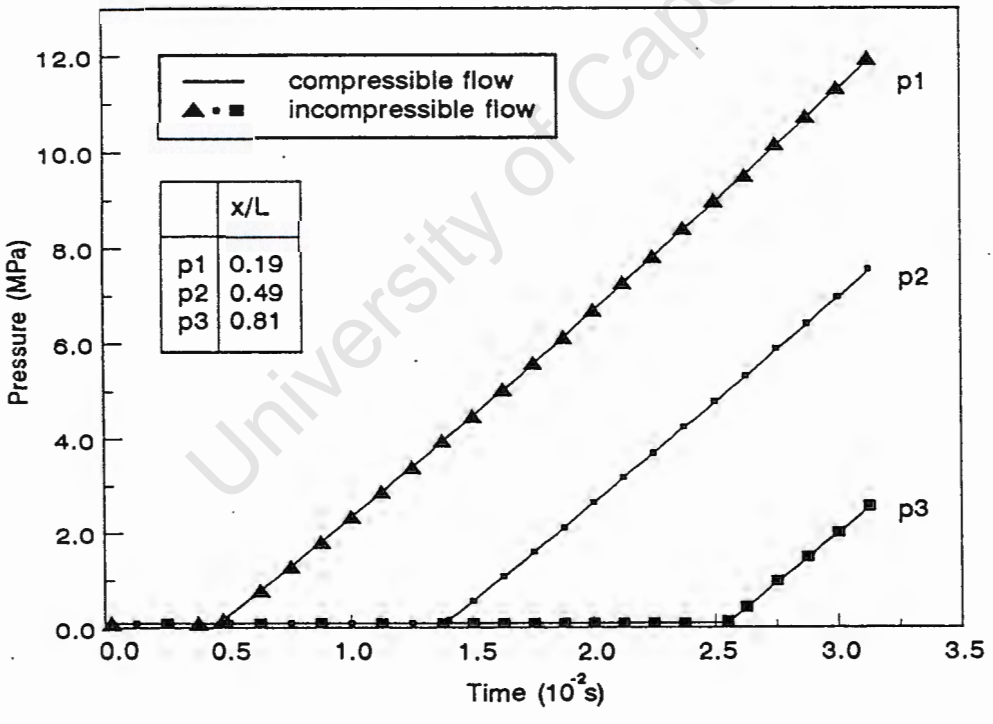

FIGURE 2.12 Pressure development with time at p1, p2 and p3

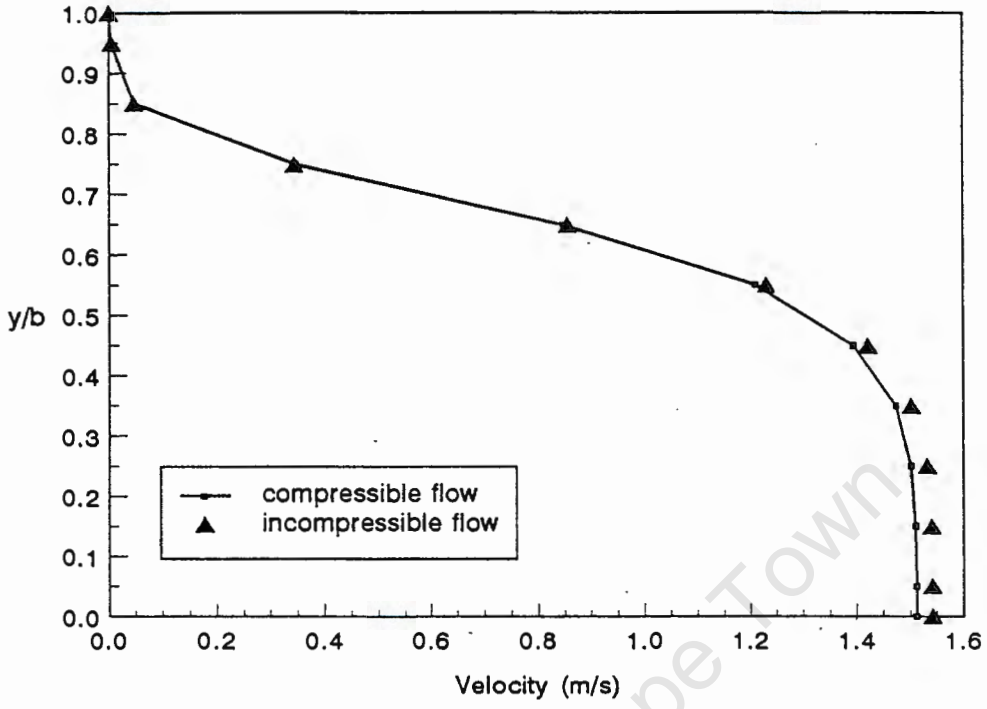

FIGURE 2.13 Velocity profiles of u at p2

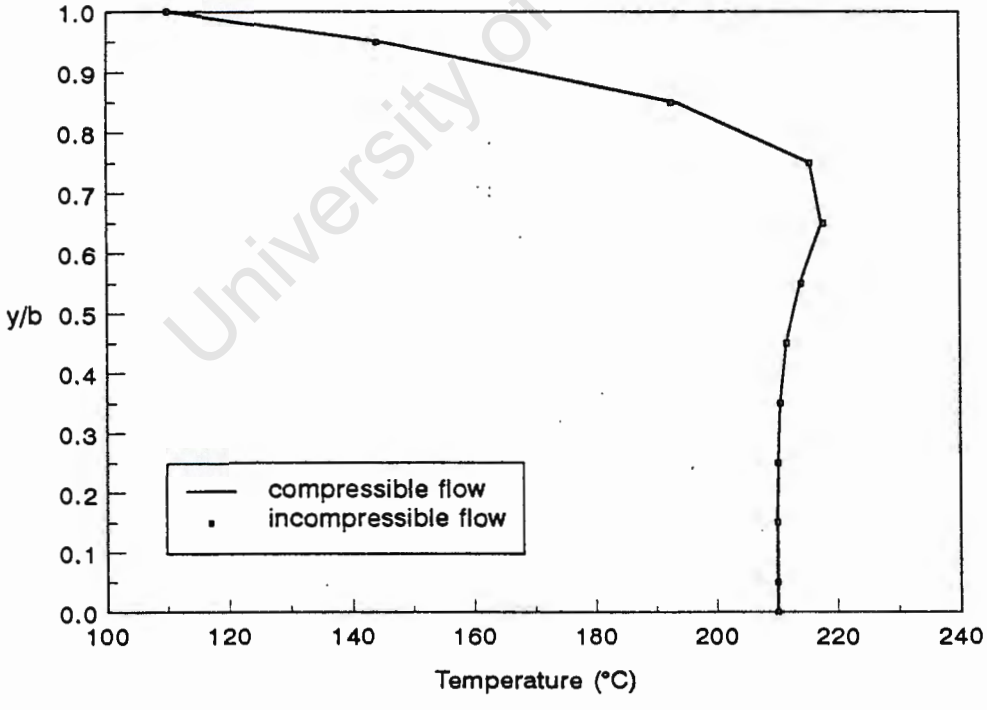

FIGURE 2.14 Temperature profiles at p2

The temperature profiles through the thickness at p2 for compressible and incompressible flow are compared in Figure 2.14. The profile for compressible flow is shown as solid lines connecting the calculated nodal values. In the case of compressible flow the temperatures through the thickness are calculated using the different densitites, calculated at the nodes through the thickness, in the energy equation. For incompressible flow the density variation is not taken into account since a constant density is used in the calculations. It is shown in Figure 2.14 that the effect of compressibility on the temperature profiles during the filling stage is negligible. The small differences in the results of incompressible and compressible flow can be explained by considering the change in density through the thickness. As shown in Figure 2.15 the density only changes by approximately 4 % through the thickness. Therefore the variable density in compressible flow will have a small influence on the results as compared to the constant density in incompressible flow.

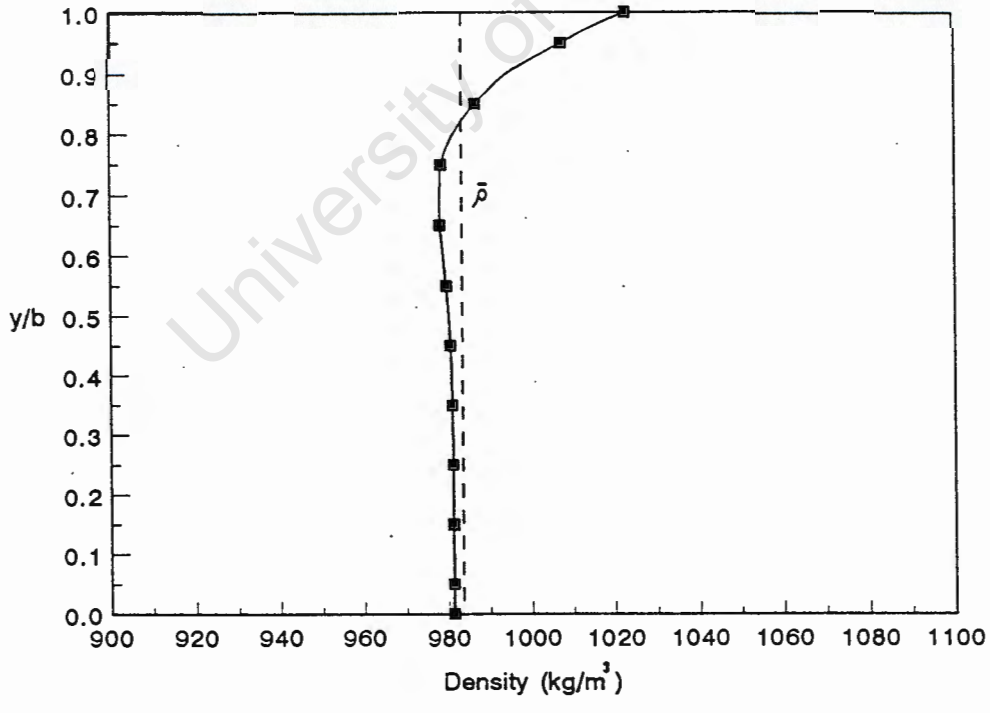

FIGURE 2.15 Density profile and thickness-averaged density at p2

The results shown in Figures 2.12, 2.13 and 2.14 explain why some authors prefer to neglect compressibility in the filling stage. However, for the purposes of comparing the GHS and GN models and since in the GN model the pressures are not assumed to be constant through the thickness as in the GHS model, compressibility will be included in the remainder of the thesis.

2.8.2 Continuous flow through a cavity with an open outlet

Consider continuous flow, without a flow front, of a weakly compressible, non–Newtonian material under non–isothermal conditions, through the cavity shown in Figure 2.8 (p. 60). The time–dependent pressure development for compressible and incompressible flow will be shown. Results of a transient solution of this flow case will be given. The results of a steady–state solution will be given to demonstrate specific features of the GHS model.

2.8.2.1 Time–dependent pressure development

The cavity is considered to be filled with material which is stationary at time t_0=0. The constant inflow specified at the inlet will set the melt in motion and the pressures in the cavity will increase gradually from atmospheric pressure. The pressure development at p1, p2 and p3 (see Figure 2.8, p. 60), is shown in Figure 2.16. Only the first 0,003 s of the calculation results is shown to obtain a better resolution.

2.8.2.2 Similarity between flow with and without a flow front

In section 2.8.1.1 the time to fill the cavity, if the movement of the flow front is modelled, was calculated as 0,0315 s. In this section a solution for continuous flow through a cavity with an open outlet, after 0,0315 s, is compared with the solution of the filling stage at the time of filling. The purpose is to show the similarity between the results of the filling stage and of continuous flow without a front for the specific geometry with one–dimensional flow, used in the comparisons.

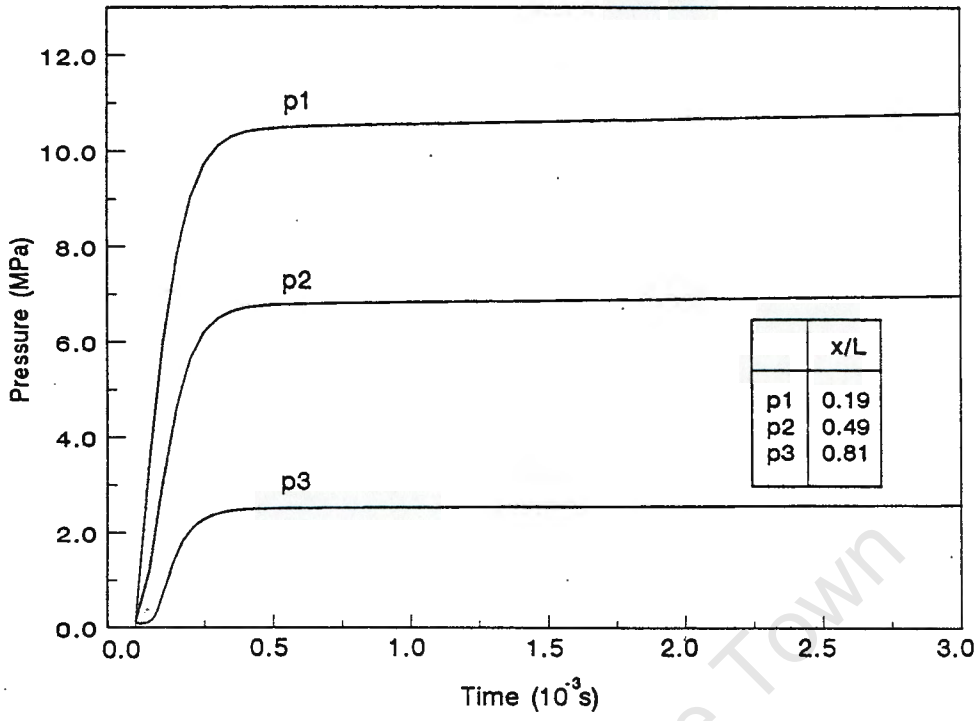

FIGURE 2.16 Pressure development for flow through a cavity with an open outlet

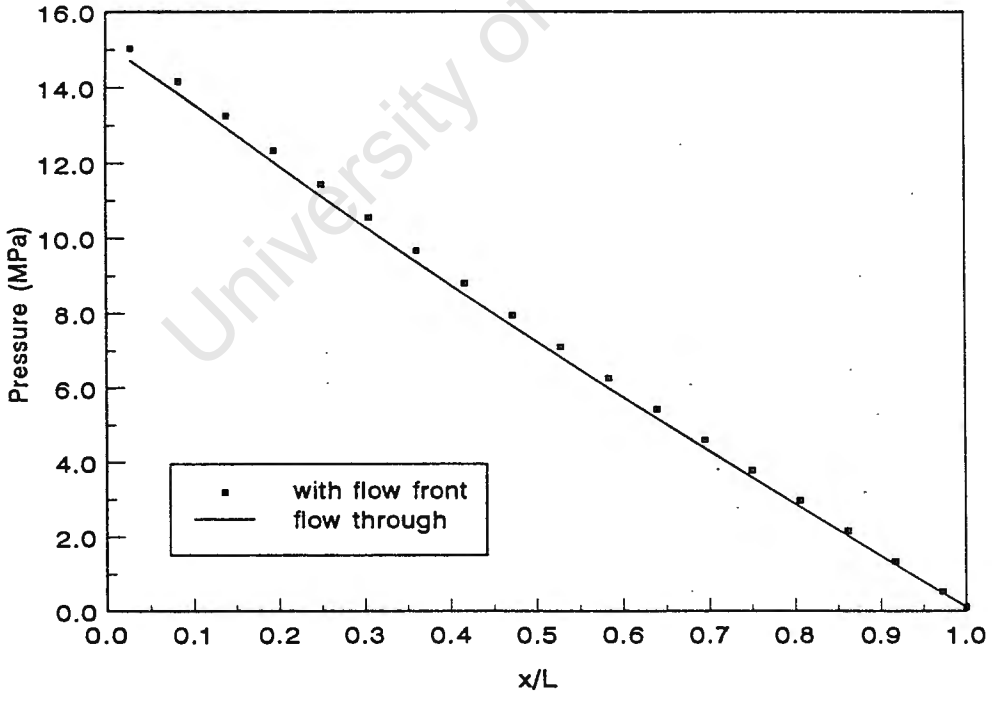

FIGURE 2.17 Pressure drop at a time equal to the filling time

The pressures at time t = 0,0315 s, of which the time–dependent development at three points have been shown in Figures 2.12 and 2.16, respectively, are compared in Figure 2.17. The velocity– and temperature profiles at p2, at time t = 0,0315 s, are compared in Figures 2.18 and 2.19, respectively. In these three figures the results of transient flow through the cavity are shown as lines connecting the calculated nodal values while the results of the filling stage are shown as nodal values. The excellent agreement in all three figures shows that, at a time equal to the filling time, the results of transient flow through the cavity closely represent the results of the filling stage simulating flow with a moving flow front. Therefore the case of continuous flow through the cavity is representative of the filling stage for this specific flow problem.

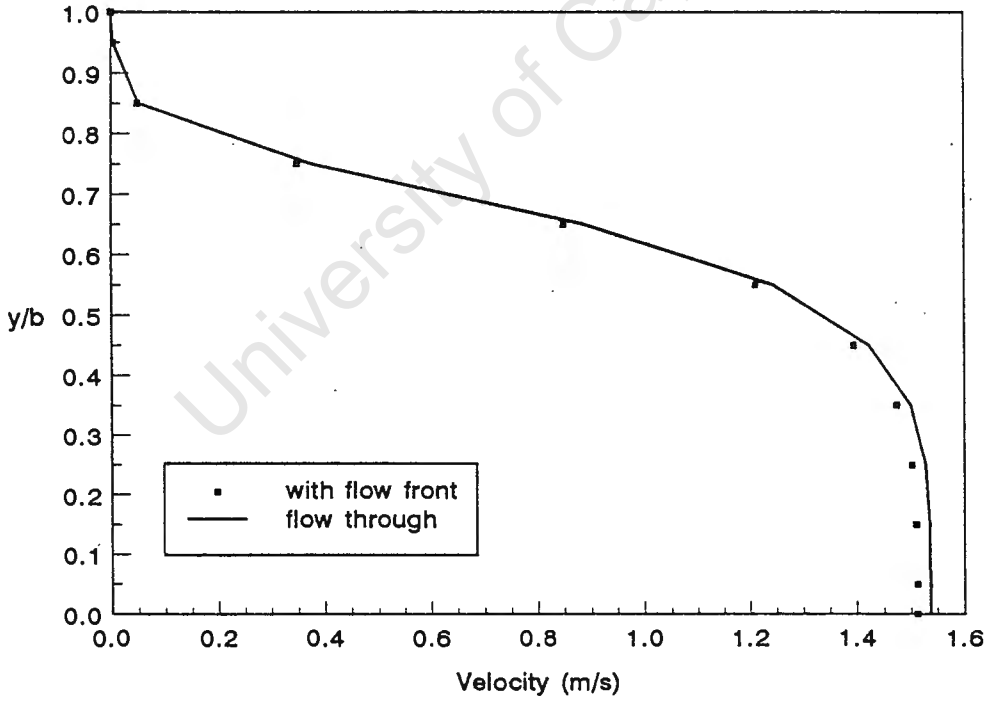

FIGURE 2.18 Velocity profiles at p2 with and without a flow front

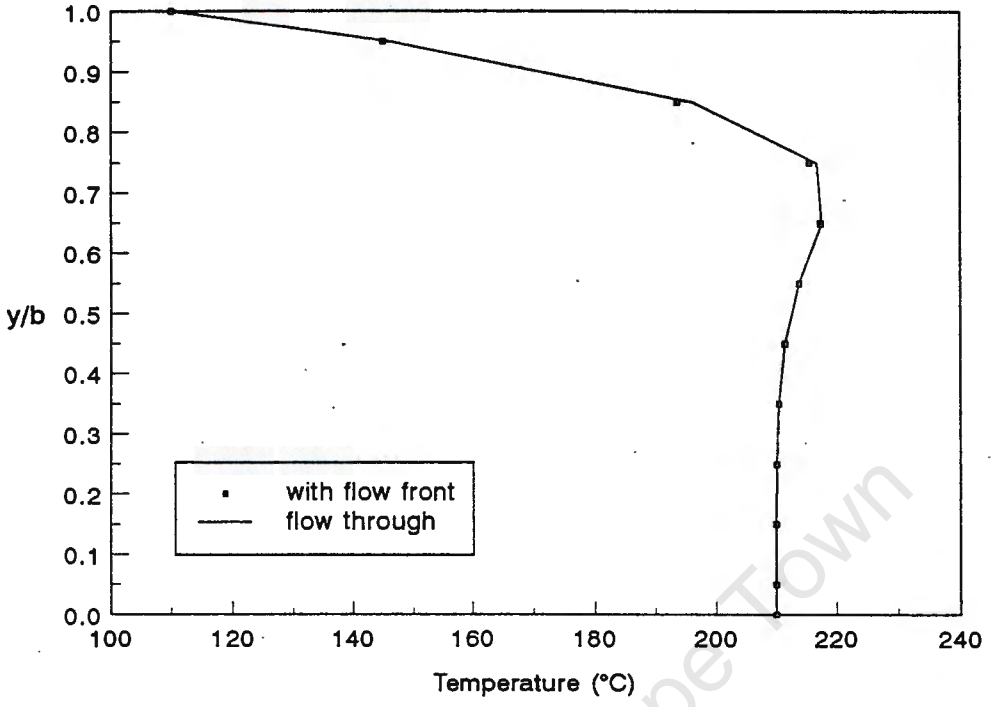

FIGURE 2.19 Temperature profiles at p2 calculated with and without a flow front

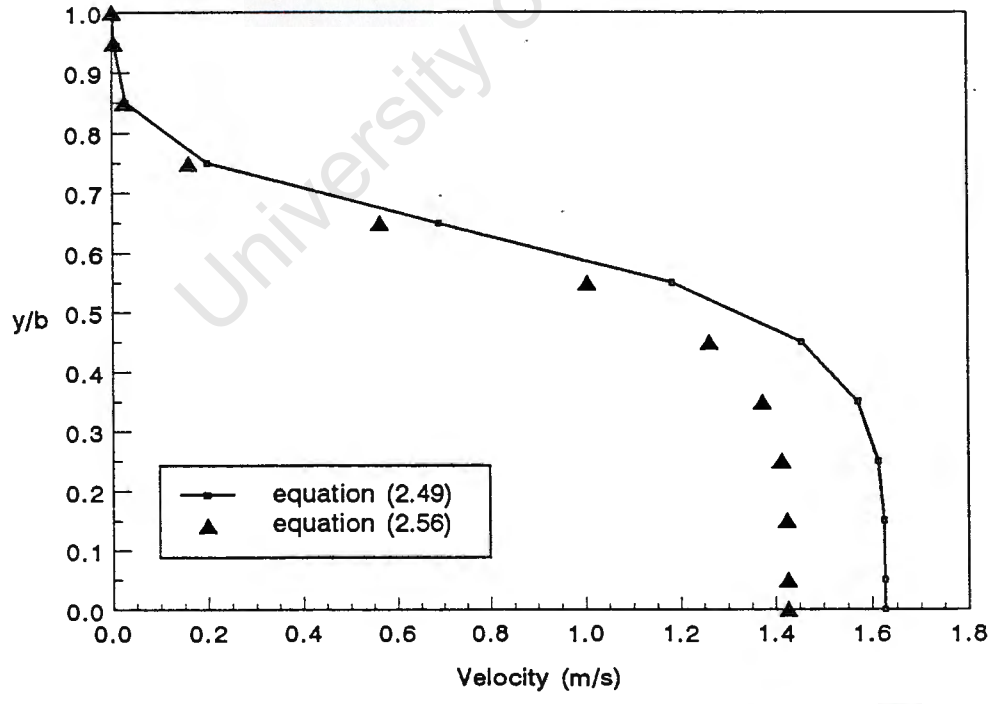

FIGURE 2.20 Velocity profiles for incompressible steady–state flow

2.8.2.3 Steady–state solution for the cavity with an open outlet

Consider non–Newtonian incompressible flow under non–isothermal conditions. The density is kept constant at a value equal to the melt density at atmospheric pressure. For incompressible flow, equation (2.50) is used to solve for the pressures with S calculated using either (2.49) or (2.56). The resulting u velocity profiles at p2 (see Figure 2.8) are compared in Figure 2.20. The solid lines are drawn between the nodal values obtained with equation (2.49). As discussed in section 2.2.3 the deviation in the velocity profiles is due to a numerical incompatibility if equation (2.56) is used.

Consider incompressible Newtonian flow by keeping both viscosity and density constant. In this case an analytical solution for the velocity profile can be obtained (Shames, 1982). The analytical solution is a parabola about the centre line of the gap with the maximum velocity equal to 1,5 times the average velocity. This result is shown in Figure 2.21 as a solid line. The velocity profile calculated with the

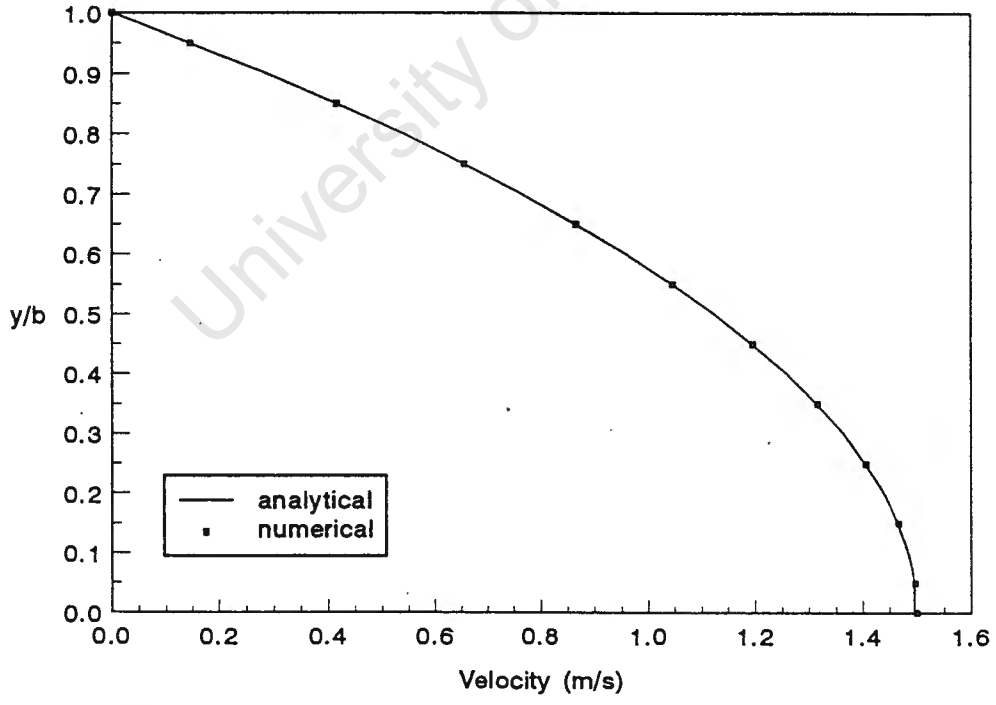

FIGURE 2.21 Velocity profile compared with analytical solution

numerical model, for any position in the cavity, is shown as nodal values. The solutions obtained with the numerical model and the analytical solution, respectively, are in excellent agreement. There is only a slight deviation at the centre line of the gap where a zero normal gradient boundary condition is specified in the numerical model.

2.8.3 Post–filling stage

During the post–filling stage the velocities will decrease while the pressures will develop with time until the melt becomes stationary. The post–filling stage is modelled as transient flow of a compressible non–Newtonian melt in the cavity shown in Figure 2.9 (p. 63). The resulting values at the end of the filling stage, of which representative values are shown in Figures 2.12 through 2.15, are used as initial values for the post–filling stage. Alternatively, due to the similarity between the filling stage and continuous flow through a cavity at a time equal to the filling time, the results of the latter flow case can be used as initial values. Results, representative of these inital values, are shown in Figures 2.17, 2.18 and 2.19. The post–filling stage is simulated until the pressures throughout the cavity are equal to the specified holding pressure. This provides a criterion for the GHS and GN numerical models to be compared more precisely.

One–dimensional heat transfer in the post–filling stage, after the melt has become stationary, is not modelled since it does not form part of the numerical models which are compared to determine the influence of the Hele–Shaw approximations. As will be discussed in section 3.4 the time dependence of the temperature is neglected in the source term, equation (2.80), for the purpose of comparing the development of the pressures solved with the GHS and GN models, but will be included in the refined GHS model in chapter 5.

Compressibility cannot be neglected in the post–filling stage since the cavity is filled with a molten material subjected to a holding pressure at the inlet. The melt is compared as the pressures throughout the cavity increase to the same value as the holding pressure. The holding pressure can either be specified to be equal to the pressure at the inlet, at the end of the filling stage, or a higher holding pressure can be specified. The pressure development for both cases are shown.

2.8.3.1 Solution for holding pressure equal to inlet pressure

The pressure at the inlet, which was 14.71 MPa at the end of the filling stage, is used as the constant holding pressure. The time–dependent pressure development at p1, p2 and p3 (see Figure 2.9, p. 63) is shown in Figure 2.22. Only the first 0,005 s of the post–filling stage is shown in order to show more clearly the development of the pressures, which change much faster in the first part of the post–filling stage than later on when the velocities become very small and when the

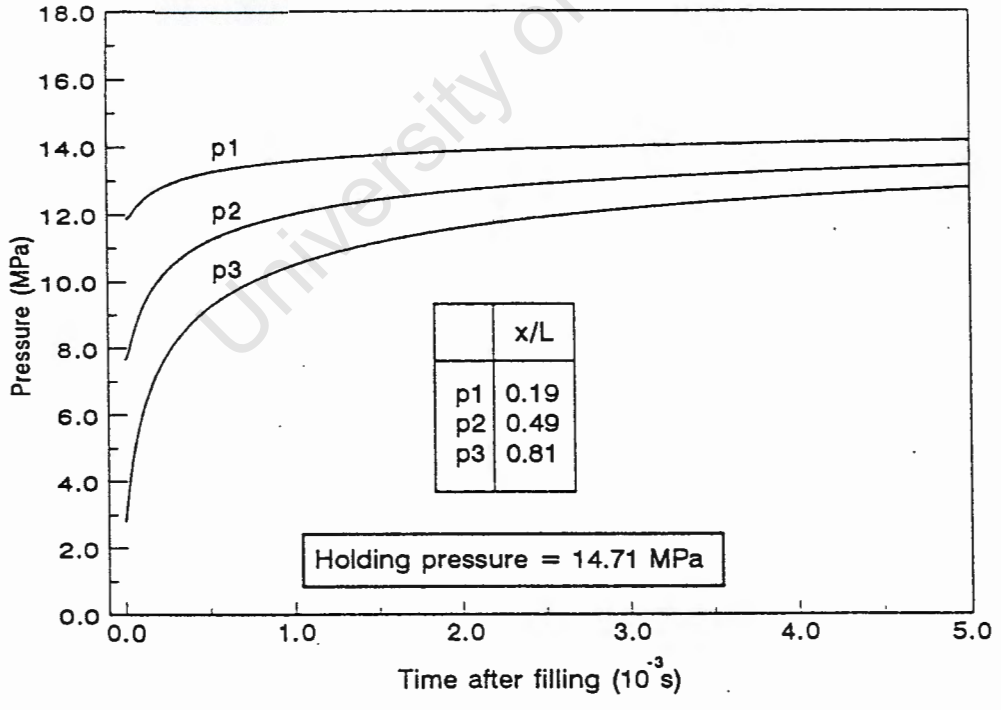

FIGURE 2.22 Time–dependent pressure development in the post–filling stage

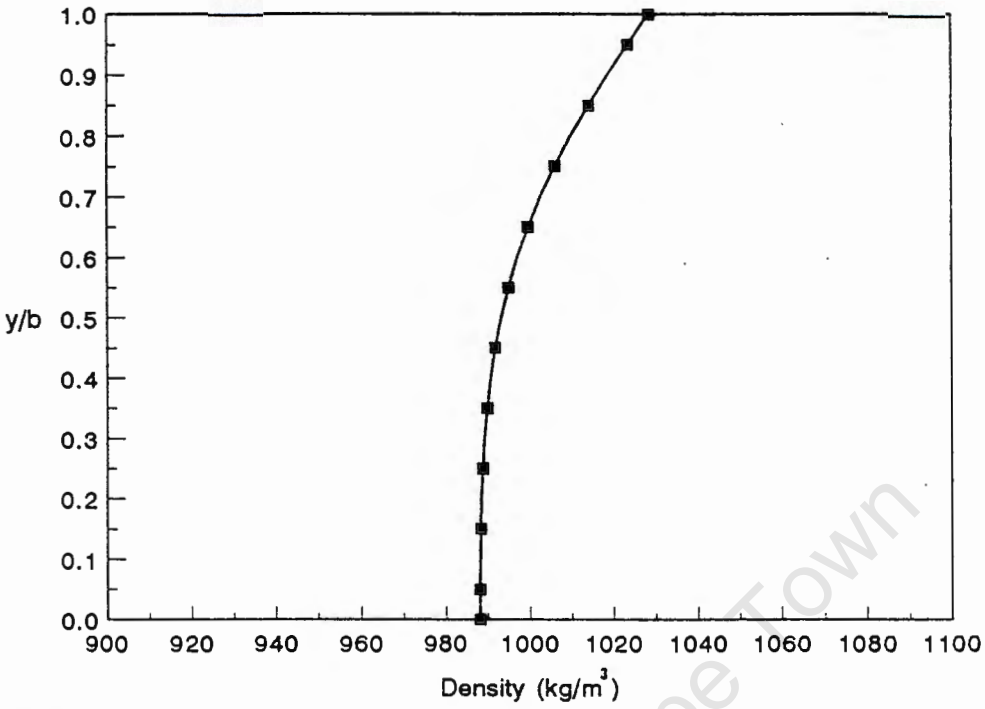

FIGURE 2.23 Density profile at p2 at the end of the post–filling stage

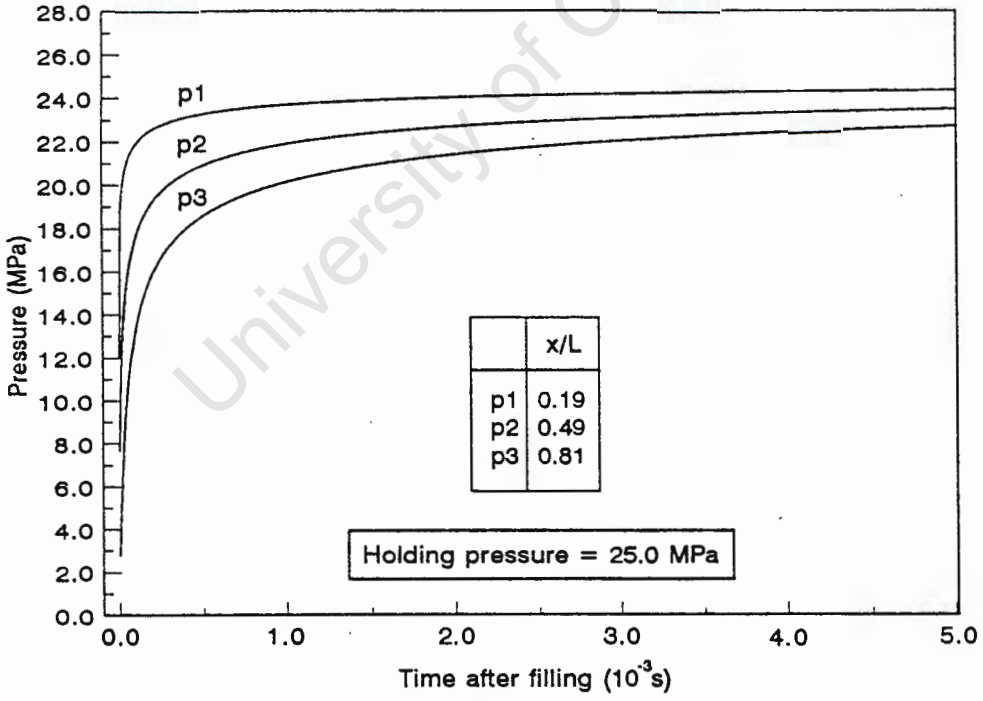

FIGURE 2.24 Time–dependent pressure development with a specified high holding pressure in the post–filling stage

pressures increase slowly until reaching the same constant value. In order to obtain the time–step independent solution in Figure 2.22 initial time–steps equal to or smaller than 10^{-5} s are required.

In Figure 2.23 the density profile at p2 is shown. The densities are higher than in the filling stage since the pressure at p2 is higher and the temperatures have decreased. The profile is calculated with the constitutive equations given in section 2.4

2.8.3.2 Solution for increased holding pressure

The post–filling stage is simulated with a holding pressure specified to be higher than the inlet pressure at the end of the filling stage. For the purpose of this calculation example a holding pressure of 25,0 MPa is chosen. The initial values which are equal to the values at the end of the filling stage are the same as in the previous example (see section 2.8.3.1). The time–dependent pressure development is shown in Figure 2.24. In this case the pressures throughout the cavity develop to a value equal to the specified higher holding pressure.

2.7 Summary

In this chapter the GHS numerical model has been developed to simulate compressible, non–Newtonian flow under non–isothermal conditions during the filling and post–filling stages. This model includes the movement of the flow front during the filling stage. The model has been demonstrated by simulating the flow in a thin rectangular cavity. Three flow cases have been considered. The filling stage, the post–filling stage and continuous flow through a cavity with an open outlet which does not have a flow front. Similarity between the results of the filling stage and the results of continuous flow through the cavity at a time equal to the filling time has been shown for the specific flow problem. The results of compressible and incompressible flow have been compared. Although the influence of compressibility in the filling stage is small, compressibility will not be neglected in the GHS model. It has been shown that in the case of incompressible flow the calculation of S, using a simplified formulation reported in the literature, is incompatible with the calculation of the velocity. This resulted in a deviation in the velocity profiles. The simplified formulation will therefore not be used. The numerical results for steady–state flow with constant density and viscosity agree very well with analytical results. In the next chapter the GN numerical model, solving the Navier–Stokes equation, will be developed in order to compare it with the GHS model in chapter 4.

CHAPTER 3

3 A NUMERICAL MODEL SOLVING THE NAVIER–STOKES EQUATIONS

3.1 Introduction

In this chapter a numerical model to solve the two–dimensional Navier–Stokes equations is described. The model is generalized to non–Newtonian fluids and will be identified as the generalized Newtonian (GN) model to distinguish it from the generalized Hele–Shaw (GHS) model. The GN model, which does not include the Hele–Shaw approximations, is developed for the purpose of comparing it with the GHS model.

The governing equations for a weakly compressible polymer melt and the non–dimensional form of these equations are described. The governing equations are discretized with a finite volume method in a two–dimensional Cartesian coordinate system using a staggered grid. The calculational plane is a section through the thickness of the cavity. The set of discretized equations is solved using the PISO algorithm. For the purpose of comparing the GHS and GN models, transient and steady–state solutions of continuous flow through a cavity with an open outlet is discussed. The solution of the post–filling stage is also discussed.

The same constitutive equations, for generalized Newtonian materials, as in the GHS model are used in the GN model.

Since the purpose of doing example calculations with this model is to compare it with the GHS model, the example calculations will be given in chapter 4 where the models are compared.

3.2 Governing equations

As described in chapter 2, the coefficient of bulk viscosity is negligible for the type of flow considered in this study. Therefore, μ', has been eliminated from the governing equations using $\mu' = 2/3 \cdot \mu$ (Anderson et al., 1984). The stresses are substituted in the momentum and energy equations (see section 2.2), and the resulting three–dimensional Navier–Stokes equations, expressed as a system of scalar equations using a Cartesian coordinate system, are :

Continuity equation

$$\frac{\partial \rho}{\partial t} + \frac{\partial}{\partial x}(\rho u) + \frac{\partial}{\partial y}(\rho v) + \frac{\partial}{\partial z}(\rho w) = 0 \; . \tag{3.1}$$

Momentum equations

$$\begin{aligned} &\frac{\partial}{\partial t}(\rho u) + \frac{\partial}{\partial x}(\rho u^2) + \frac{\partial}{\partial y}(\rho uv) + \frac{\partial}{\partial z}(\rho uw) \\ &= -\frac{\partial p}{\partial x} + \frac{\partial}{\partial x}\left[\frac{2}{3}\mu\left(2\frac{\partial u}{\partial x} - \frac{\partial v}{\partial y} - \frac{\partial w}{\partial z}\right)\right] + \frac{\partial}{\partial y}\left[\mu\left(\frac{\partial u}{\partial y} + \frac{\partial v}{\partial x}\right)\right] \\ &\quad + \frac{\partial}{\partial z}\left[\mu\left(\frac{\partial w}{\partial x} + \frac{\partial u}{\partial z}\right)\right] + \rho f_x \; , \end{aligned} \tag{3.2a}$$

$$\begin{aligned} &\frac{\partial}{\partial t}(\rho v) + \frac{\partial}{\partial x}(\rho uv) + \frac{\partial}{\partial y}(\rho v^2) + \frac{\partial}{\partial z}(\rho vw) \\ &= -\frac{\partial p}{\partial y} + \frac{\partial}{\partial x}\left[\mu\left(\frac{\partial v}{\partial x} + \frac{\partial u}{\partial y}\right)\right] + \frac{\partial}{\partial y}\left[\frac{2}{3}\mu\left(2\frac{\partial v}{\partial y} - \frac{\partial u}{\partial x} - \frac{\partial w}{\partial z}\right)\right] \\ &\quad + \frac{\partial}{\partial z}\left[\mu\left(\frac{\partial v}{\partial z} + \frac{\partial w}{\partial y}\right)\right] + \rho f_y \; , \end{aligned} \tag{3.2b}$$

$$\frac{\partial}{\partial t}(\rho w) + \frac{\partial}{\partial x}(\rho uw) + \frac{\partial}{\partial y}(\rho vw) + \frac{\partial}{\partial z}(\rho w^2)$$

$$= -\frac{\partial p}{\partial z} + \frac{\partial}{\partial x}\left[\mu\left(\frac{\partial w}{\partial x} + \frac{\partial u}{\partial z}\right)\right] + \frac{\partial}{\partial y}\left[\mu\left(\frac{\partial v}{\partial z} - \frac{\partial w}{\partial y}\right)\right]$$

$$+ \frac{\partial}{\partial z}\left[\frac{2}{3}\mu\left(2\frac{\partial w}{\partial z} - \frac{\partial u}{\partial x} - \frac{\partial v}{\partial y}\right)\right] + \rho f_z \,. \qquad (3.2c)$$

Energy equation

$$c_p\frac{\partial}{\partial t}(\rho T) + c_p\frac{\partial}{\partial x}(\rho uT) + c_p\frac{\partial}{\partial y}(\rho vT) + c_p\frac{\partial}{\partial z}(\rho wT)$$

$$-\left[\frac{\partial p}{\partial t} + \frac{\partial}{\partial x}(up) + \frac{\partial}{\partial y}(vp) + \frac{\partial}{\partial z}(wp)\right]$$

$$= \frac{\partial}{\partial x}\left(k\frac{\partial T}{\partial x}\right) + \frac{\partial}{\partial y}\left(k\frac{\partial T}{\partial y}\right) + \frac{\partial}{\partial z}\left(k\frac{\partial T}{\partial z}\right) + SS \,, \qquad (3.3)$$

where $$SS = \mu\left[2\left(\frac{\partial u}{\partial x}\right)^2 + 2\left(\frac{\partial v}{\partial y}\right)^2 + 2\left(\frac{\partial w}{\partial z}\right)^2 + \left(\frac{\partial v}{\partial x} + \frac{\partial u}{\partial y}\right)^2\right.$$

$$\left. + \left(\frac{\partial w}{\partial y} + \frac{\partial v}{\partial z}\right)^2 + \left(\frac{\partial u}{\partial z} + \frac{\partial w}{\partial x}\right)^2 - \frac{2}{3}\left(\frac{\partial u}{\partial x} + \frac{\partial v}{\partial y} + \frac{\partial w}{\partial z}\right)^2\right] . \qquad (3.4)$$

These governing equations are generalized to non–Newtonian fluids by replacing the Newtonian viscosity, μ, with a non–Newtonian viscosity, η, which depends on the pressure, temperature and shear rate. These governing equations will be referred to as the Navier–Stokes equations in the remainder of the text. Strictly speaking the term Navier–Stokes equations refers to the viscous momentum equations (3.2), but it is common practice (Anderson et al., 1984) to include the continuity and energy equations in the set of equations referred to as the Navier–Stokes equations.

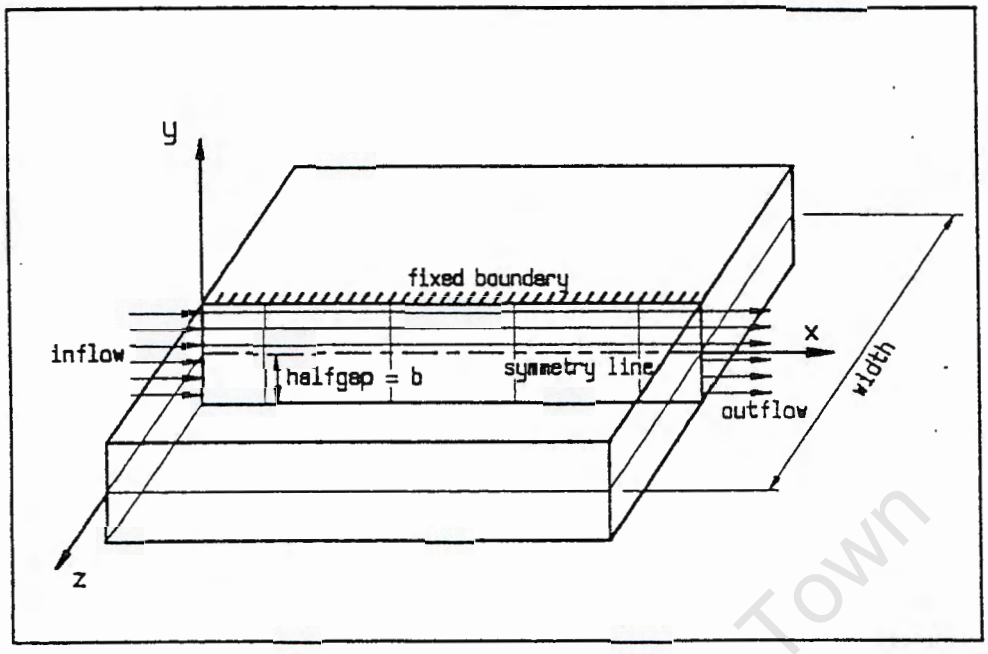

FIGURE 3.1 Calculational plane for the GN model

The numerical model described in this chapter solves the Navier–Stokes equations in two dimensions. All the variables are independent of z. The calculational plane is the x–y plane which is a section through the thickness of the cavity as shown in Figure 3.1. The numerical model solves for the pressure and the two velocity components simultaneously.

Body forces in the momentum equations are neglected and the thermal conductivity in the energy equation is assumed to be constant. For polymer materials the terms involving pressure in the energy equation can also be neglected (Kamal & Lafleur, 1986). The governing equations in two dimensions therefore become :

Continuity

$$\frac{\partial \rho}{\partial t} + \frac{\partial}{\partial x}(\rho u) + \frac{\partial}{\partial y}(\rho v) = 0 \; . \qquad (3.5)$$

Momentum

$$\frac{\partial}{\partial t}(\rho u) + \frac{\partial}{\partial x}(\rho u^2) + \frac{\partial}{\partial y}(\rho uv)$$

$$= -\frac{\partial p}{\partial x} + \frac{4}{3}\cdot\frac{\partial}{\partial x}(\eta\cdot\frac{\partial u}{\partial x}) + \frac{\partial}{\partial y}(\eta\cdot\frac{\partial u}{\partial y}) + S^u \ , \qquad (3.6)$$

where the source term, S^u, is given by

$$S^u = -\frac{2}{3}\cdot\frac{\partial}{\partial x}(\eta\cdot\frac{\partial v}{\partial y}) + \frac{\partial}{\partial y}(\eta\cdot\frac{\partial v}{\partial x}) \ , \qquad (3.7a)$$

which, for the purpose of the discretization in section 3.3.2, can be rewritten as

$$S^u = -\frac{2}{3}\cdot\frac{\partial v}{\partial y}\cdot\frac{\partial \eta}{\partial x} + \frac{\eta}{3}\cdot\frac{\partial^2 v}{\partial x \partial y} + \frac{\partial v}{\partial x}\cdot\frac{\partial \eta}{\partial y} \ , \qquad (3.7b)$$

and $$\frac{\partial}{\partial t}(\rho v) + \frac{\partial}{\partial y}(\rho v^2) + \frac{\partial}{\partial x}(\rho uv)$$

$$= -\frac{\partial p}{\partial y} + \frac{4}{3}\cdot\frac{\partial}{\partial y}(\eta\cdot\frac{\partial v}{\partial y}) + \frac{\partial}{\partial x}(\eta\cdot\frac{\partial v}{\partial x}) + S^v \ , \qquad (3.8)$$

where the source term, S^v, is given by

$$S^v = -\frac{2}{3}\cdot\frac{\partial}{\partial y}(\eta\cdot\frac{\partial u}{\partial x}) + \frac{\partial u}{\partial x}(\eta\cdot\frac{\partial u}{\partial y}) \ , \qquad (3.9a)$$

which can be rewritten as

$$S^v = -\frac{2}{3}\cdot\frac{\partial u}{\partial x}\cdot\frac{\partial \eta}{\partial y} + \frac{\eta}{3}\cdot\frac{\partial^2 u}{\partial x \partial y} + \frac{\partial u}{\partial y}\cdot\frac{\partial \eta}{\partial x} \ . \qquad (3.9b)$$

Energy

$$\frac{\partial}{\partial t}(\rho T) + \frac{\partial}{\partial x}(\rho T u) + \frac{\partial}{\partial y}(\rho T v)$$

$$= \frac{1}{c_p}\cdot\left(\frac{\partial}{\partial x}\cdot\left(k\cdot\frac{\partial T}{\partial x}\right) + \frac{\partial}{\partial y}\left(k\cdot\frac{\partial T}{\partial y}\right)\right) + S^T \,, \qquad (3.10)$$

where the source term $S^T = SS/c_p$ and SS is given by

$$SS = \eta\cdot\left[2\left(\frac{\partial u}{\partial x}\right)^2 + 2\left(\frac{\partial v}{\partial y}\right)^2 + \left(\frac{\partial v}{\partial x} + \frac{\partial u}{\partial y}\right)^2 - \frac{2}{3}\left(\frac{\partial u}{\partial x} + \frac{\partial v}{\partial y}\right)^2\right] . \qquad (3.11)$$

Since $\frac{\partial u}{\partial x}$ and $\frac{\partial v}{\partial y}$ are negligible in comparison with $\frac{\partial u}{\partial y}$ and $\frac{\partial v}{\partial x}$ in shear–dominated flow, SS reduces to

$$SS = \eta\dot{\gamma}^2 \,, \qquad (3.12)$$

where $$\dot{\gamma} = \left[\left(\frac{\partial v}{\partial x} + \frac{\partial u}{\partial y}\right)^2\right]^{1/2} . \qquad (3.13)$$

Incompressible flow is also modelled with the above equations for weakly compressible flow but in the case of incompressibility the density is kept constant.

In order to derive a non–dimensional form of the continuity and momentum equations, the following dimensionless variables are defined :

$$\bar{x} = \frac{x}{L} \,, \quad \bar{y} = \frac{y}{L} \,, \qquad (3.14a,b)$$

$$\bar{u} = \frac{u}{U} , \quad \bar{v} = \frac{v}{U} , \tag{3.15a,b}$$

$$\bar{p} = \frac{p}{\rho_c U^2} , \quad \bar{\eta} = \frac{\eta}{\eta_0} , \quad \bar{\rho} = \frac{\rho}{\rho_c} , \tag{3.16a,b,c}$$

$$\bar{t} = \frac{tU}{L} . \tag{3.17}$$

Here L is a characteristic length, U a characteristic velocity and ρ_c is the constant melt density. The Newtonian base value of the viscosity, η_0, is the viscosity at zero shear rate, atmospheric pressure and at a reference melt temperature. In this case we choose the melt temperature to be 100°C above the glass transition temperature.

The half-gap dimension, b, in the y direction is chosen as characteristic length and the inlet velocity as the characteristic velocity. The Reynolds number is defined by

$$R_e = \frac{Ub\rho_c}{\eta_0} . \tag{3.18}$$

The dimensionless variables are introduced into the two-dimensional continuity and momentum equations by substitution. After rearrangement, the results can be written as :

Continuity

$$\frac{\partial \bar{\rho}}{\partial \bar{t}} + \frac{\partial}{\partial \bar{x}}(\bar{\rho}\bar{u}) + \frac{\partial}{\partial \bar{y}}(\bar{\rho}\bar{v}) = 0 , \tag{3.19}$$

Momentum (x direction)

$$\frac{\partial}{\partial \bar{\bar{t}}}(\bar{\bar{\rho}}\bar{\bar{u}}) + \frac{\partial}{\partial \bar{\bar{x}}}(\bar{\bar{\rho}}\bar{\bar{u}}^2) + \frac{\partial}{\partial \bar{\bar{y}}}(\bar{\bar{\rho}}\bar{\bar{u}}\bar{\bar{v}})$$

$$= -\frac{\partial \bar{\bar{p}}}{\partial \bar{\bar{x}}} + \frac{1}{Re}\frac{4}{3}\cdot\frac{\partial}{\partial \bar{\bar{x}}}(\bar{\bar{\eta}}\cdot\frac{\partial \bar{\bar{u}}}{\partial \bar{\bar{x}}}) + \frac{1}{Re}\frac{\partial}{\partial \bar{\bar{y}}}(\bar{\bar{\eta}}\cdot\frac{\partial \bar{\bar{u}}}{\partial \bar{\bar{y}}})$$

$$-\frac{1}{Re}\frac{2}{3}\cdot\frac{\partial}{\partial \bar{\bar{x}}}(\bar{\bar{\eta}}\cdot\frac{\partial \bar{\bar{v}}}{\partial \bar{\bar{y}}}) + \frac{1}{Re}\frac{\partial}{\partial \bar{\bar{y}}}(\bar{\bar{\eta}}\cdot\frac{\partial \bar{\bar{v}}}{\partial \bar{\bar{x}}}) \; . \qquad (3.20)$$

An equation similar to (3.20) can be written for the y–direction momentum.

Since the same constitutive equations as in chapter 2 are used, the same constant, $\bar{\bar{\tau}}^*$, as before is introduced. As was shown in section 2.2.1 the Cross model, equation (1.10), can be written in non–dimensional form as

$$\bar{\bar{\eta}} = \frac{\eta}{\eta_0} = \frac{1}{1 + [\bar{\bar{\gamma}}/(\bar{\bar{\tau}}^* \, Re)]^{1-n}} \; , \qquad (3.21)$$

where $$\bar{\bar{\gamma}} = \frac{\dot{\gamma} b}{U} \; , \qquad (3.22)$$

and $$\bar{\bar{\tau}}^* = \frac{\tau^*}{\rho_c U^2} \; . \qquad (3.23)$$

Therefore, when the Cross model is used as constitutive equation, there are two parameters, Re and $\bar{\bar{\tau}}^*$, that define the problem as will be shown in chapter 4.

The movement of the flow front and consequently also the fountain flow at the free surface are not included in the GN model. The purpose of developing the GN numerical model is to compare it with the GHS numerical model to determine how the Hele–Shaw approximations influence the solution, and not to develop a complete model alongside the GHS model. The modelling of the flow front used in the GHS model assumes that the flow front does not vary in the thickness direction since the pressures are constant through the thickness. This assumption precludes the simulation of fountain flow in the GHS model. The simplified approach used in the GHS model, to determine the position of the flow front by solving for the fractional volume of fluid, f, using the continuity equation, cannot be incorporated in the approach used in the GN model which does not include the Hele–Shaw approximations. In the GN model the pressures, which are calculated as a function of the thickness direction, and the velocities are solved simultaneously using the pressure correction approach of the PISO algorithm. The pressures are therefore not solved directly from the continuity equation as in the GHS model.

The fundamental solution methods used in the GHS and GN models, which are to be compared in order to determine the influence of the Hele–Shaw approximations, are not altered by excluding the movement of the flow front. Since the objective is to compare the two models within the same framework, both models are developed to simulate flow without a moving flow front. For this purpose continuous flow through a cavity with an open outlet is considered (see Figure 3.1, p. 83).

3.3 Discretization

The dependent variables in the momentum and energy equations (3.6), (3.8) and (3.10) all obey a generalized conservation principle which enables the formulation of a general transport equation (Van Doormaal & Raithby, 1984). In two dimensions the general transport equation can be written as

$$\frac{\partial}{\partial t}(\rho\phi) = -\frac{\partial}{\partial x}(\rho u\phi) - \frac{\partial}{\partial y}(\rho v\phi) + \frac{\partial}{\partial x}\left[\Gamma\frac{\partial\phi}{\partial x}\right] + \frac{\partial}{\partial y}\left[\Gamma\frac{\partial\phi}{\partial y}\right] + SS, \quad (3.24)$$

where ϕ represents any one of the dependent variables (u, v or T), Γ is the diffusion coefficient and SS is a source term. The quantities Γ and SS are specific to a particular meaning of ϕ, e.g. in equation (3.6), where $\phi = u$, $\Gamma = f(\eta)$ and $SS = S^u - \frac{\partial p}{\partial x}$. In equation (3.10), where $\phi = T$, $\Gamma = k/c_p$ and $SS = S^T$.

The transport equations are discretized using the finite volume formulation. A two–dimensional Cartesian grid is constructed over the calculation domain. The domain is then divided into a number of non–overlapping control volumes in such a way that each grid point, except those on the domain boundary, is surrounded by one control volume. This arrangement of control volumes requires the spacing between nodes at the boundaries to be half the spacing in the rest of the grid, if the grid has equally spaced nodes, as is shown in Figure 3.2. The solid lines are grid lines and the dashed lines indicate the relative position of control volumes.

In the finite volume approach the transport equations are integrated over a control volume or cell as described in section 2.3. A typical two–dimensional control volume and the centre points of its neighbours are shown in Figure 3.3.

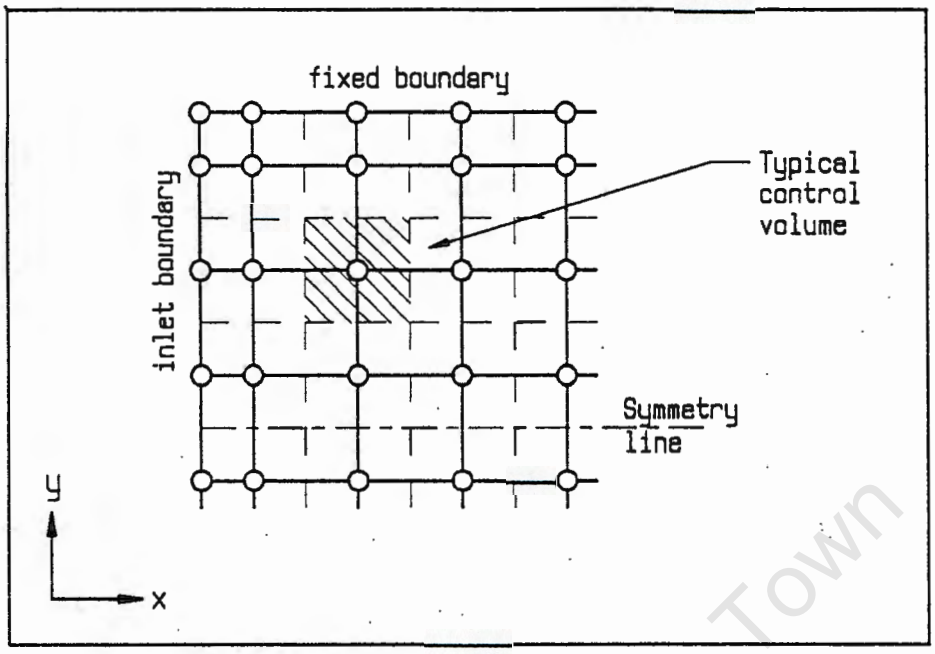

FIGURE 3.2 Control volumes in the two–dimensional computational grid used in the GN model.

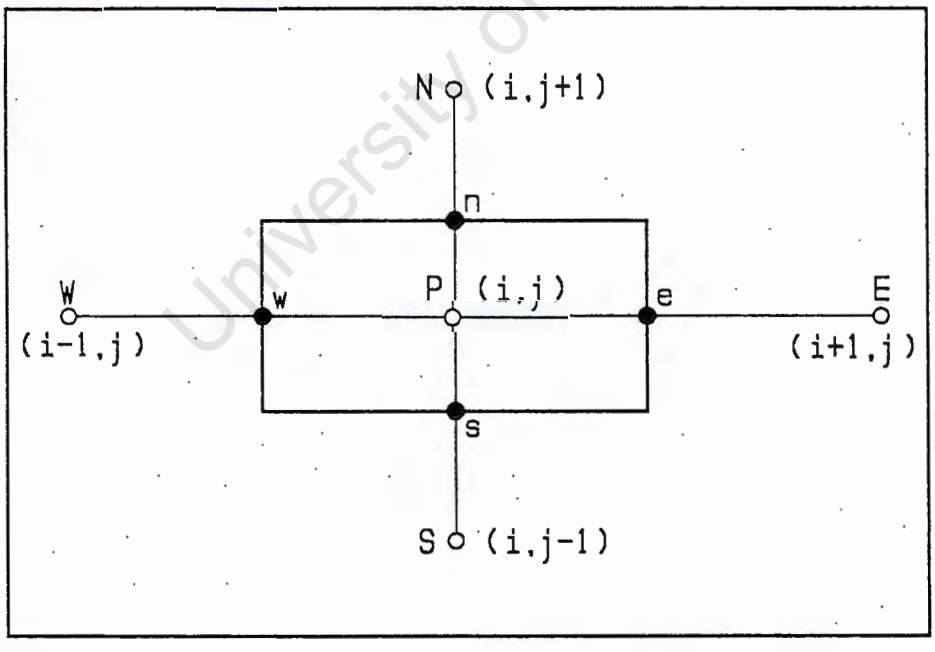

FIGURE 3.3 A typical control volume in the x–y plane where E, W, N and S are the centre points of its neighbours.

For each control volume the general discretized form of equation (3.24) gives the relation between ϕ at the control volume centre, P, and the neighbouring values of ϕ (Patankar, 1984) as follows :

$$(a_P + a_t)\phi_P^t = \Sigma a_{nb}\, \phi_{nb} + SS + a_t\phi_P^{t-1} , \qquad (3.25)$$

where a_{nb} are the neighbouring coefficients which account for the combined convection–diffusion influences at the control volume boundaries and the lengths of the boundaries, ϕ_{nb} is the neighbouring values and $(SS + a_t\phi_P^{t-1})$ is a source term.

Equation (3.25) exists for each hydrodynamic variable in every interior cell of the grid (Le Grange, 1990). Therefore a system of n equations in n unknowns, where n is the total number of internal nodes, has to be solved for each hydrodynamic variable.

The finite volume discretization is done using the staggered grid shown in Figure 3.4. The staggered grid is used to overcome numerical difficulties occuring when all the variables are calculated for the same grid points as described by Patankar (1984). In the staggered grid, the velocity components are calculated at the points that lie on the boundaries of the control volumes. Thus, the x–direction velocity, u, is calculated at the boundaries that are normal to the x direction and the y–direction velocity, v, at the boundaries normal to the y direction. The locations for u and v are indicated in Figure 3.4 by short arrows, while the grid points are indicated by small circles. The dashed lines indicate the control volume boundaries.

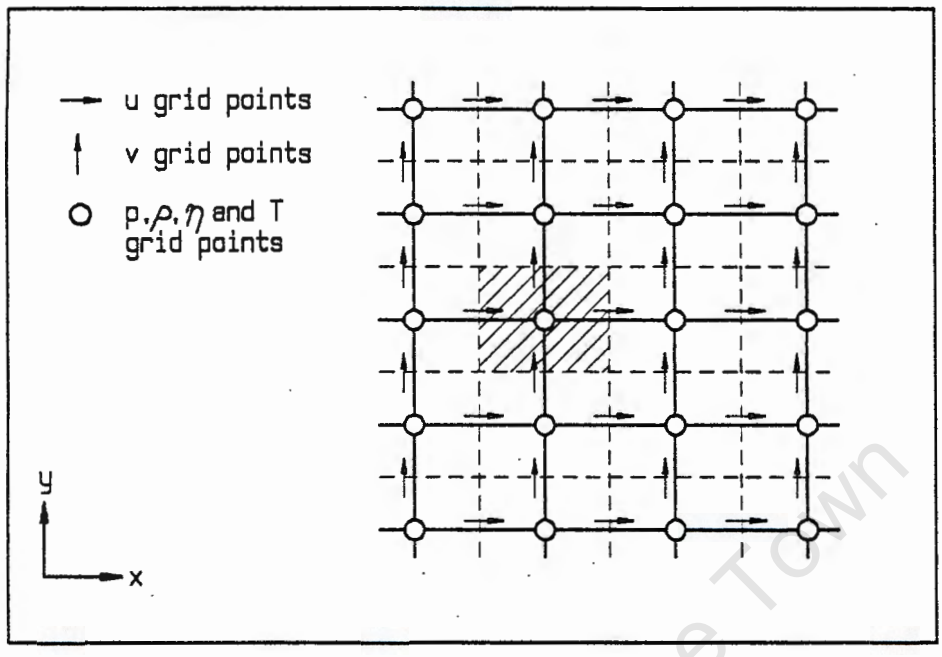

FIGURE 3.4 Two–dimensional staggered grid used in the GN model

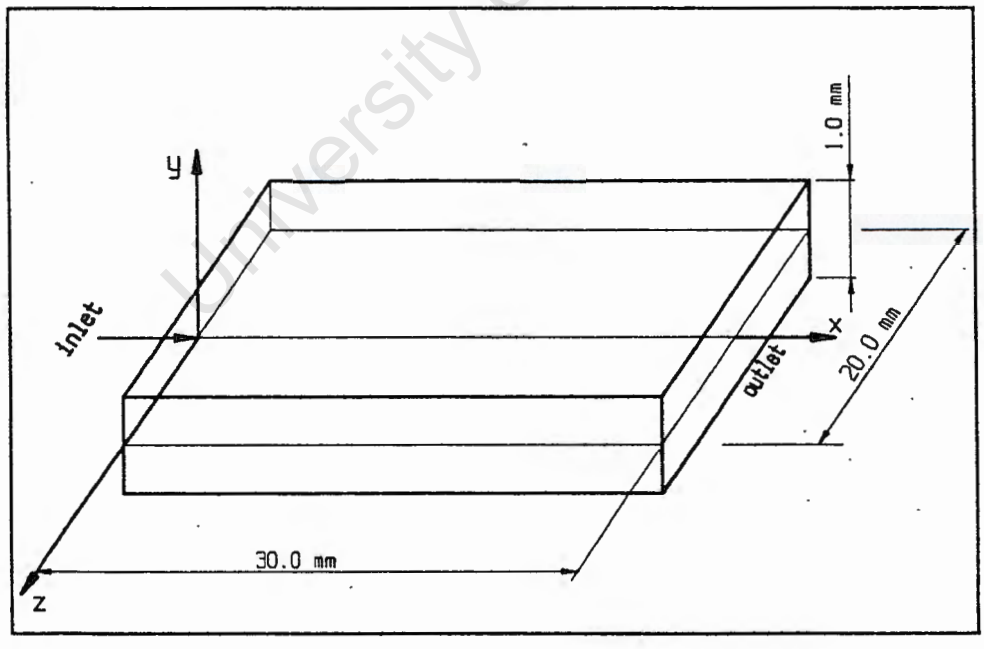

FIGURE 3.5 Geometry of the cavity

3.3.1 The finite volume discretization of the continuity equation

The discretized equation is

$$\Delta x\Delta y\cdot\frac{(\rho_P^t - \rho_P^{t-1})}{\Delta t} + \Delta y(\rho_e u_e - \rho_w u_w) + \Delta x(\rho_n v_n - \rho_s v_s) = 0 \ . \quad (3.26)$$

The discretized **continuity equation** can be rewritten as

$$\Delta x\Delta y\cdot\frac{(\rho_P - \rho_P^{t-1})}{\Delta t} + u_e\rho_e\cdot\Delta y - u_w\rho_w\cdot\Delta y + v_n\rho_n\cdot\Delta x - v_s\rho_s\cdot\Delta x = 0, \quad (3.27)$$

where ρ is calculated analogous to equation (3.60) on p. 107.

3.3.2 Finite volume discretization of the momentum equations

Equations (3.6) and (3.8) are discretized as follows.

3.3.2.1 x-direction momentum (equation 3.6)

$$\frac{(\rho_P u_P - \rho_P^{t-1}u_P^{t-1})}{\Delta t}\cdot\Delta x\Delta y + (\rho_e\bar{u}_e u_e - \rho_w\bar{u}_w u_w)\Delta y + (\rho_n\bar{v}_n u_n - \rho_s\bar{v}_s u_s)\Delta x$$

$$= \Delta y(p_{i,j} - p_{i+1,j}) + \frac{4}{3}\cdot\Delta y\{\eta_e\cdot\frac{(u_E - u_P)}{\Delta x_e} - \eta_w\cdot\frac{(u_P - u_W)}{\Delta x_w}\}$$

$$+ \Delta x\{\eta_n\cdot\frac{(u_N - u_P)}{\Delta y_n} - \eta_s\cdot\frac{(u_P - u_S)}{\Delta y_s}\}$$

$$+ \left[\frac{1}{3}\cdot\{\eta_e\cdot\frac{(v_{i+1,j} - v_{i+1,j-1})}{\Delta y_e} - \eta_w\cdot\frac{(v_{i,j} - v_{i,j-1})}{\Delta y_w}\}\Delta y\right.$$

$$+ \{\frac{(v_{i+1,j} + v_{i+1,j-1})}{2} - \frac{(v_{i,j} + v_{i,j-1})}{2}\}\cdot(\eta_n - \eta_s)$$

$$- \frac{2}{3}\cdot\left\{\frac{(v_{i,j} + v_{i+1,j})}{2} - \frac{(v_{i,j-1} + v_{i+1,j-1})}{2}\right\}\cdot(\eta_e - \eta_w)\Big], \qquad (3.28)$$

where the term in square brackets is the source term S^u, multiplied by $\Delta x \Delta y$. $\bar{u}$, ρ and η are given by

$$\bar{u}_e = \frac{1}{2}\cdot(u_E + u_P) \qquad (3.29a)$$

$$\bar{u}_w = \frac{1}{2}\cdot(u_P + u_W) \qquad (3.29b)$$

$$\bar{v}_n = \frac{1}{2}\cdot(v_N + v_P) \qquad (3.29c)$$

$$\bar{v}_s = \frac{1}{2}\cdot(v_P + v_S)\ , \qquad (3.29d)$$

and
$$\rho_e = \rho_{i+1,j} \qquad (3.30a)$$

$$\rho_w = \rho_{i,j} \qquad (3.30b)$$

$$\rho_n = \frac{1}{4}\cdot(\rho_{i,j} + \rho_{i+1,j} + \rho_{i,j+1} + \rho_{i+1,j+1}) \qquad (3.30c)$$

$$\rho_s = \frac{1}{4}\cdot(\rho_{i,j} + \rho_{i+1,j} + \rho_{i,j-1} + \rho_{i+1,j-1})\ , \qquad (3.30d)$$

and
$$\eta_e = \eta_{i+1,j} \qquad (3.31a)$$

$$\eta_w = \eta_{i,j} \qquad (3.31b)$$

$$\eta_n = \frac{1}{4}\cdot(\eta_{i,j} + \eta_{i+1,j} + \eta_{i,j+1} + \eta_{i+1,j+1}) \qquad (3.31c)$$

$$\eta_s = \frac{1}{4}\cdot(\eta_{i,j} + \eta_{i+1,j} + \eta_{i,j-1} + \eta_{i+1,j-1}) \qquad (3.31d)$$

Following Hieber and Shen (1978) we use upwind differencing in the convection term for numerical stability (Roache, 1972) which implies that

$$\bar{u}_e u_e = u_P[\bar{u}_e, 0] - u_E[-\bar{u}_e, 0] \tag{3.32a}$$

$$\bar{u}_w u_w = u_W[\bar{u}_w, 0] - u_P[-\bar{u}_w, 0] \tag{3.32b}$$

$$\bar{u}_n u_n = u_P[\bar{u}_n, 0] - u_N[-\bar{u}_n, 0] \tag{3.32c}$$

$$\bar{u}_s u_s = u_S[\bar{u}_s, 0] - u_P[-\bar{u}_s, 0] . \tag{3.32d}$$

Substitution of equations (3.32) into (3.28), results in the discretized momentum equation

$$u_P a_P^u = u_E a_E^u + u_W a_W^u + u_N a_N^u + u_S a_S^u + u_P^{t-1} a_T^u + (p_{i+1} - p_i)\Delta y + \Delta x \Delta y \cdot S^u , \tag{3.33}$$

which is similar to the formulation given by Patanker (1984) and

where $$a_E^u = \frac{4}{3}\cdot\eta_e\cdot\frac{\Delta y}{\Delta x_e} + [-\bar{u}_e\rho_e\cdot\Delta y, 0] \tag{3.34a}$$

$$a_W^u = \frac{4}{3}\cdot\eta_w\cdot\frac{\Delta y}{\Delta x_w} + [\bar{u}_w\rho_w\cdot\Delta y, 0] \tag{3.34b}$$

$$a_N^u = \eta_n\cdot\frac{\Delta x}{\Delta y_n} + [-\bar{v}_n\rho_n\cdot\Delta x, 0] \tag{3.34c}$$

$$a_S^u = \eta_s\cdot\frac{\Delta x}{\Delta y_s} + [\bar{v}_s\rho_s\cdot\Delta x, 0] \tag{3.34d}$$

$$a_T^u = \rho_P^{t-1}\frac{\Delta x \Delta y}{\Delta t} , \tag{3.34e}$$

and $$a_P^u = \frac{4}{3}\cdot\eta_e\cdot\frac{\Delta y}{\Delta x_e} + [\,\bar{u}_e\rho_e\cdot\Delta y\ ,\ 0]$$

$$+ \frac{4}{3}\cdot\eta_w\cdot\frac{\Delta y}{\Delta x_w} + [-\bar{u}_w\rho_w\cdot\Delta y\ ,\ 0]$$

$$+ \eta_n\cdot\frac{\Delta x}{\Delta y_n} + [\,\bar{v}_n\rho_n\cdot\Delta x\ ,\ 0]$$

$$+ \eta_s\cdot\frac{\Delta x}{\Delta y_e} + [-\bar{v}_s\rho_s\cdot\Delta x\ ,\ 0]$$

$$+ \rho_P\cdot\frac{\Delta x\Delta y}{\Delta t}\ , \qquad (3.35)$$

or $$a_P^u = a_E^u + a_W^u + a_N^u + a_S^u + a_T^u$$

$$+ [\bar{u}_e\rho_e\cdot\Delta y - \bar{u}_w\rho_w\cdot\Delta y + \bar{v}_n\rho_n\cdot\Delta x - \bar{v}_s\rho_s\cdot\Delta x$$

$$+ \frac{(\rho_P - \rho_P^{t-1})}{\Delta t}\cdot\Delta x\Delta y]\ . \qquad (3.36)$$

Since it follows from continuity that last term in square brackets in (3.36) is zero, this equation becomes

$$a_P^u = a_E^u + a_W^u + a_N^u + a_S^u + a_T^u\ . \qquad (3.37)$$

3.3.2.2 <u>y–direction momentum</u> (equation 3.8)

The finite volume discretization of the y–direction momentum is analogous to the x–direction discretization giving the discretized momentum equation :

$$v_P a_P^v = v_N a_N^v + v_S a_S^v + v_E a_E^v + v_W a_W^v + v_P^{t-1} a_T^v$$

$$+ (p_{i,j} - p_{i,j+1})\Delta x + \Delta x \Delta y \cdot S^v \ . \qquad (3.38)$$

3.3.3 Finite volume discretization of the energy equation

$$\Delta x \Delta y \left[\frac{(\rho T)_P - (\rho T)_P^{t-1}}{\Delta t}\right] + \Delta y \left[(\rho T \bar{u})_e - (\rho T \bar{u})_w\right] + \Delta x \left[(\rho T \bar{v})_n - (\rho T \bar{v})_s\right]$$

$$= \{\Delta y \left[k \cdot \left(\frac{T_E - T_P)}{\Delta x_e} - k \cdot \frac{(T_P - T_W)}{\Delta x_w}\right]\right.$$

$$\left. + \ \Delta x \left[k \cdot \frac{(T_N - T_P)}{\Delta y_n} - k \cdot \frac{(T_P - T_S)}{\Delta y_s}\right]\right\} \frac{1}{c_p} + \Delta x \Delta y \cdot S^T \ , \qquad (3.39)$$

where

$$\bar{u}_e = u_{i,j} \qquad (3.40a)$$

$$\bar{u}_w = u_{i-1,j} \qquad (3.40b)$$

$$\bar{v}_n = v_{i,j} \qquad (3.40c)$$

$$\bar{v}_s = v_{i,j-1} \ . \qquad (3.40d)$$

Using upwind differencing in the convection terms for numerical stability (Roache, 1972), implies that

$$\bar{u}_e \cdot T_e = T_P[\bar{u}_e \ , \ 0] - T_E[-\bar{u}_e \ , \ 0] \qquad (3.41a)$$

$$\bar{u}_w \cdot T_w = T_W[\bar{u}_w \ , \ 0] - T_P[-\bar{u}_w \ , \ 0] \qquad (3.41b)$$

$$\bar{u}_n \cdot T_n = T_P[\bar{u}_n \ , \ 0] - T_N[-\bar{u}_n \ , \ 0] \qquad (3.41c)$$

$$\bar{u}_s \cdot T_s = T_S[\bar{u}_s \ , \ 0] - T_P[-\bar{u}_s \ , \ 0] \ . \qquad (3.41d)$$

Subsitution of equations (3.41) into (3.39) results in the discretized energy equation (Patanker, 1984) :

$$T_P a_P = T_E a_E + T_W a_W + T_N a_N + T_S a_S + T_P^{t-1} a_T + \Delta x \Delta y \cdot S^T \quad , \quad (3.42)$$

where

$$a_E = \frac{\Delta y \cdot k_e}{\Delta x_e c_p} + [-\bar{u}_e \rho_e \cdot \Delta y \ , \ 0] \quad (3.43a)$$

$$a_W = \frac{\Delta y \cdot k_w}{\Delta x_w c_p} + [\ \bar{u}_w \rho_w \cdot \Delta y \ , \ 0] \quad (3.43b)$$

$$a_N = \frac{\Delta x \cdot k_n}{\Delta y_n c_p} + [-\bar{v}_n \rho_n \cdot \Delta x \ , \ 0] \quad (3.43c)$$

$$a_S = \frac{\Delta x \cdot k_s}{\Delta y_s c_p} + [\ \bar{v}_s \rho_s \cdot \Delta x \ , \ 0] \quad (3.43d)$$

$$a_T = \rho_P^{t-1} \cdot \frac{\Delta x \Delta y}{\Delta t} \ , \quad (3.43e)$$

and

$$\begin{aligned} a_P = & \frac{\Delta y \cdot k_e}{\Delta x_e c_p} + [\ \bar{u}_e \rho_e \cdot \Delta y \ , \ 0] \\ & + \frac{\Delta y \cdot k_w}{\Delta x_w c_p} + [-\bar{u}_w \rho_w \cdot \Delta y \ , \ 0] \\ & + \frac{\Delta x \cdot k_n}{\Delta y_s c_p} + [\ \bar{v}_n \rho_n \cdot \Delta x \ , \ 0] \\ & + \frac{\Delta x \cdot k_s}{\Delta y_s c_p} + [-\bar{v}_s \rho_s \cdot \Delta x \ , \ 0] \\ & + \rho_P \cdot \frac{\Delta x \Delta y}{\Delta t} \ . \end{aligned} \quad (3.44)$$

As before it follows from continuity that (3.44) becomes

$$a_P = a_E + a_W + a_N + a_S + a_T \,. \tag{3.45}$$

The source term is discretized as follows

$$\Delta x \Delta y \cdot S^T = \frac{\eta}{c_p} \left(\Delta y \Delta x \cdot \left[\frac{(v_e - v_w)}{\Delta x} + \frac{(u_n - u_s)}{\Delta y}\right]^2\right) , \tag{3.46}$$

where $$u_n = \frac{1}{4}\left[u_{i,j} + u_{i-1,j} + u_{i,j+1} + u_{i-1,j+1}\right] \tag{3.47a}$$

$$u_s = \frac{1}{4}\left[u_{i,j} + u_{i-1,j} + u_{i,j-1} + u_{i-1,j-1}\right] \tag{3.47b}$$

$$v_e = \frac{1}{4}\left[v_{i,j} + v_{i,j-1} + v_{i+1,j} + v_{i+1,j-1}\right] \tag{3.47c}$$

$$v_w = \frac{1}{4}\left[v_{i,j} + v_{i,j-1} + v_{i-1,j} + v_{i-1,j-1}\right] \,. \tag{3.47d}$$

Equation (3.42) is solved (Patankar, 1984) with a tridiagonal matrix algorithm (TDMA).

3.4 Constitutive equations

Since the objective is to compare the GN and GHS models in chapter 4, the same constitutive equations for generalized Newtonian materials are used in both models. Therefore the constitutive equations described in section 2.4 is also used in the GN model.

In the discretization of the Navier–Stokes equations the time derivative of ρ can be expressed as

$$\frac{\partial \rho}{\partial t} = \frac{\partial \rho}{\partial p} \cdot \frac{\partial p}{\partial t} + \frac{\partial \rho}{\partial T} \cdot \frac{\partial T}{\partial t} \cdot \qquad (3.48)$$

Only the term involving the time dependence of the pressure is taken into account in the source term of the pressure correction equation while the time dependence of the temperature is neglected. During the filling stage $\frac{\partial T}{\partial t}$ is much smaller than $\frac{\partial p}{\partial t}$ and the last term of (3.48) has a negligible influence on the solution.

In the post–filling stage, before the melt becomes stationary, the influence of the time dependence of the temperature is still much smaller than the time dependence of the pressure. In the GHS model the last term of equation (3.48) is given by

$$\frac{\partial \overline{\rho}}{\partial \overline{T}} \cdot \frac{\partial \overline{T}}{\partial t} ,$$

where $\overline{\rho}$ and $\overline{T}$ are the thickness averaged values. Since the objective is to compare the GHS and GN models, the time dependence of the temperature in the source term is neglected in solving the post–filling stage. By neglecting $\frac{\partial \rho}{\partial T} \cdot \frac{\partial T}{\partial t}$ in the source term in the GN model and $\frac{\partial \overline{\rho}}{\partial \overline{T}} \cdot \frac{\partial \overline{T}}{\partial t}$ in in the source term in the GHS model, the pressure development can be compared more precisely since the pressures throughout the cavity will develop to a constant value. The one–dimensional heat transfer in the post–filling stage, after the melt has become stationary, is not modelled in the GN model since it does not form part of the numerical model which is developed for the purpose of comparing it with the GHS model (see section 2.8.3).

3.5 Boundary conditions

The GN model solves the continuity and momentum equations simultaneously to give the pressures and the velocity components in the x and y directions. The temperatures are calculated with the energy

equation. Since a finite volume method is used to discretize the governing equations, the variables are calculated only at the interior nodes which coincide with the control volume centres. Boundary conditions are required to specify the values of the variables at the boundaries.

For the purpose of comparing the GN and GHS models, two flow cases with different boundary conditions will be considered. The first is transient flow through a cavity with an open outlet, of which a half model is shown in Figure 3.6, which will be compared with the flow described in section 2.7.2. After a time, equal to the time required to fill the cavity in the filling stage as calculated in section 2.8.1.1, the outlet is closed and the second flow case which is the post–filling stage is simulated using the half model of the cavity as shown in Figure 3.7.

3.5.1 Continuous flow through a cavity with an open inlet

In this flow case the same pressure boundary conditions as in the GHS model are specified in the GN model. A zero normal pressure gradient is specified at the inlet boundary since a specific inlet velocity is specified at the centres of the control volumes at this boundary. The centres of these control volumes coincides with the first row of nodes away from the inlet. Atmospheric pressure is specified at the open outlet boundary. Zero pressure gradients are specified at the boundaries in the y direction, i.e. at the symmetry line and at the fixed boundary where $y = 0,b$ since there is no flow across these boundaries.

The following boundary conditions are specified for the velocity components u and v. A zero normal gradient is specified for u at the outlet boundary and at the symmetry line. At the fixed boundary u is zero since a non–slip boundary condition is assumed. At the inlet v is zero since the specified inflow is in the x direction. At the outlet a zero normal gradient boundary condition is specified for v. At the symmetry line and at the fixed boundary the zero pressure gradients

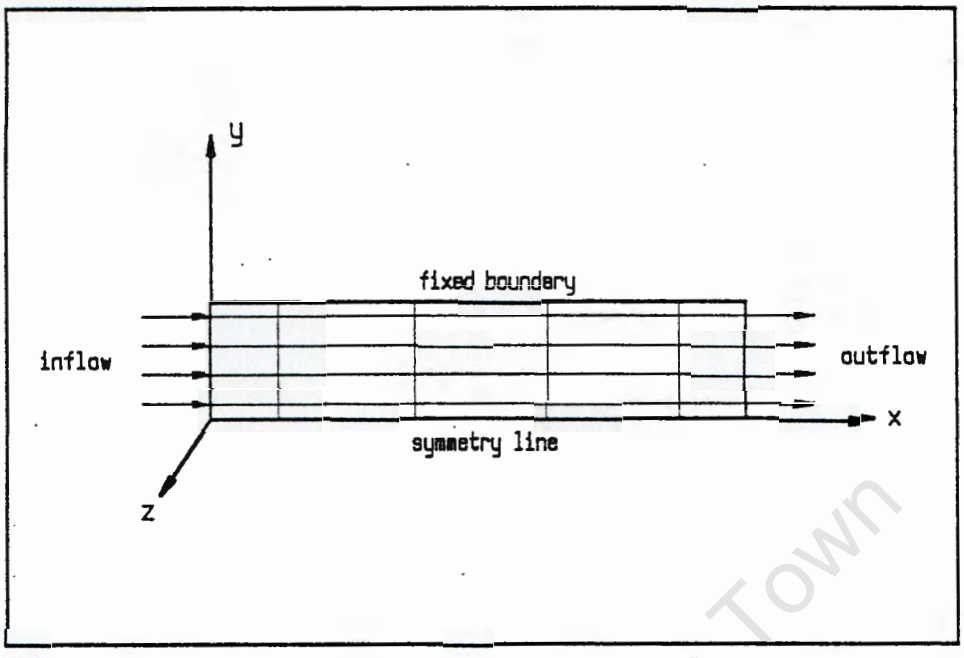

FIGURE 3.6 Geometry of the model for transient flow through a cavity

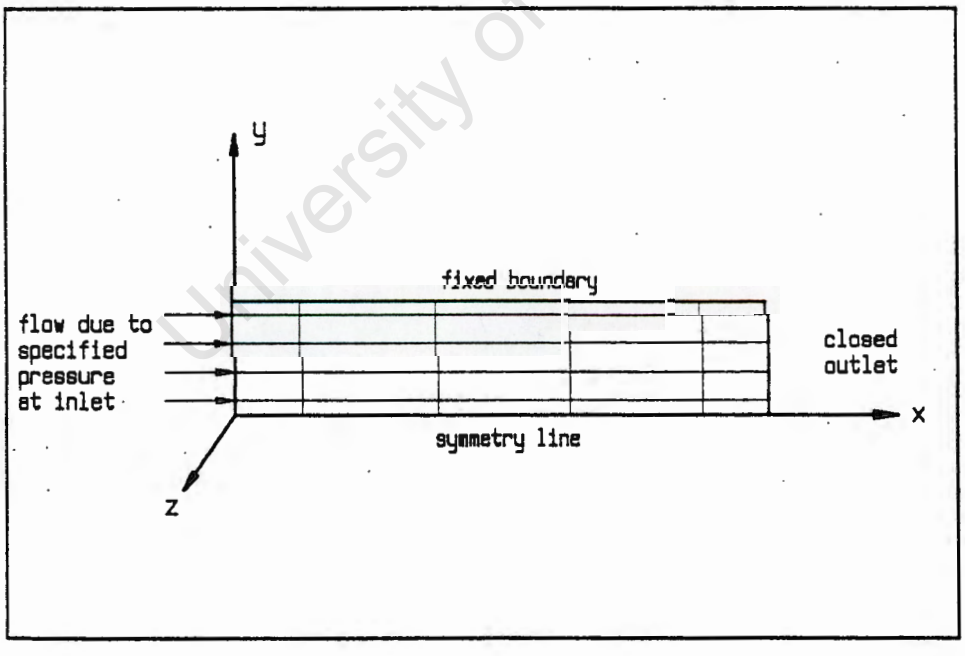

FIGURE 3.7 Geometry of the model for the post–filling stage which is closed at a specified instant

discribed above will result in a zero v velocity since there is no flow in the y direction across these boundaries. The abovementioned boundary conditions will be incorporated in equations (3.68) for the pressure correction and equations (3.67a) and (3.67b) for u and v (see p. 110) by specifying the coefficients a_{nb} at the boundaries.

The boundary conditions for the other variables are specified, as in the GHS model, on the boundaries where these variables are not calculated. At the inlet and outlet boundaries zero normal gradients are specified for the viscosity. No boundary condition is specified at the wall or fixed boundary where the viscosity is calculated. At the symmetry line a zero normal gradient boundary condition is specified. A zero normal gradient is also specified for the density at the symmetry line. At all the other boundaries the density is calculated. Zero normal gradients are specified for the temperature at the symmetry line and at the outlet. A constant temperature equal to the temperature of the inflowing melt is specified at the inlet. At the fixed boundary a constant wall temperature equal to the mould temperature is specified. Alternatively a heat transfer coefficient can be specified.

3.5.2 Post–filling stage

The boundary conditions for the pressures in the post–filling stage are the same as for the GHS model. A constant pressure is specified at the inlet boundary and a zero normal pressure gradient is specified at the closed outlet. The boundary conditions for the velocity components in the post–filling stage are as follows. At the outlet u and v are specified to be zero and at the inlet boundary where the pressure is known zero normal gradients are specified for u and v. At the fixed boundary u is zero since a non–slip boundary condition is assumed and at the symmetry line a zero normal gradient is specified. Since there is no flow in the y direction across the symmetry line or the fixed boundary, v is specified to be zero at these boundaries. The boundary conditions for the other variables are the same as in section 3.5.1 above.

3.6 Initial values

Following are the initial values for the two flow cases described above.

3.6.1 Continuous flow through a cavity with an open outlet

Only the velocity at the inlet, which is uniform through the thickness, is specified to have a fixed value. Initial values need to be specified for the other variables. Since the viscosities vary as much as three orders of magnitude through the cavity thickness for highly viscous shear flow, the solution algorithm will not converge if reference values for the pressure or the viscosity are specified as initial values through the domain. The solution algorithm converges only if the initial values are properly chosen. Since the objective is to compare the GN and GHS models, the values of all the variables (except the velocity at the inlet), obtained after a few time–steps with the transient GHS model solving the same flow case, will be used as initial values for the GN model. This choice of initial values is appropriate since the influence of the Hele–Shaw approximations can then be determined by comparing the final results of the GN and GHS models at a specific time.

In the case of a steady–state solution the values of the converged solution obtained with the GHS model are used as initial values in the GN model. In this way the effect of the Hele–Shaw approximations can be determined by investigating the deviation of the GN solution from the steady–state GHS solution used as initial values.

3.6.2 Post–filling stage

Since the objective is to compare the GN and GHS models, the same initial values have to be used in both models. Therefore the results obtained with the GHS model at the end of the filling stage will be used as initial values for the post–filling stage when it is solved with the GHS as well as the GN models. The inlet pressure at the end of the filling stage, calculated with the GHS model, is used as the constant holding pressure for the post–filling stage.

3.7 Solution algorithm

The derivation of the equations reported by Patankar (1984), to be used in the Pressure–Implicit Split–operator (PISO) algorithm described by Issa (1986), is given. For the purpose of this thesis the equations are extended to include the density and non–Newtonian viscosity for weakly compressible non–Newtonian flow. The PISO algorithm is extended to include the calculation of the density, ρ, and the non–Newtonian viscosity, η, using the constitutive equations in section 2.4.

3.7.1 Derivation

Let p* be the guessed pressure field

and let

$$\rho = \rho^* + \rho' \tag{3.49a}$$

$$u = u^* + u' \tag{3.49b}$$

$$v = v^* + v' \tag{3.49c}$$

$$p = p^* + p' \ , \tag{3.49d}$$

where the superscripts, * and $'$, indicate, respectively, the tentative value and the correction to obtain the corrected value. The tentative velocity u^* is obtained from the discretized momentum equation (3.33), by using the guessed pressure (for more detail see Patankar, 1984).

After including $a_T^u \cdot u_P^{t-1}$ and S^u in a new term S_P^u, the momentum equation (3.33) becomes :

$$a_P^u u_P^* = \Sigma a_{nb}^u u_{nb}^* + S_P^u + (p_{i,j}^* - p_{i+1,j}^*)\Delta y \ . \tag{3.50}$$

The velocity u based on the correct pressure p is given by

$$a_P^u u_P = \Sigma a_{nb}^u u_{nb} + S_P^u + (p_{i,j} - p_{i+1,j})\Delta y \ . \tag{3.51}$$

Substracting (3.50) from (3.51) gives

$$a_P^u u_P' = \Sigma a_{nb}^u u_{nb}' + (p_{i,j}' - p_{i+1,j}')\Delta y \ . \tag{3.52}$$

In the Semi–Implicit Method for Pressure–Linked Equations (SIMPLE), equation (3.52) is simplified (Patankar, 1984) by neglecting the term $\Sigma a_{nb}^u \, u_{nb}'$ in (3.52), resulting in

$$u_P' = \frac{\Delta y}{a_P^u} \cdot (p_{i,j}' - p_{i+1,j}') \ . \tag{3.53}$$

Since, from (3.49b), $u_P' = u_P - u_P^*$,

we get $$u_P = u_P^* + D_P^u \cdot (p_{i,j}' - p_{i+1,j}') \ , \tag{3.54}$$

where $$D_P^u = \frac{\Delta y}{a_P^u} \ . \tag{3.55}$$

Similarly $$v_P = v_P^* + D_P^v \cdot (p_{i,j}' - p_{i,j+1}') \ , \tag{3.56}$$

where $$D_P^v = \frac{\Delta x}{a_P^v} \ . \tag{3.57}$$

From equations (3.54) and (3.56) we get the velocity–correction formulas (Patankar, 1984) :

$$u_e' = D_e^u \cdot (p_P' - p_E') \ , \tag{3.58a}$$

$$u_w' = - D_w^u \cdot (p_P' - p_W') \ , \tag{3.58b}$$

$$v_n' = D_n^v \cdot (p_P' - p_N') \ , \tag{3.58c}$$

$$v_s' = - D_s^v \cdot (p_P' - p_S') \ . \tag{3.58d}$$

From equations (3.49), neglecting $\rho' u'$,

$$\rho u = (\rho^* + \rho')(u^* + u') = \rho^* u^* + \rho' u^* + u' \rho^* . \tag{3.59}$$

Since $\frac{\partial T}{\partial t}$ is much smaller than $\frac{\partial p}{\partial t}$ as discussed in section 3.4, we can define $\rho = K \cdot p$ where $K = \frac{\partial \rho}{\partial p}$. For weakly compressible flow (defined in section 2.2.1) we get

$$\rho_e' = (K_P p_P' + K_E p_E')/2 \ , \tag{3.60a}$$

$$\rho_w' = (K_P p_P' + K_W p_W')/2 \ , \tag{3.60b}$$

$$\rho_n' = (K_P p_P' + K_N p_N')/2 \ , \tag{3.60c}$$

$$\rho_s' = (K_P p_P' + K_S p_S')/2 \ . \tag{3.60d}$$

Substitution of (3.59) and (3.60) into the continuity equation (3.27) gives

$$\frac{(\rho_P^* + K_P p_P' - \rho_P^{t-1})}{\Delta t}\cdot\Delta x\Delta y + (\rho_e^* u_e^*\cdot\Delta y - \rho_w^* u_w^*\cdot\Delta y)$$

$$+ (\rho_n^* v_n^*\cdot\Delta x - \rho_s^* v_s^*\cdot\Delta x) + (K_P p_P' + K_E p_E')\cdot u_e^*\cdot\Delta y/2$$

$$- (K_P p_P' + K_W p_W')\cdot u_w^*\cdot\Delta y/2 + (K_P p_P' + K_N p_N')\cdot v_n^*\cdot\Delta x/2$$

$$- (K_P p_P' + K_S p_S')\cdot v_s^*\cdot\Delta x/2 + \rho_e^* D_e^u(p_P' - p_E')\Delta y$$

$$- \rho_w^* D_w^u\cdot(p_W' - p_P')\Delta y + \rho_n^* D_n^v\cdot(p_P' - p_N')\Delta x$$

$$- \rho_s^* D_s^v\cdot(p_S' - p_P')\Delta x = 0 . \qquad (3.61)$$

Equation (3.61), the pressure correction equation, can be rewritten as

$$a_P p_P' = a_N p_N' + a_S p_S' + a_E p_E' + a_W p_W' + S' \qquad (3.62)$$

where
$$a_E = \rho_e^* D_e^u\cdot\Delta y - K_E u_e^*\Delta y/2 \qquad (3.63a)$$

$$a_W = \rho_w^* D_w^u\cdot\Delta y + K_W u_w^*\Delta y/2 \qquad (3.63b)$$

$$a_N = \rho_n^* D_n^v\cdot\Delta x - K_N v_n^*\Delta x/2 \qquad (3.63c)$$

$$a_S = \rho_s^* D_s^v\cdot\Delta x + K_S v_s^*\Delta x/2 , \qquad (3.63d)$$

and $$a_p = \rho_e^* D_e^u \cdot \Delta y + \rho_w^* D_w^u \cdot \Delta y + \rho_n^* D_n^v \cdot \Delta x + \rho_s^* D_s^v \cdot \Delta x$$

$$+ K_p u_e^* \Delta y/2 - K_p u_w^* \Delta y/2$$

$$+ K_p v_n^* \Delta x/2 - K_p v_s^* \Delta x/2 + K_p \cdot \frac{\Delta x \Delta y}{\Delta t} , \qquad (3.64)$$

and

$$S' = -\left[\frac{(\rho_P^* - \rho_P^{t-1})}{\Delta t} \cdot \Delta x \Delta y + \rho_e^* u_e^* \cdot \Delta y - \rho_w^* u_w^* \cdot \Delta y + \rho_n^* v_n^* \cdot \Delta x - \rho_s^* v_s^* \cdot \Delta x\right] . \qquad (3.65)$$

Therefore $$a_P = a_N + a_S + a_E + a_W + K_P \cdot \frac{\Delta x \Delta y}{\Delta t} . \qquad (3.66)$$

Equation (3.62), which is similar to the pressure correction equation given by Patankar (1984), but which includes terms representing weakly compressible flow, is used in the PISO algorithm to solve for the pressure corrections.

3.7.2 PISO algorithm

The Pressure–Implicit Split–Operator (PISO) algorithm, as described by Issa (1986), is used to solve the governing equations after extending it to include the calculations of the density and the non–Newtonian viscosity using the constitutive equations given in section 2.4.

The PISO algorithm uses a two–stage predictor–corrector sequence. It satisfies the continuity and momentum equations more closely at each cycle of iteration than the SIMPLE algorithm (Patankar, 1984). As a consequence it has improved the computational efficiency, as reported by

Benodekar et al., (1985) and has therefore been chosen for the purposes of this thesis.

Following Issa (1986), the solution of the governing equations using the PISO algorithm is given for the flow cases considered in this chapter. The PISO algorithm uses a number of successive updates for the pressure and velocity fields in the endeavour to satisfy continuity and momentum simultaneously. The superscripts *, ** and *** denote intermediate field values obtained during the splitting process.

Predictor step

(a) Guess a pressure field p^* for the entire domain.

(b) Solve for the velocities u^* and v^*, using equation (3.50) for u^* and a similar equation for v^* :

$$a_P^u \, u_P^* = \Sigma a_{nb}^u \, u_{nb}^* + S_P^u + (p_{i,j}^* - p_{i+1,j}^*)\Delta y \ , \tag{3.67a}$$

$$a_P^v \, v_P^* = \Sigma a_{nb}^v \, v_{nb}^* + S_P^v + (p_{i,j}^* - p_{i,j+1}^*)\Delta x \ . \tag{3.67b}$$

First corrector step

(c) Solve for the pressure corrections, p', from (3.62) :

$$a_P p_P' = a_N p_N' + a_S p_S' + a_E p_E' + a_W p_W' + S'$$

$$= \Sigma a_{nb}^p \, p_{nb}' + S' \ . \tag{3.68}$$

(d) Calculate the new pressure field from

$$p_P^{**} = p_P^* + p_P' \ . \tag{3.69}$$

(e) Update the pressures at the boundaries using the boundary conditions.

(f) Calculate the density, ρ^{**}, using p^{**} in the equation of state described in section 2.4.

(g) Calculate the velocities u^{**} and v^{**} using equations (3.54) and (3.56) as follows :

$$u_P^{**} = u_P^{*} + D_P^u \cdot (p'_{i,j} - p'_{i+1,j}) \,, \tag{3.70a}$$

$$v_P^{**} = v_P^{*} + D_P^v \cdot (p'_{i,j} - p'_{i,j+1}) \,. \tag{3.70b}$$

Second corrector step

(h) Solve for the pressure correction, p'', from (3.62), using u^{**}, v^{**} and ρ^{**} :

$$a_P p''_P = \Sigma a_{nb}^P p'' + S'' \,, \tag{3.71}$$

where $$S'' = -\left[\frac{(\rho_P^{**} - \rho_P^{t-1})}{\Delta t} \cdot \Delta x \Delta y + \rho_e^{**} u_e^{**} \cdot \Delta y - \rho_w^{**} u_w^{**} \cdot \Delta y + \rho_n^{**} v_n^{**} \cdot \Delta x - \rho_s^{**} v_s^{**} \cdot \Delta x\right] \,. \tag{3.72}$$

(i) Calculate the velocities u^{***} and v^{***} using

$$u_P^{***} = u_P^{**} + (\Sigma a_{nb}^u u'_{nb})/a_P^u + D_P^u \cdot (p''_{i,j} - p''_{i+1,j}) \,, \tag{3.73a}$$

$$v_P^{***} = v_P^{**} + (\Sigma a_{nb}^v v'_{nb})/a_P^v + D_P^v \cdot (p''_{i,j} - p''_{i,j+1}) \,. \tag{3.73b}$$

where $u_P' = u_P^{**} - u_P^{*}$, (3.74a)

and $v_P' = v_P^{**} - v_P^{*}$. (3.74b)

(j) Calculate the new pressure field from

$$p_P^{***} = p_P^{**} + p_P'' \, . \tag{3.75}$$

(k) Update the pressures at the boundaries.

(l) Calculate the density.

(m) Calculate the viscosities using the viscosity model in section 2.4.

(n) Calculate the temperatures using the energy equation (3.42).

(o) The pressure p^{***} is now treated as the guessed pressure p^{*} in step (a) and the corresponding density is ρ^{*}. Steps (b) to (n) are repeated until the calculations converge for the current time–level.

(p) The algorithm is repeated for the next time–level, using the pressures obtained in the previous time–step as the new "guessed" pressure field in step (a).

3.7.3 Solutions for two different flow cases

The solutions for the two flow cases described above, which will be solved in chapter 4 for the purposes of the comparisons, are discussed. A numerical grid of 18x10 control volumes will be used for the GN calculations.

3.7.3.1 Flow through a cavity with an open outlet

For the purpose of comparing the GHS and GN models, a transient and a steady–state solution will be obtained for this flow case. A model of the geometry that will be used to solve this flow case has been shown in Figure 3.6 (p. 102).

The transient solution is obtained with the PISO algorithm, after adapting it for the type of flow considered in this thesis, as follows. Although the fully implicit scheme used here is unconditionally stable, very small time–steps are required to get the correct transient development of the solution. Larger time–steps may be used but will not result in a time–step independent solution. The small time–steps used here are still orders of magnitude larger than would have been required if an explicit scheme were used. In the latter case the time–steps would have been 10^{-11} to 10^{-13} s mainly as a result of the large viscosities. Since the velocity field develops much faster than the temperature field, the small time–steps used to solve the temperatures accurately are not small enough to solve the velocities accurately in time. Impractical small time–steps are required to solve the velocities which are therefore solved iteratively within each time–step by neglecting, in the momentum equations, the $\frac{\partial}{\partial t}$ terms. The $\frac{\partial}{\partial t}$ terms in the continuity and energy equations are retained in the PISO algorithm and these equations are solved as described above. To obtain a time–step independent solution for this flow case initial time–steps of 10^{-7} s or smaller are required as will be shown in chapter 4.

Although the PISO algorithm is cast in a time–dependent form, it is also useful for steady–state calculations (Issa, 1986). A steady–state solution is obtained by neglecting the $\frac{\partial}{\partial t}$ terms in the continuity, momentum and energy equations in the PISO algorithm.

3.7.3.2 Post–filling stage

A transient solution for the post–filling stage is obtained with the PISO algorithm after neglecting the $\frac{\partial}{\partial t}$ terms in the momentum equations but retaining them in all the other equations as described in section 3.7.3.1. A model of the geometry that will be used to solve the post–filling stage has been shown in Figure 3.7 (p. 102).

3.8 Summary

A two–dimensional numerical model, which uses the PISO algorithm to solve for the three hydrodynamic variables u, v and p simultaneously, have been described in this chapter. Weakly compressible, non–Newtonian flow under non–isothermal conditions is modelled with the GN model. The same constitutive equations for generalized Newtonian materials as in the GHS model are used. The GN model has been developed for the purpose of comparing it with the GHS model to determine the influence of the Hele–Shaw approximations on the solution. To achieve this objective the solution of flow through a cavity with an open outlet and the solution of the post–filling stage in the cavity with a closed outlet will be used. The solution algorithms for these two flow cases have been discussed in this chapter. In the next chapter these flow cases will be simulated with the GN and GHS models and the results of the two models compared.

CHAPTER 4

4 COMPARISON BETWEEN THE GHS AND GN MODELS

4.1 Introduction

In this chapter the solutions obtained with the generalized Hele–Shaw model are compared with those of the generalized Newtonian model to determine the influence of the Hele–Shaw approximations used in the GHS model. The approach used in the GHS model is to solve for one hydrodynamic variable, p, only. The velocity components are derived from the pressures. The approach in the GN model is to solve for the velocity components, u and v, and the pressure, p, using the Navier–Stokes equations without the Hele–Shaw approximations. The difference between the results obtained with these two approaches is therefore an indication of the influence of the Hele–Shaw approximations.

The GHS and GN models are compared as follows : firstly, the solutions obtained for two specific flow cases are compared. Secondly, parametric studies are done to compare the solutions of the GHS and GN models for a wider range of flow cases represented by different Reynolds numbers.

4.2 Domains

The calculational planes for the GHS and GN models are given in Figure 2.1 (p. 34) and Figure 3.1 (p. 83) respectively. The GHS model is solved on the two–dimensional x–z plane through the centre line of the cavity. The GN model is solved on a section through the thickness of the cavity. The section is taken in the x direction, which is the direction of flow, through p1, p2 and p3 and lies in the x–y plane. One–dimensional plane flow, which is independent of z, is considered for the purposes of the comparisons.

initial values in the GN model. The final results of the two models are then compared. The effects of the Hele–Shaw approximations are given by the degree to which the GN model changes the results of the GHS model.

The profiles, through the thickness, of the temperature and the density are calculated at node p2 (shown in Figure 2.8, p.60). At p2, which is approximately half way between the inlet and the end of the cavity, the flow is fully developed.

The temperature profiles at p2, obtained from the steady–state solutions of the GHS and GN models, are shown in Figure 4.1. Lines connecting the values calculated at the nodes represent the results of the GHS model while the results of the GN model are given as nodal values. The temperature profiles at p2 compare very well and the maximum deviation is less than 2° C or approximately 1%.

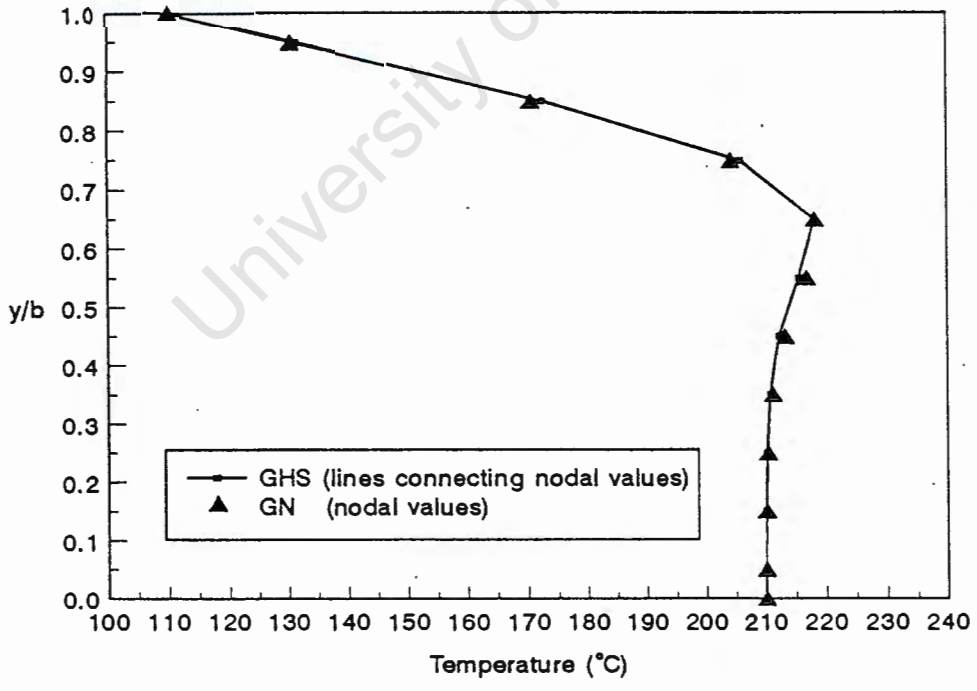

FIGURE 4.1 Temperature profiles for the GHS and GN models (steady–state)

As discussed in section 2.8.1.2 the influence of compressibility on the flow is very small. For the sake of comparing the two models, the density profiles at p2 are shown in Figure 4.2. The results of the GN model, given as points representing the nodal values, compare very well with the results of the GHS model shown as a curve fit through the values at the nodes.

The results in Figure 4.1 indicate that the specific forms of the energy equations used in the GHS and GN models, respectively, to calculate the temperatures are compatible and give similar results. The results in Figure 4.2 indicate that the equation of state used in both models to calculate the densities, which are pressure dependent, also give similar results although the pressures are not calculated in the same way by the two models. It is therefore concluded that the contribution of the temperatures and the densities, to any deviation that may be identified between the results obtained with the GHS and GN models, are negligible.

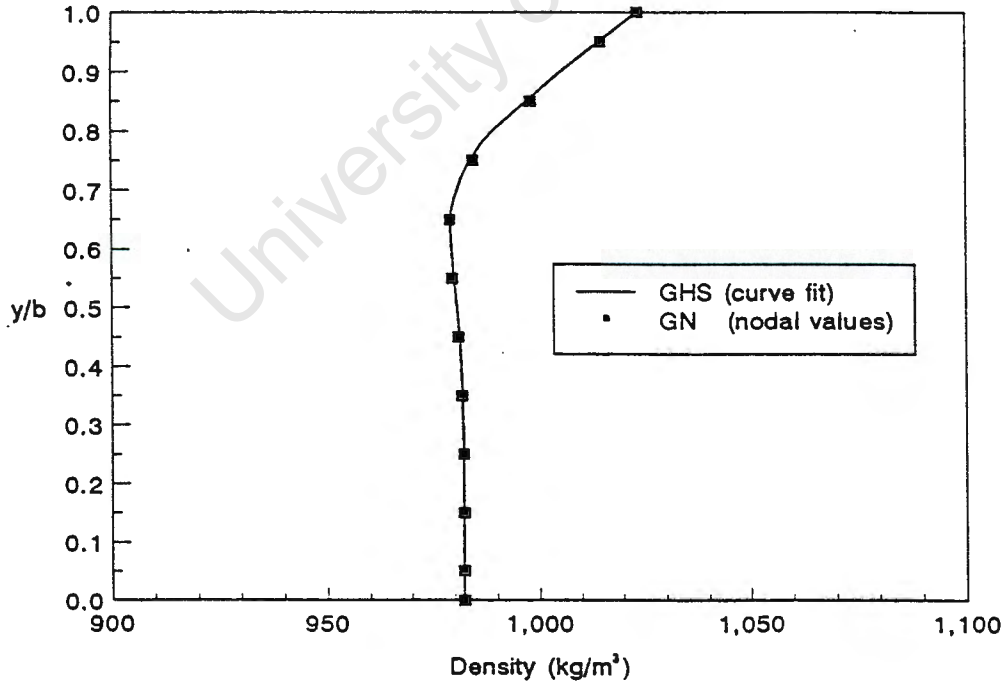

FIGURE 4.2 Density profiles for GHS and GN models (steady–state solution).

4.3.1.2 Transient solution of flow through a cavity with an open outlet

To compare the transient solutions of the GHS and GN models for this flow case, consider the same example as for the steady–state solution with an inlet flow rate of 20 cm^3/s, a melt temperature of 210° C and a wall temperature of 110° C.

To obtain time–step independence in the solution of the GHS model a time–step (dt) of $2{,}5.10^{-5}$ s is required. To obtain a similar time–step independent solution with the GN model, initial time–steps smaller than 5.10^{-8} s are required. The time–steps can be increased gradually as the calculations progress. The intermediate values of the variables obtained with the GHS model after 6 time–steps or 0,00015 s are used as initial values for the GN model since the numerical model requires properly chosen initial values to obtain a solution (as discussed in section 3.6.1).

The time–dependent development of the pressures and the u velocity profiles are compared to determine the influence of the Hele–Shaw approximations. If the values obtained with the GHS model, at an earlier time than 0,00015 s, were used as initial values in the GN model, even smaller time–steps would have been required in the GN model. The time–steps and initial values chosen for the GN model in this example are sufficient for the purpose of comparing the transient development of the pressures calculated with the two models.

The time–dependent development of the gap–averaged pressures at p1, p2, and p3 (see Figure 2.8, p. 60) in the cavity is shown in Figure 4.3. In the initial part of the development there is a slight difference between the pressures. If larger time–steps are used in the GN model, the difference becomes larger. The time–step independent GHS solution compares very well with the time–step independent GN solution for this flow case. To obtain time–step independence with the GN model a much smaller time–step than in the GHS model, is required. In the example considered the time–steps used in the GN model are 500 times

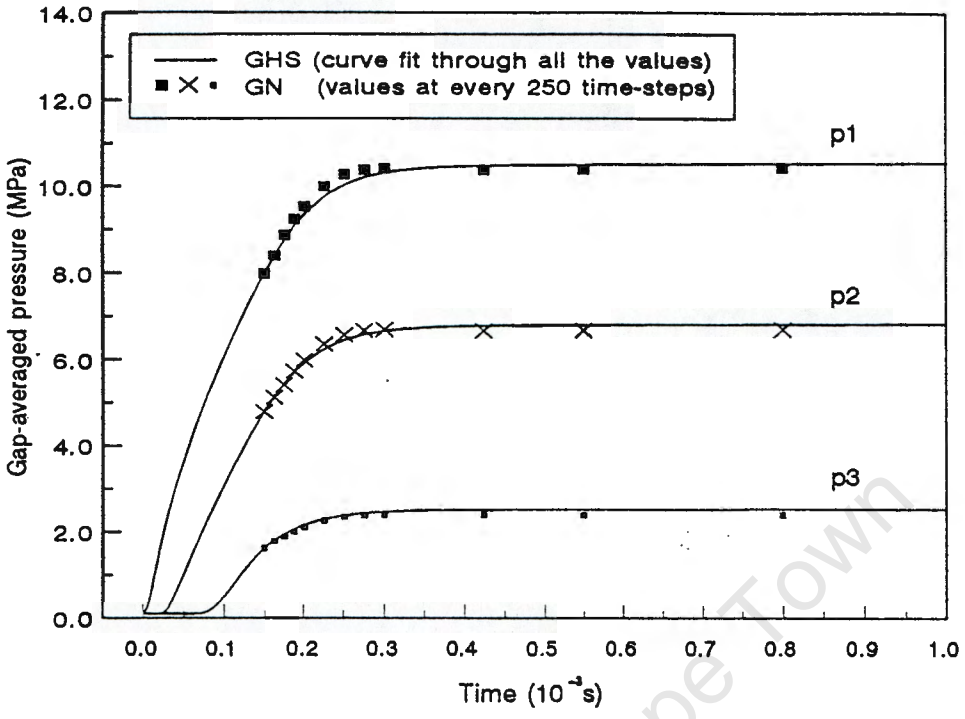

FIGURE 4.3 Time–dependent pressure development in the filling stage.

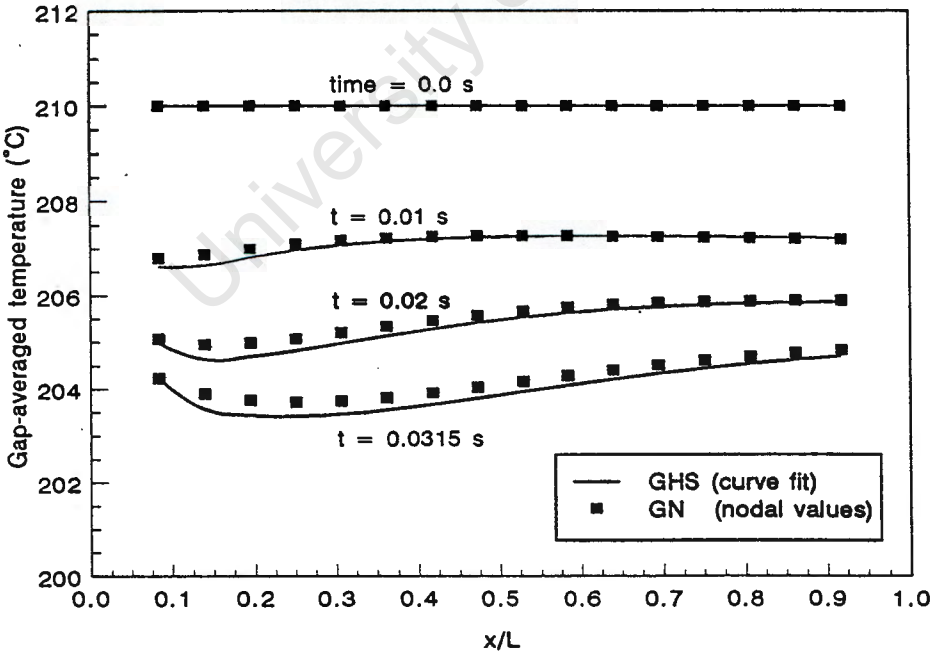

FIGURE 4.4 Time–dependent development of the gap–averaged temperatures

smaller. Only the first 1,0 x 10^{-3} s of the development is shown in Figure 4.3 to make the difference in the results for the chosen time–steps more visible.

The transient solutions of the two models can also be compared by comparing the development of the temperatures in the cavity. The temperatures develop at a much slower rate than the pressures. For the same example as above a steady–state solution for the filling stage under isothermal conditions is obtained. Keeping the solved values of all the other variables constant, the temperature is then calculated with a transient scheme. The time–dependent development of the gap–averaged temperatures is shown in Figure 4.4. The time– dependent temperatures calculated in the two models compare very well, again confirming that the energy equations in the two models give compatible solutions. The maximum deviation is 0,33° C which is less than 0,2%.

The profiles of the u velocity component at p2, at a time equal to the time that would have been required to fill the cavity and which has been calculated as 0,0315 s in section 2.8.1.1, are shown in Figure 4.5. The results of the GHS model are given as lines connecting the calculated nodal values. The results of the GN model are given as nodal values. The GN model, solving the full momentum equations, changes the velocity profile slightly. Near the fixed wall the velocities obtained with the GN model are smaller than those obtained with the GHS model. At the first node away from the fixed wall the velocities are 0,00075 m/s and 0,0044 m/s respectively. Near the centre line the GN solution give slightly larger velocities as compared to the GHS model. At the centre line the velocities are 1,547 m/s and 1,536 m/s.

Although the difference in the absolute values of the velocities are small, the difference in the **variation** of the velocities through the thickness results in different shear rates. The shear rate profiles at p2 are shown in Figure 4.6. The GHS results are represented by lines

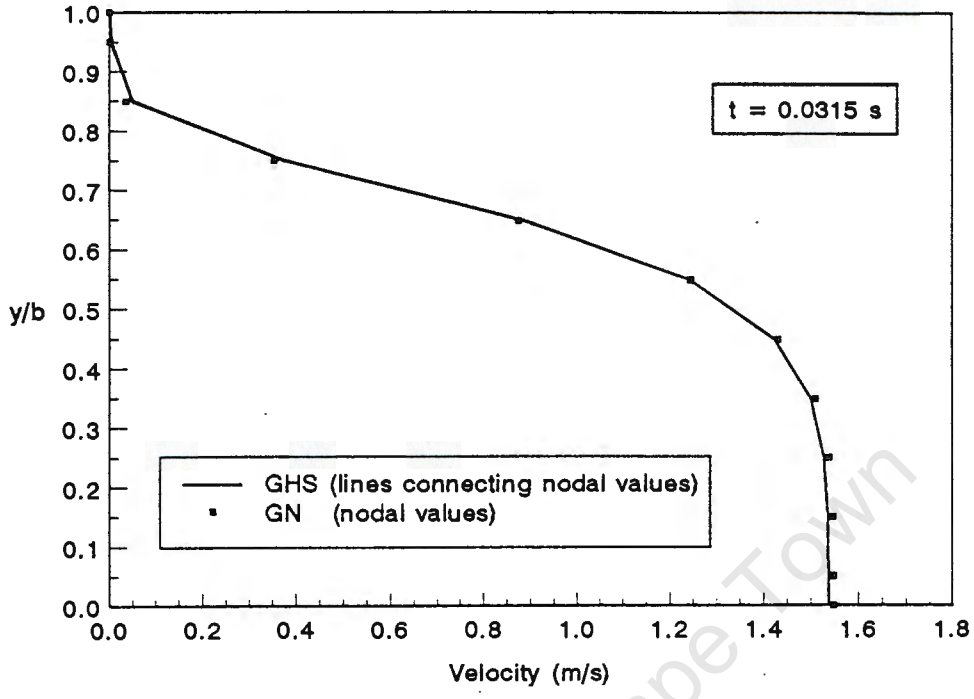

FIGURE 4.5 Profiles of the u velocity component in transient flow.

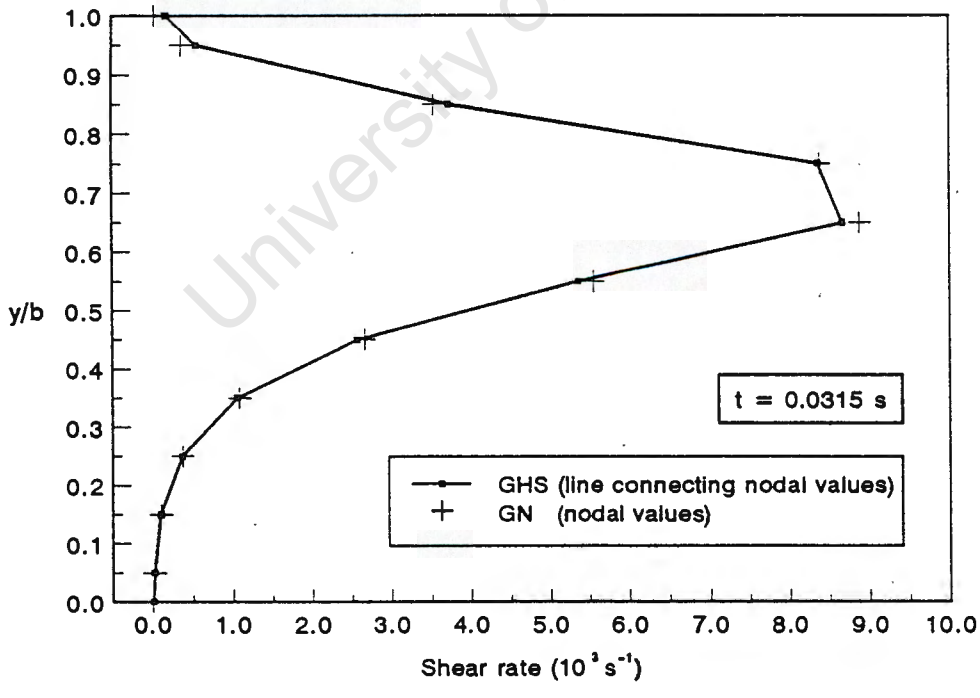

FIGURE 4.6 Shear rate profiles for transient solutions of GHS and GN models

connecting the values calculated at the nodes and the GN results are given as nodal values. Near the fixed wall the shear rates obtained with the GN model are smaller than that of the GHS model. At the first node away from the fixed wall the shear rates are $0{,}365.10^3\ s^{-1}$ and $0{,}549.10^3\ s^{-1}$ respectively. At the nodes near the middle of the half gap larger shear rates are obtained with the GN model. The maximum difference occurs where the shear rates are $8{,}88.10^3\ s^{-1}$ and $8{,}66.10^3\ s^{-1}$ respectively.

Figures 4.5 and 4.6 show that the differences in the absolute values of the velocity and the shear rate are small and that the results of the GHS and GN models compare well. Since the viscosity is shear–rate dependent, the difference in shear rates near the wall results in a large difference in the absolute viscosities as shown in Figure 4.7. At the wall the viscosity calculated by the GN model is much higher than the viscosity obtained with the GHS model. The viscosities at the wall, however, only have a numerical and not a physical meaning since the velocities are zero at the wall where a non–slip boundary condition is imposed. At the first node away from the wall the viscosity calculated with the GN model is also higher than that of the GHS model. Since the viscosity is a function not only of shear rate and temperature but also of pressure, the pressures at the nodes near the wall are also compared. The Hele–Shaw formulation assumes the pressure to be constant through the thickness. Although the GN model calculates different pressures through the thickness, the variation through the thickness at p2 is less than 0,01% for this flow case due to the characteristics of shear flow through a thin section. Furthermore at p2 the difference in the pressure at the wall, calculated with the GN model, and the constant pressure through the thickness, calculated with the GHS model, is only 2,23%. Therefore, since it was also shown in section 4.3.1 that the temperatures calculated with the two models are similar, the difference in the viscosities near the wall is mainly a result of the difference in shear rates due to the different velocity profiles.

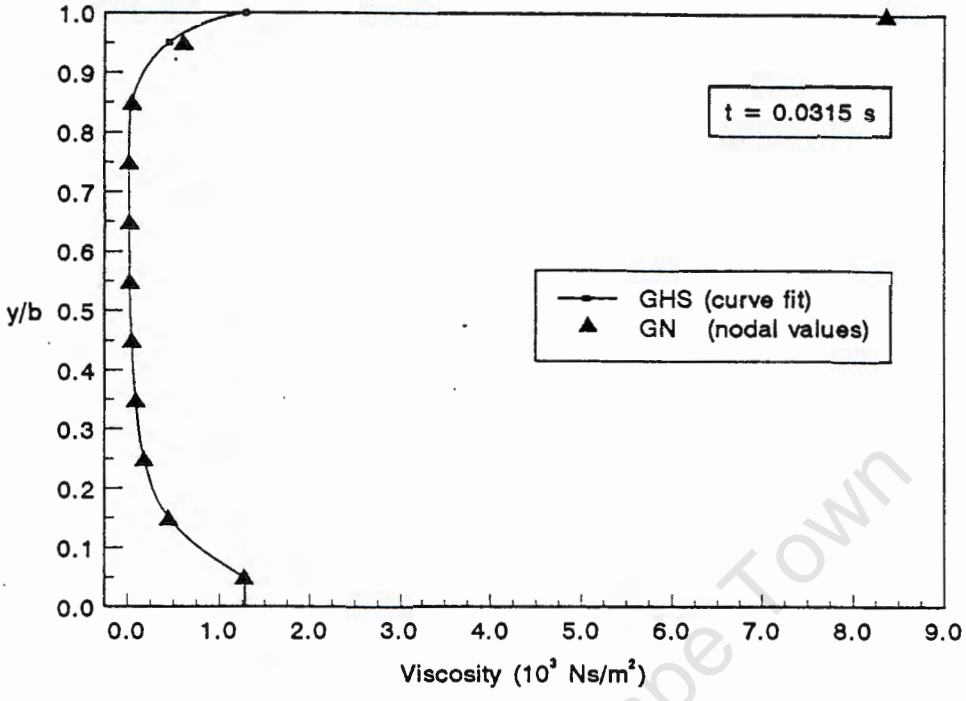

FIGURE 4.7 Viscosity profiles for transient solutions of GHS and GN models

The higher viscosities near the wall, calculated with the GN model, result in smaller velocities as was shown in Figure 4.5. At all the other nodes the viscosities calculated with the two models compare very well. Since the velocities near the wall are very small compared to the rest of the flow field, the influence of the large viscosities near the wall on the overall solution is small. This is confirmed by comparing the pressure drops.

The drop in the pressures at the centre line along the length of the cavity is shown in Figure 4.8, while the drop in the thickness–averaged pressures along the length of the cavity is shown in Figure 4.9. In both figures the pressure drop calculated with the GHS model is shown as a curve fitted through the calculated nodal values and the results of the GN model are shown as nodal values. The results in Figure 4.8 compare well and the maximum deviation which occurs at the first node away

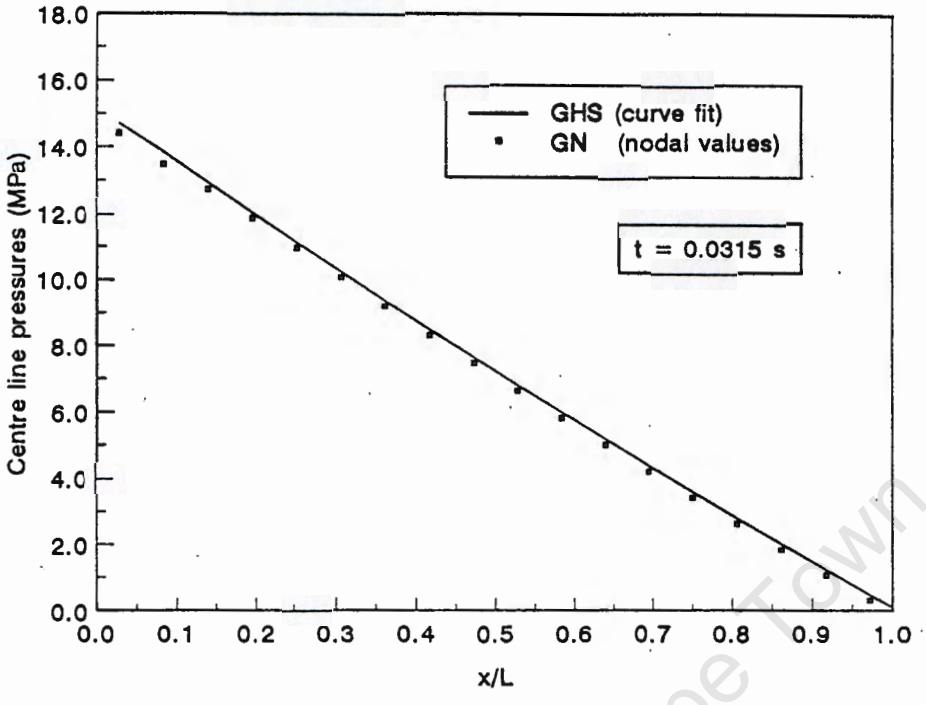

FIGURE 4.8 Drop in the pressures at the centre line of the cavity

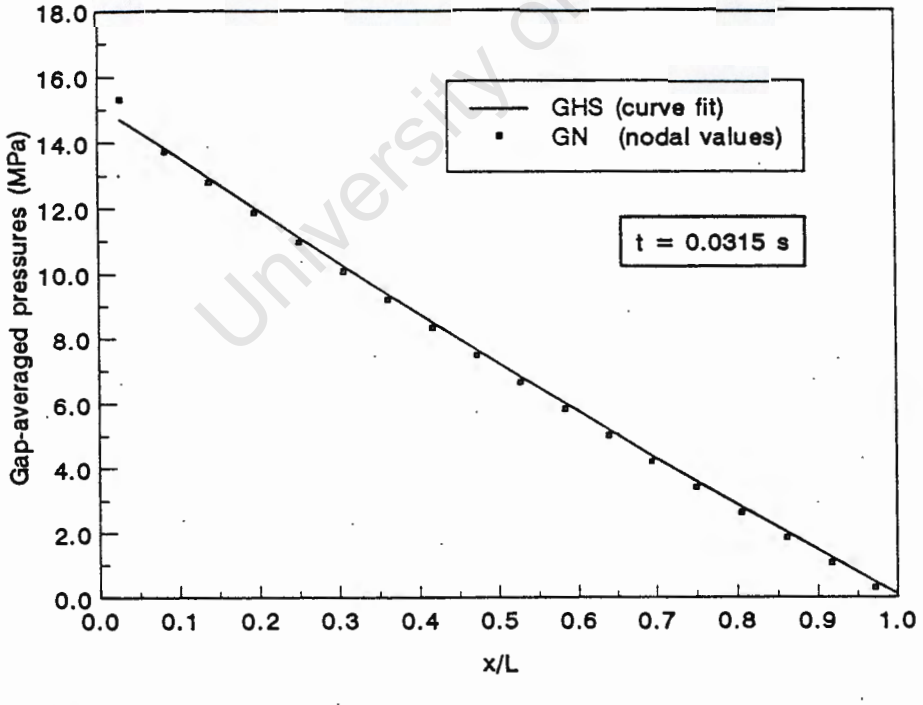

FIGURE 4.9 Drop in the gap–averaged pressures along the length of the cavity

from the inlet is 2,61%. The deviation at the inlet is 2,02%. However, since the GN model calculates different pressures through the thickness, the gap–averaged pressures are also compared in Figure 4.9. The maximum deviation between the pressures calculated with the GHS model, which are constant through the thickness, and the gap–averaged pressures calculated with the GN model is 3,9% at the inlet. At the first node away from the inlet the deviation is only 0,77%. The solutions obtained by using the different approaches of the GHS and GN models therefore compare very well, except at the inlet, indicating that the Hele–Shaw approximations have a small influence on the transient solution obtained for this flow case. The larger deviation of the pressures at the inlet will be discussed further in section 4.4.

4.3.2 Post–filling stage

The results of the transient solutions for the GHS and GN models obtained in section 4.3.1.2 above, at a time equal to the filling time of the cavity, are used as initial values for the post–filling stage. The value of the inlet pressure obtained at this instant is used as the constant holding pressure at the inlet for the post–filling stage. The post–filling stage is simulated until the pressures throughout the cavity are equal to the holding pressure as discussed in section 3.4. For the purpose of comparing the GHS and GN models, one–dimensional heat transfer after the melt has become stationary is not included as discussed in sections 2.8.3 and 3.4.

The time–dependent development of the gap–averaged pressures at p1, p2 and p3 (see Figure 2.9, p. 63) is shown in Figure 4.10. The initial pressures at these points are different due to the pressure drop along the cavity at the beginning of the post–filling stage. The pressures increase with time and eventually reach the same constant value. Only the first 0,005 s of the post–filling stage is shown in order to show more clearly the development of the pressures, which change much faster

in the first part of the post–filling stage than later on when the velocities become very small and when the pressures change very slowly.

A time–step (dt) of 10^{-5} s is required to obtain a time–step independent solution with the GHS model. Initial time–steps of 5.10^{-8} s are required to obtain a time–step independent solution with the GN model. The results of the GN model differ slightly from the GHS solution during the initial part of the post–filling stage. To make the difference in the pressure development visible only the solution obtained with initial time–steps of 10^{-7} s is shown. The difference becomes smaller if the initial time–steps in the GN model are decreased. For this example the pressures calculated with the two models are in excellent agreement at a time of approximately 4.10^{-3} s after the commencement of the post–filling stage. The pressures throughout the cavity, in both cases, reach the same constant value of 14,7 MPa after approximately 0,1 s.

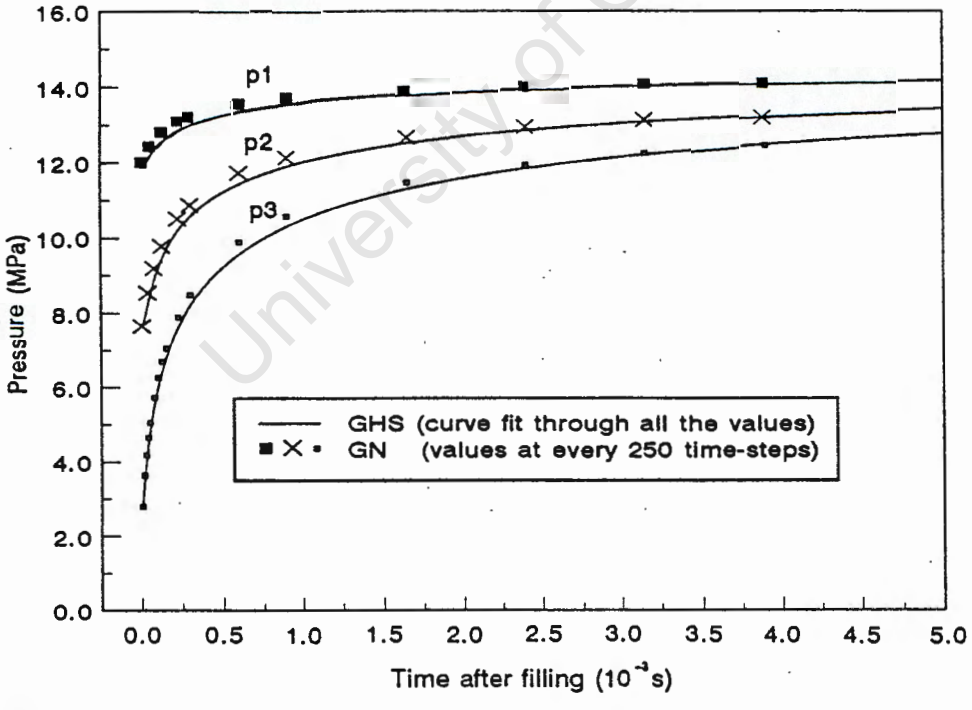

FIGURE 4.10 Time–dependent pressure development during the post–filling stage

4.4 Parametric studies

In section 4.3 the solutions of two specific flow cases obtained with the GHS and GN models, respectively, were compared. In this section parametric studies are preformed to compare the results of the two models for wider ranges of the inlet velocity and the gap thickness.

The Hele–Shaw formulation is based on the assumption that the pressure, which is the only hydrodynamic variable solved by the GHS model, is independent of y, the gap–wise dimension. The GN model calculates the pressure distribution through the thickness, i.e. in the gap–wise direction. Therefore the pressures, calculated with the GHS and GN models respectively, are used in the parametric studies with a view to comparing the two models.

For the purpose of the parametric studies consider the case of continuous flow through a cavity with an open outlet. By varying the half–gap dimension or the specified inlet velocity (which is equivalent to varying the specified inflow rate) different pressure fields will result in the cavities. For this flow case two constants, the Reynolds number, R_e, and $\bar{\bar{\tau}}^*$, which depends on the characteristic velocity, have been defined in section 2.2.1. For different values of $\bar{\bar{\tau}}^*$, different relations exist between R_e and $\bar{\bar{p}}$, the non–dimensional pressure, due to the particular form of the constitutive equations. These relations are shown in Figure 4.11 for the GHS model. The results were obtained for inlet velocities ranging from 0,5 m/s to 10 m/s and gap or thickness dimensions ranging from 0,5 mm to 10,0 mm.

Although the GHS model seems to give consistant results over a range of Reynolds numbers for different $\bar{\bar{\tau}}^*$ values, as shown in Figure 4.11, the results are not neccesarily valid since the GHS model is based on the assumption that the flow is predominantly shear flow in which the

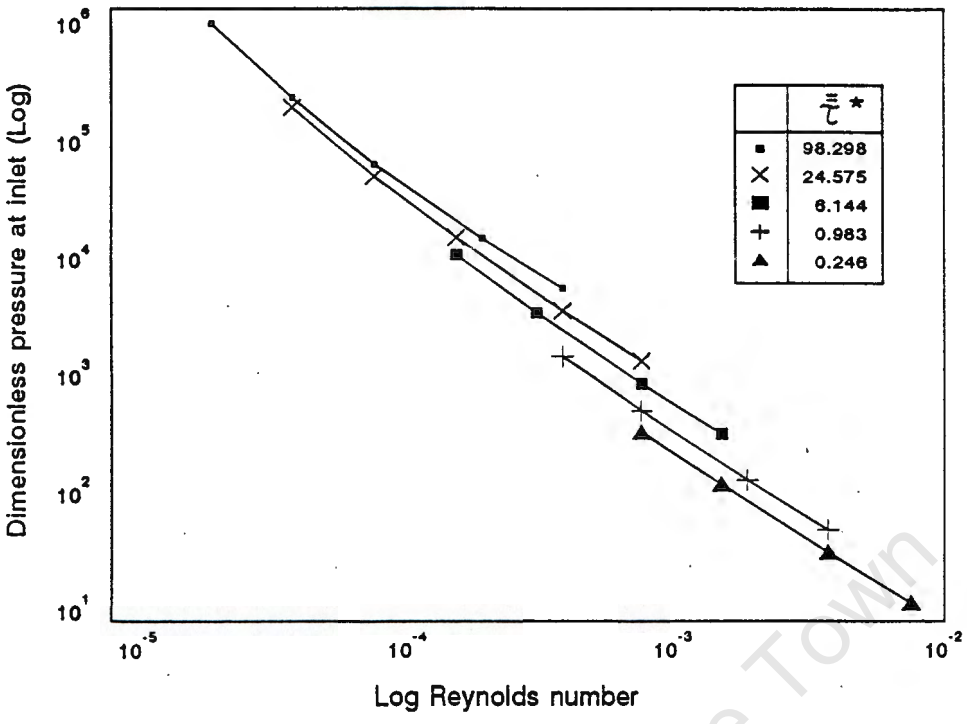

FIGURE 4.11 Parametric study of the results obtained with the GHS model

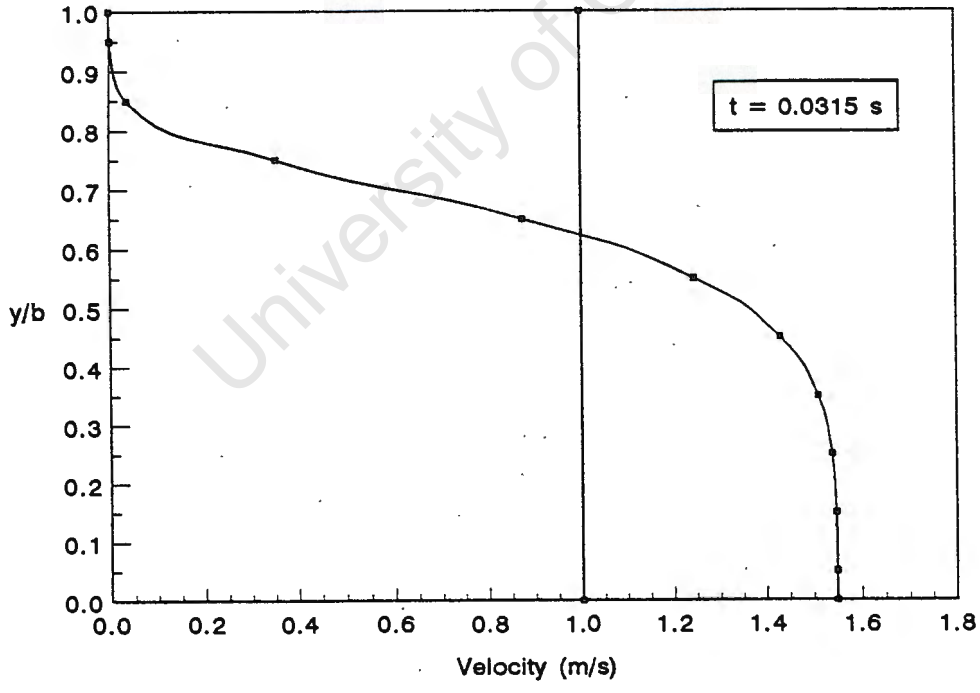

FIGURE 4.12 Typical velocity profiles for uniform inlet velocity changing to fully developed flow

inertial forces are much smaller than the viscous forces. In the GHS model the pressures are also assumed to be constant through the thickness or gap–wise direction while the GN model calculates the actual pressure distribution.

Another difference between the GHS and GN models is that a uniform inlet velocity is specified for the GN model while the GHS model assumes the velocities to be fully developed throughout the cavity. The inlet velocity specified for the GN model changes in the flow direction from the specified uniform distribution at the inlet to the velocity profile of fully developed flow. In Figure 4.12 the velocity profile of the fully developed flow at p2, in the flow case described in section 4.3.1.2 above, is given. The uniform velocity at the inlet is shown as a straight line. Once the flow is fully developed the change in the pressure through the thickness becomes very small as shown in Figure 4.13. At the inlet the pressure changes by 8,8% for this flow case. The maximum change in the pressure through the thickness occurs at the inlet and comparing these pressures will give an indication of the influence of the Hele–Shaw approximations on the results of the GHS model. The deviation between the pressures at the inlet, as calculated with the GHS and GN models, are shown in Figure 4.14. The percentage deviation of the pressures is defined as

$$\frac{\left|p_{GN} - p_{GHS}\right|}{p_{GN}} \times \frac{100}{1}, \qquad (4.1)$$

where p_{GN} is the thickness averaged pressure at the inlet calculated with the GN model and p_{GHS} is the inlet pressure, which is independent of y, as calculated with the GHS model.

In Figure 4.14 the deviation in the inlet pressures are given against the Reynolds numbers for different $\bar{\bar{\tau}}^*$ values. For each $\bar{\bar{\tau}}^*$ there is a R_e number for which the percentage deviation is a minimum. For smaller

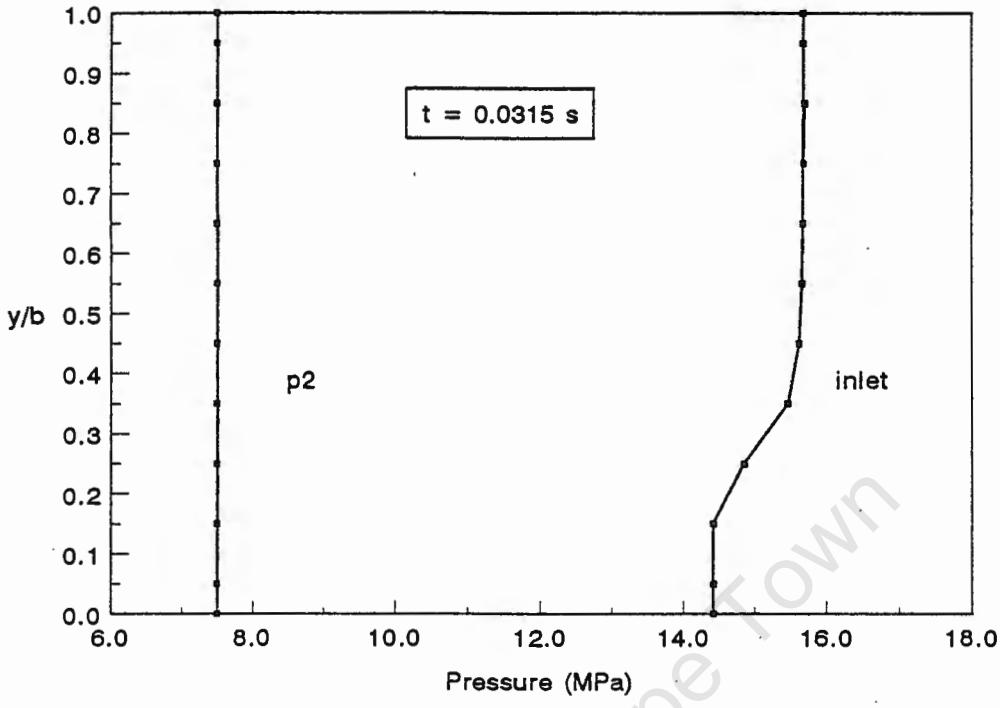

FIGURE 4.13 Pressure distribution through thickness calculated with GN model

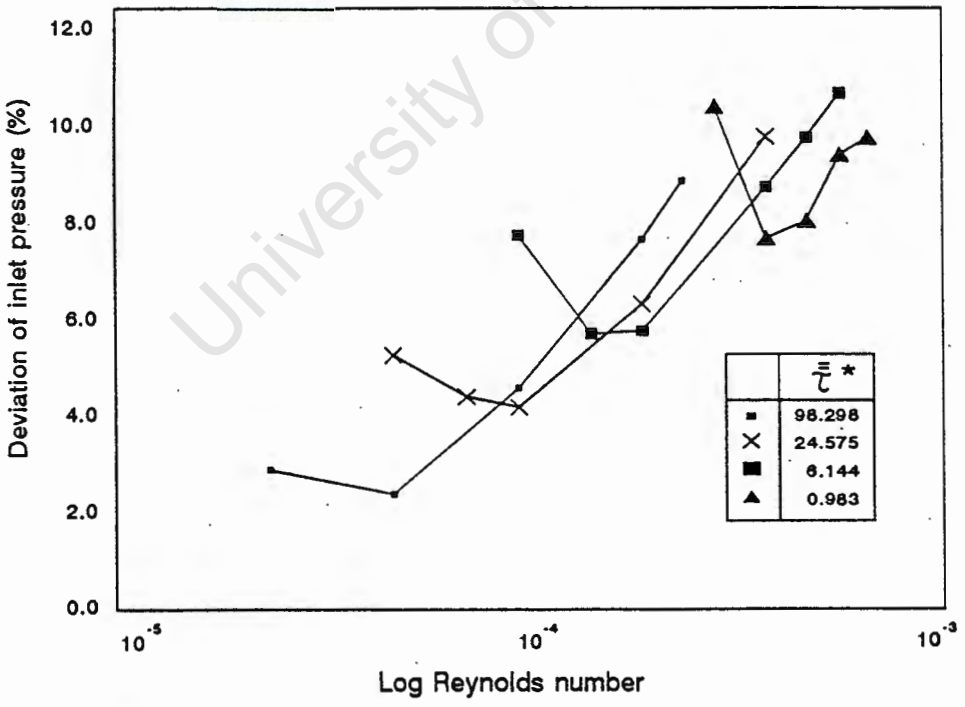

FIGURE 4.14 Deviation in pressures calculated with the GHS and GN models

values of R_e the deviation increases due to the higher pressures required for flow through thinner sections and due to the characteristics of the viscosity model (equation 2.83) which calculates viscosity as a function of pressure. For each $\bar{\bar{\tau}}^*$ value there is a minimum R_e number for which the viscosity model is applicable. This R_e number represents a thickness dimension of 0,5 mm (half–gap dimension, b, equal to 0,25 mm). For smaller values of b the required pressures at the inlet become so large that it falls beyond the applicability of this viscosity model.

Each $\bar{\bar{\tau}}^*$ value also has a maximum R_e number beyond which the GN model diverges from the GHS solution to such an extent that a solution cannot be obtained. This maximum value of R_e represents a thickness dimension of 5,0 mm in the case of $\bar{\bar{\tau}}^* = 9{,}83.10^{1}$, representing an inlet velocity of 0,5 m/s. For $\bar{\bar{\tau}}^* = 9{,}83.10^{-1}$, representing a 5 m/s inlet velocity, the maximum R_e number represents a thickness of 1,3 mm. At the maximum R_e values the percentage deviation lies in the vicinity of 10%. The influence of the Hele–Shaw approximations therefore makes the GHS solution unacceptable for higher R_e numbers. For $\bar{\bar{\tau}}^*$ values larger than $9{,}83.10^{-1}$, representing velocities larger than 5 m/s, the GN model cannot converge to a solution using the GHS results as initial values. This indicates that the solution of the uniform pressures, obtained with the GHS model, deviate from the pressure distribution through the thickness, calculated with the GN model, to such an extent that it is not an acceptable solution.

The relations between R_e and $\bar{\bar{p}}$, for different values of $\bar{\bar{\tau}}^*$, as obtained with the GN model, are shown in Figure 4.15. For each $\bar{\bar{\tau}}^*$ value in Figure 4.15 the maximum R_e number correlates with the maximum deviation shown in Figure 4.14 for the different values of $\bar{\bar{\tau}}^*$.

The parametric studies show that for each value of $\bar{\bar{\tau}}^*$, representing a

specific inlet velocity, the solution obtained with the GHS model is acceptable for a specific range of Reynolds numbers representing a range of thickness dimensions. They also show that the solution will become unacceptable for inlet velocities above a certain value.

The results of the parametric studies can be explained as follows : The GHS model is based on the approximations which assume that the pressure is constant through the thickness, that the inertial forces are negligible compared to the viscous forces and that there is no velocity component in the gap direction. These approximations are valid for injection moulding applications if the thickness dimension is small enough to ensure that the flow is predominantly shear flow and that the velocity component in the thickness direction is negligible. Due to the high viscosities of molten polymers the inertial forces will be much smaller than the viscous forces provided the Reynolds number, which is proportional to the product of the inlet velocity and the thickness dimension, is smaller than a certain value for each flow case.

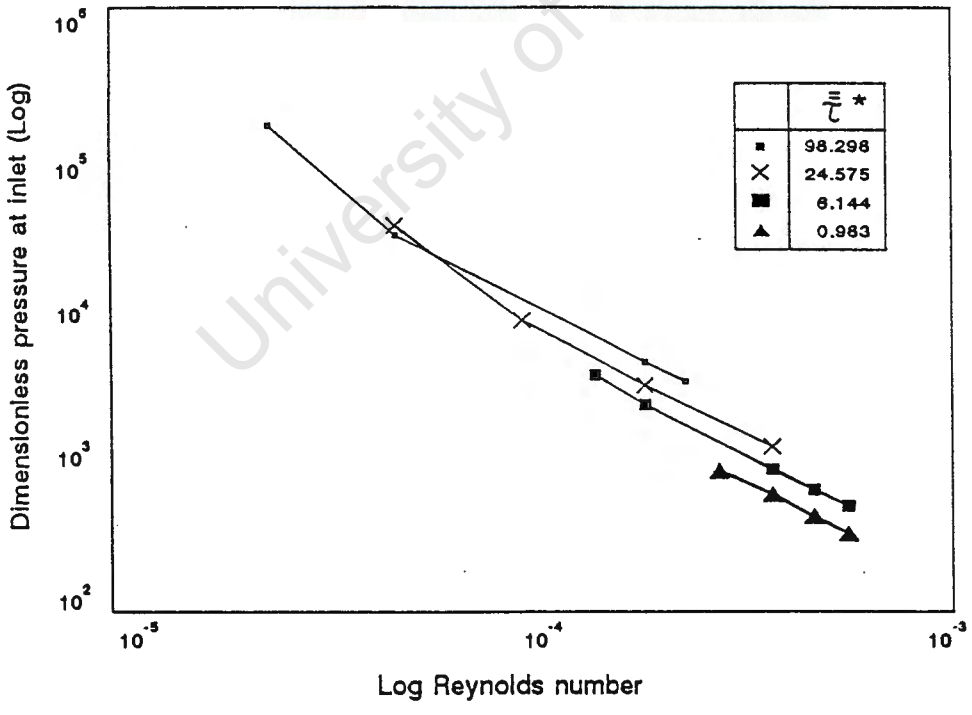

FIGURE 4.15 Parametric study of the results obtained with the GN model

4.5 Conclusions

The solutions for two specific flow cases, obtained with the generalized Newtonian model solving for pressure and velocity, have been compared with the results of the model based on the Hele–Shaw formulation. These comparisons have shown that the GHS model compares very well with the GN model which solves the full momentum equations. For these flow cases the inaccuracies due to the Hele–Shaw approximations are therefore small and the results of the GHS model are acceptable for the purpose of simulating the injection moulding process. The GHS model is also significantly faster than the GN model.

The parametric studies have shown that the applicability of the GHS model is limited to a specific range of Reynolds numbers. Although the GHS model apparantly gives solutions for R_e numbers beyond this range, these solutions deviate from the GN solutions to such an extent that the GHS solutions become unacceptable. This occurs when the thickness dimension is increased resulting in a velocity component in the thickness direction that is not negligible and flow that is not predominantly shear flow anymore, or when the ratio of the inertial forces to the viscous forces becomes larger as a result of the combined effect of higher inlet velocities and larger thickness dimensions.

The GN injection moulding model requires a much smaller time–step to obtain time–step independent transient solutions as compared to the GHS model. The solution algorithm for the GHS model described in chapter 2 is also much less involved than the PISO algorithm. Furthermore, the restriction on the GN model, that properly chosen initial values are required for convergence, does not apply to the GHS model.

The time efficiency and numerical simplicity of the GHS model as compared to the GN model make it a more practical model for personal computer–based simulations.

CHAPTER 5

5 REFINEMENT OF THE GHS MODEL

5.1 Introduction

The purpose of this chapter is, firstly, to refine the GHS model to include the cooling effects in the post–filling stage and to model material characteristics more accurately. Secondly, the simulation of one–dimensional flow, using the refined GHS model, and a two–dimensional flow case are demonstrated in example calculations.

The constitutive equations used in the previous chapters were chosen for computational simplicity, to enhance understanding of the numerical models and for the purpose of comparing the GHS and GN models. In this chapter an equation of state which models the solid and liquid phase densities is used in the GHS model. One–dimensional heat transfer calculations are also included to calculate the pressure decrease during cooling after the melt has become stationary. A viscosity model, which reflects the markedly increased temperature sensitivity of the viscosity at low temperatures, is also used to refine the GHS model. These refinements are specifically aimed at representing the material characteristics more accurately during the post–filling stage.

The refinement to include both the solid and liquid phase densities was developed specifically for the GHS model as reported in the literature (Chiang et al., 1991a). The refinement could not be incorporated in the GN model which does not include the Hele–Shaw approximations. For the purposes of the comparisons this refinement was therefore not included in the previous chapters.

One–dimensional flow was considered in the previous chapters for the purpose of the comparisons. In this chapter two–dimensional flow will also be demonstrated.

5.2 Refinement of the GHS model

An equation of state to model the solid and liquid phase densities and to calculate the pressure decrease during cooling, using one–dimensional heat transfer calculations, is given. A viscosity model, which reflects the markedly increased temperature sensitivity of the viscosity at low temperatures, is also given.

5.2.1 Equation of state and one–dimensional heat transfer

The effect of substantial cooling during the late post–filling stage was not taken into account in section 2.4.3. The Spencer–Gilmore equation of state (2.81) is valid for temperatures above T_g and makes no distinction between the solid and liquid phases which are present in the polymer during the post–filling stage. The Spencer–Gilmore equation may be used to model the density during the filling stage, when the temperatures are well above T_g and the polymer is in the liquid phase except for a very thin solidified layer next to the fixed wall. In the post–filling stage the cooling is more pronounced and as the temperatures drop below T_g the material solidifies progressively inward from the colder wall towards the centre of the cavity. This results in a solid and a liquid region on each side of the moving solid–liquid interface.

The classical empirical equation of state (1.2), proposed by Tait, can be used to describe the densities in both the liquid and solid regions. This is achieved (Chiang et al., 1991a) by using the double–domain Tait equation

$$\frac{1}{\rho} = v_s(p,T) = v_0(T)\left[1 - C\ln\left(1 + \frac{p}{B(T)}\right)\right] \qquad (5.1)$$

and representing $v_0(T)$ and $B(T)$ as follows :

$$v_o(T) = \begin{cases} b_{1,l} + b_{2,l}\tilde{T} & \text{if } T > T_g \\ b_{1,s} + b_{2,s}\tilde{T} & \text{if } T < T_g \end{cases} \tag{5.2}$$

$$B(T) = \begin{cases} b_{3,l} \exp(-b_{4,l}\tilde{T}) & \text{if } T > T_g \\ b_{3,s} \exp(-b_{4,s}\tilde{T}) & \text{if } T > T_g \end{cases} \tag{5.3}$$

where the glass transition temperature is assumed to be a linear function of pressure given by

$$T_g(p) = b_5 + b_6 p \tag{5.4}$$

and where

$$\tilde{T} = T - b_5 \tag{5.5}$$

with subscripts l and s denoting the liquid and solid phases. The constants for PS reported by Chiang et al. (1991b) are :

$b_{1,l}$	$= 9{,}88 \times 10^{-4}$	m^3/kg
$b_{2,l}$	$= 6{,}10 \times 10^{-7}$	$m^3/kg.^\circ C$
$b_{3,l}$	$= 115{,}0$	MPa
$b_{4,l}$	$= 3{,}66 \times 10^{-3}$	$^\circ C^{-1}$
$b_{1,s}$	$= 9{,}88 \times 10^{-4}$	m_3/kg
$b_{2,s}$	$= 1{,}49 \times 10^{-7}$	$m^3/kg.^\circ C$
$b_{3,s}$	$= 238{,}0$	MPa
$b_{4,s}$	$= 2{,}10 \times 10^{-3}$	$^\circ C^{-1}$
b_5	$= 112{,}0$	$^\circ C$
b_6	$= 7{,}8 \times 10^{-7}$	$^\circ C.Pa^{-1}$

In chapter 2 only the liquid phase density was taken into account in calculating $\tilde{S}$ in the continuity equation (2.28). To take the density of both the liquid and the solid phases of amorphous polymers into account the continuity equation, which is the governing equation for solving the

pressure field, can be written (Chiang et al., 1991a) as

$$G\frac{\partial p}{\partial t} - \frac{\partial}{\partial x}\left(\tilde{S}\,\frac{\partial p}{\partial x}\right) - \frac{\partial}{\partial y}\left(\tilde{S}\,\frac{\partial p}{\partial y}\right) = -F \qquad (5.6)$$

where $$G = \int_0^{\chi}\left(\frac{\partial \rho_l}{\partial p}\right)_T dz + \int_{\chi}^{h}\left(\frac{\partial \rho_s}{\partial p}\right)_T dz \qquad (5.7)$$

and $$F = \int_0^{\chi}\left(\frac{\partial \rho_l}{\partial T}\right)_p \frac{\partial T}{\partial t}\, dz + \int_{\chi}^{h}\left(\frac{\partial \rho_s}{\partial T}\right)_p \frac{\partial T}{\partial t}\, dz\ . \qquad (5.8)$$

$z = \chi$ corresponds to the gapwise location of the solid–liquid interface.

The temperature– and the pressure dependence of the density is taken into account in equation (5.6). This equation is used to solve the filling– and post–filling stages, even though the variable–density effects associated with the G and F terms are negligible during the filling stage Due to substantial cooling in the late post–filling stage, $\tilde{S}$ becomes negligible and eventually the melt becomes stationary. With $\tilde{S}$ negligible, equation (5.6) solves for the pressures through one–dimensional heat transfer involving only the terms $G\frac{\partial p}{\partial t}$ and F. Solutions obtained with equation (5.6) and the double–domain Tait equation of state (5.1) are shown in the example calculations.

5.2.2 Viscosity model

The viscosity model described in section 2.5 is a version of the modified Cross model, equation (1.10), which requires only 5 material constants. This model was used for both the filling and post–filling stages in chapter 2. The function $\eta_0(T,p)$ in (1.10) is given by

$$\eta_0 = B\,\exp\left(\frac{T_b}{T}\right)\exp(\beta p)\ , \qquad (5.9)$$

which is Arhenius–type temperature dependence. B, T_b and β are material constants.

During the post–filling stage substantial cooling occurs and this 5–constant model underpredicts the viscosity as reported by Wang and Hieber (1987). They use a refined version of the modified Cross model with WLF–type temperature dependence for the post–filling stage. This version of the model requires 7 material constants with η_0 in equation (1.10) given by

$$\eta_0 = D_1 \exp[-A_1(T - T^*)/(A_2 + (T - T^*)] \quad , \qquad (5.10)$$

where $$A_2(p) = \tilde{A}_2 + D_3 p \qquad (5.11)$$

and $$T^*(p) = D_2 + D_3 p \quad . \qquad (5.12)$$

D_1, D_2, D_3 A_1 and $\tilde{A}_2$ are material constants.

The 7 constants for PS, reported by Chiang et al. (1991b), are :

$n = 0{,}26$
$\tau^* = 2{,}50 \times 10^4$ Pa
$D_1 = 4{,}36 \times 10^{11}$ Pa.s
$D_2 = 100{,}0$ °C
$D_3 = 2{,}3 \times 10^{-7}$ °C/Pa
$A_1 = 27{,}45$
$\tilde{A}_2 = 48{,}0$ °C

The above–mentioned authors used the 5–constant model for the filling stage and the 7–constant model for the post–filling stage. They report that the two models give virtually the same results for the filling stage, but the 7–constant model is more accurate for the post–filling stage. The GHS model can therefore be refined to do a unified simulation of

the filling– and post–filling stages by employing the 7–constant model in both stages. The difference in the pressure development during the post–filling stage, based on calculations using the 5–constant and 7–constant models, are demonstrated in the example calculations.

5.3 One–dimensional and two–dimensional flow

The flow in the cavity with a film gate shown in Figure 5.1 will be one–dimensional flow while the flow in the cavity shown in Figure 5.2, which has a direct sprue gate will be two–dimensional.

5.3.1 One–dimensional flow to demonstrate the refined GHS model

Consider the thin cavity shown in Figure 5.1, which is closed on all sides except at the inlet where a constant flow rate is specified along the length of the inlet. The wall temperature at the fixed walls in the x–z plane is below T_g. Two flow cases are considered. During the filling stage the polymer melt flows into the cavity through the inlet. The flow front moves through the cavity until it reaches the closed outlet. At this instant the cavity is filled and the post–filling stage commences. For this flow case a holding pressure is specified at the inlet. During the post–filling stage more material flows into the cavity and the pressures throughout the closed cavity increase until the melt becomes stationary. Simultaneously the temperatures of the melt decrease due to heat transfer to the colder wall and the melt solidifies progressively inwards. Once the melt has become stationary the pressures will decrease as the material cools down.

5.3.2 Two–dimensional flow

Consider the cavity shown in Figure 5.2 which is closed on all sides. The polymer melt flows radially outwards from the inlet and reaches the closed sides nearest to the inlet first. As more material flows into the cavity the pressure will start to build up at the sides until the material reaches the other two sides of the cavity and the cavity is filled.

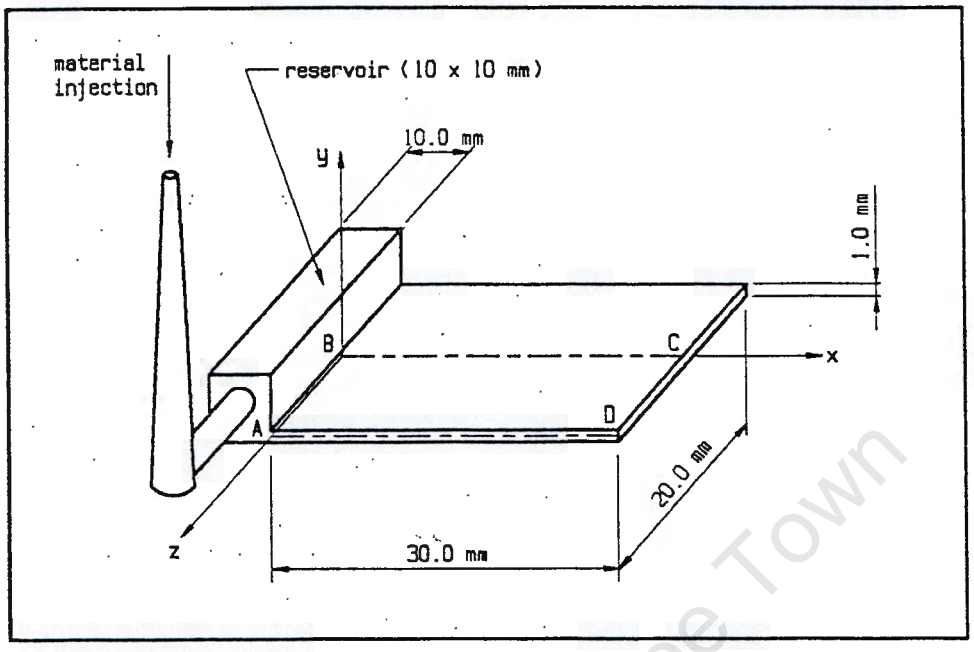

FIGURE 5.1 Geometry of an injection moulded part with a film gate

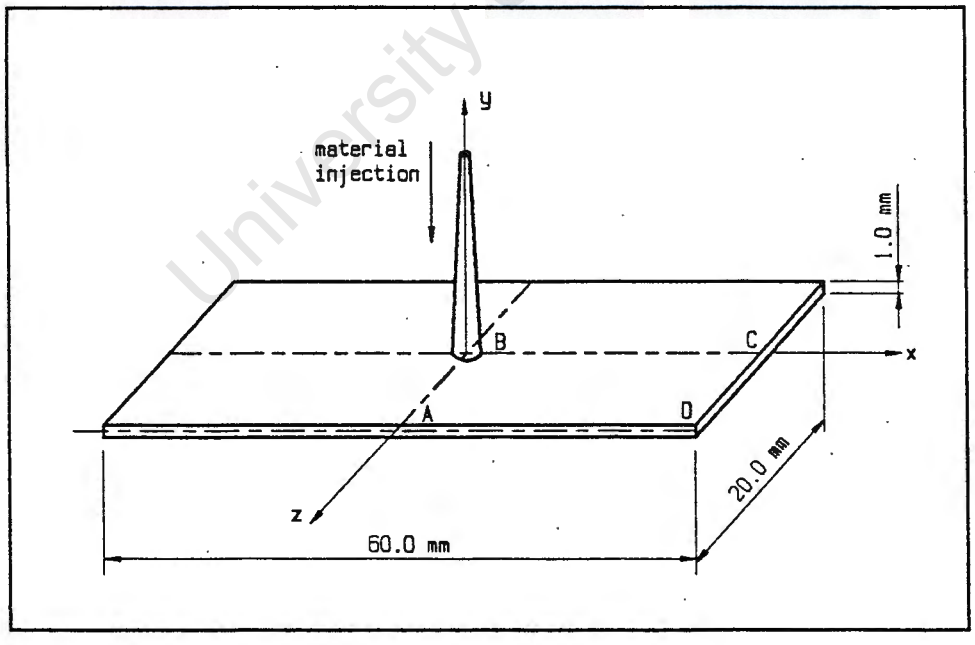

FIGURE 5.2 Geometry of an injection moulded part with a direct sprue gate

5.4 Example calculations

5.4.1 One–dimensional flow simulated with the refined GHS model

The complete process of filling and post–filling, including cooling, is simulated for the geometry shown in Figure 5.1. The resulting pressure development in the filling– and post–filling stages and the influence of the holding pressure are shown.

Consider the filling of the thin rectangular cavity, of which a quarter model is shown in Figure 5.3, with PS and the subsequent compression and cooling of the material.

The specified flow rate at the inlet is 5,0 cm^3/s. The temperature of the inflowing melt is 210° C and the temperature of the fixed wall is kept at 60° C which is below T_g. The material constants for PS given in section 2.4 are used in the 5–constant viscosity model and the

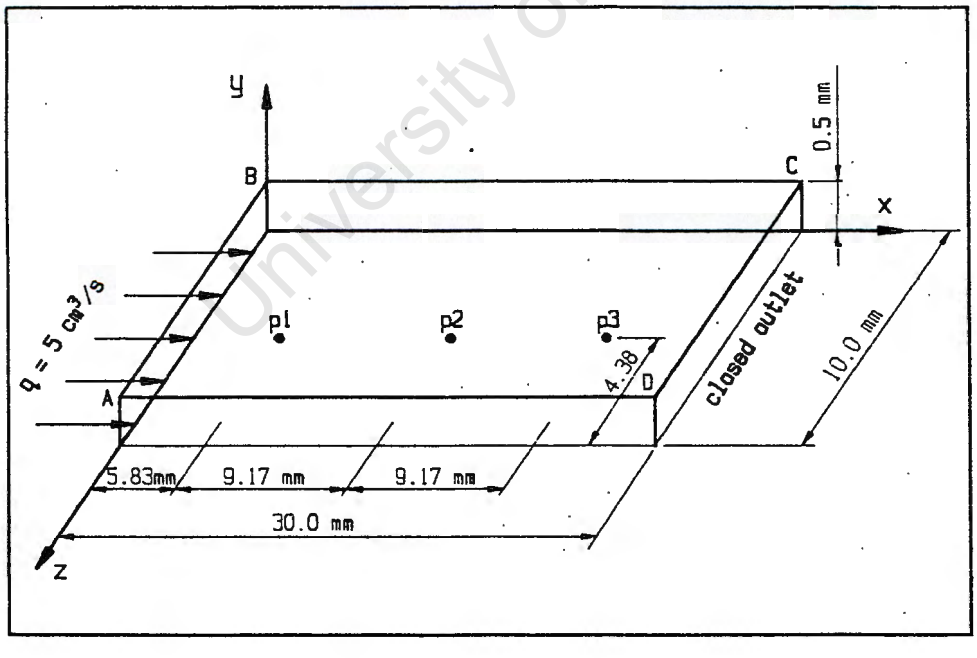

FIGURE 5.3 A quarter model of the cavity with one–dimensional flow

material constants given in section 5.2 above are used in the 7–constant model. The thermal properties for PS were given in section 2.4.

The development of the pressures at nodes p1, p2 and p3 during the post–filling stage, calculated by using, respectively, the 5–constant and 7–constant viscosity models in the GHS model, are shown in Figures 5.4 and 5.5. The lines are best curve fits through the discrete values calculated at different times during the post–filling stage. The double–domain Tait equation was used in both cases. By comparing these two figures the difference in the pressure development of the pressures, obtained with the two versions of the viscosity model, can be seen. Chiang et al. (1991b) have shown that the results based on the 7–constant model correspond well with experimental results. They report that the difference in the results based on the two models is due to the to the fact that, unlike the WLF functional form in the 7–constant model, the 5–constant model does not reflect a markedly increased temperature sensitivity as the temperature of the amorphous material drops into the glass–transition range.

The development of the pressures at p1, p2 and p3 during the filling– and post–filling stages are shown in Figure 5.6. The results were obtained with the refined GHS model including the double–domain Tait equation of state, the 7–constant viscosity model and equation (5.6) to model the cooling effects. After the flow front has reached each node the pressure at that node increases until the short filling stage is completed. During the post–filling stage the pressures increase to their peak values due to the holding pressure. After the melt has become stationary the pressures decrease to atmospheric pressure during the longer cooling time.

In the simulation of the complete injection moulding process, described above, the pressure at the inlet at the end of the filling stage was used

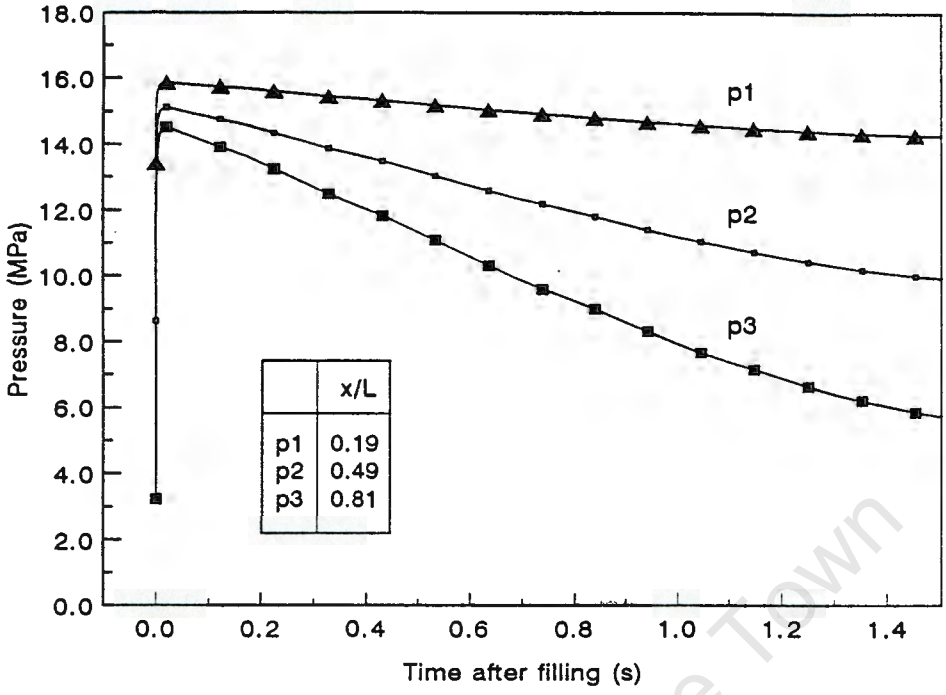

FIGURE 5.4 Pressure development during the post–filling stage based on the 5–constant viscosity model.

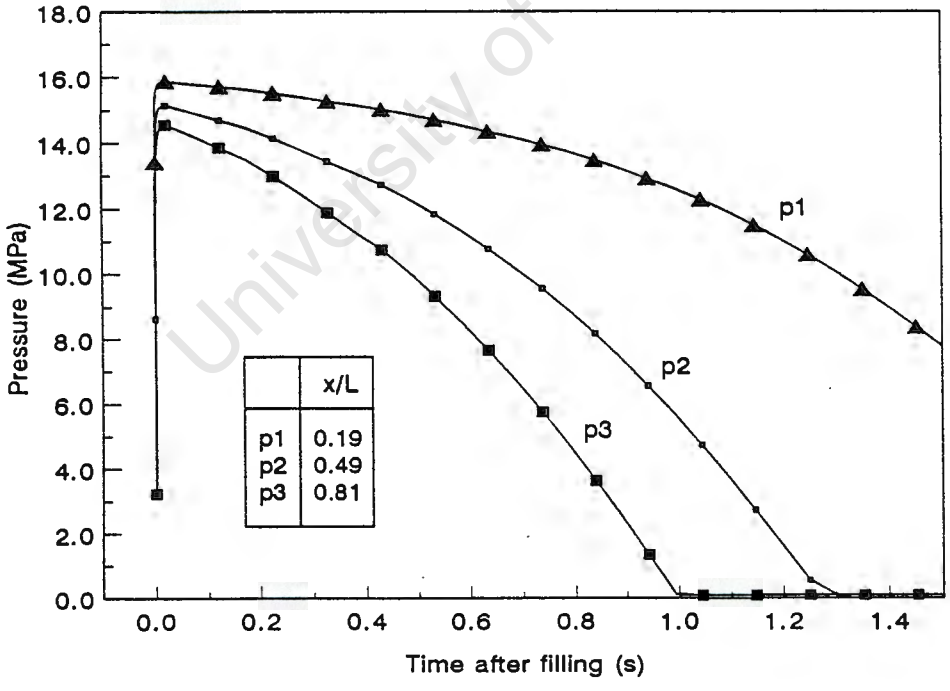

FIGURE 5.5 Pressure development during the post–filling stage based on the 7–constant viscosity model.

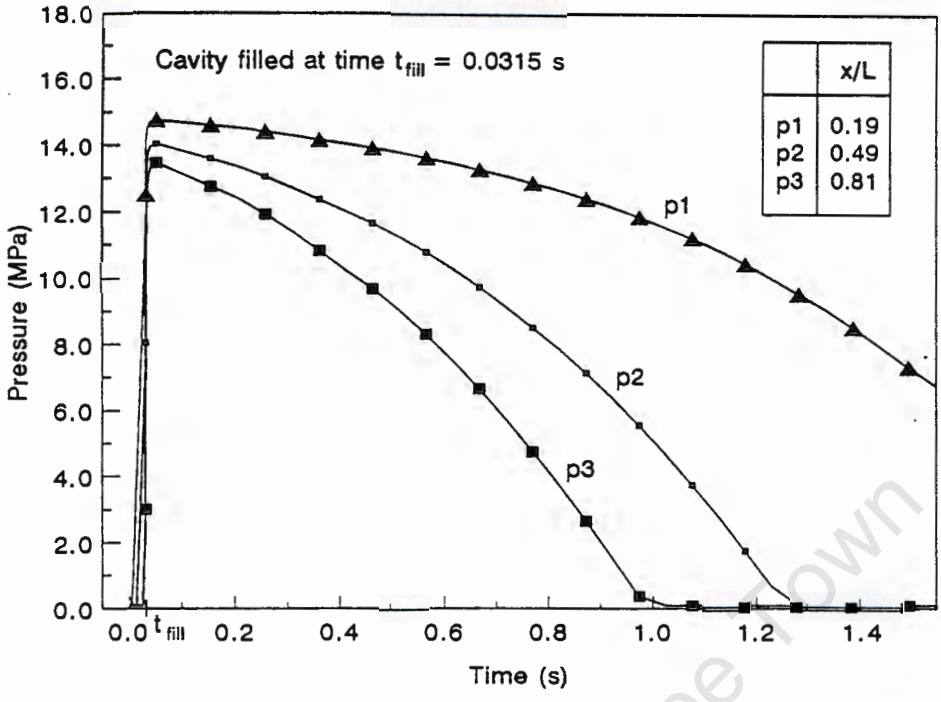

FIGURE 5.6 Pressure development during filling and post–filling.

as the constant holding pressure during the post–filling stage. In practice a higher holding pressure would be set on the injection moulding machine to avoid sinkmarks in the product caused by shrinkage during cooling. To do a more realistic simulation of the actual pressure development during the injection moulding process, a holding pressure of 25,0 MPa is specified for the example described above, as compared to the inlet pressure of 14,7 MPa at the end of the filling stage. The pressure development is shown in Figure 5.7. When the filling stage has been completed, the pressure at the inlet is increased to 25,0 MPa and the pressures at the three positions considered increase accordingly before dropping again due to cooling. To compare the difference in the development of the pressures when different holding pressures are specified, the results in Figure 5.6 and 5.7 are shown on the same scale in Figure 5.8. With a higher holding pressure, a longer cooling time is required for the pressures to reach atmospheric pressure than with the lower holding pressure.

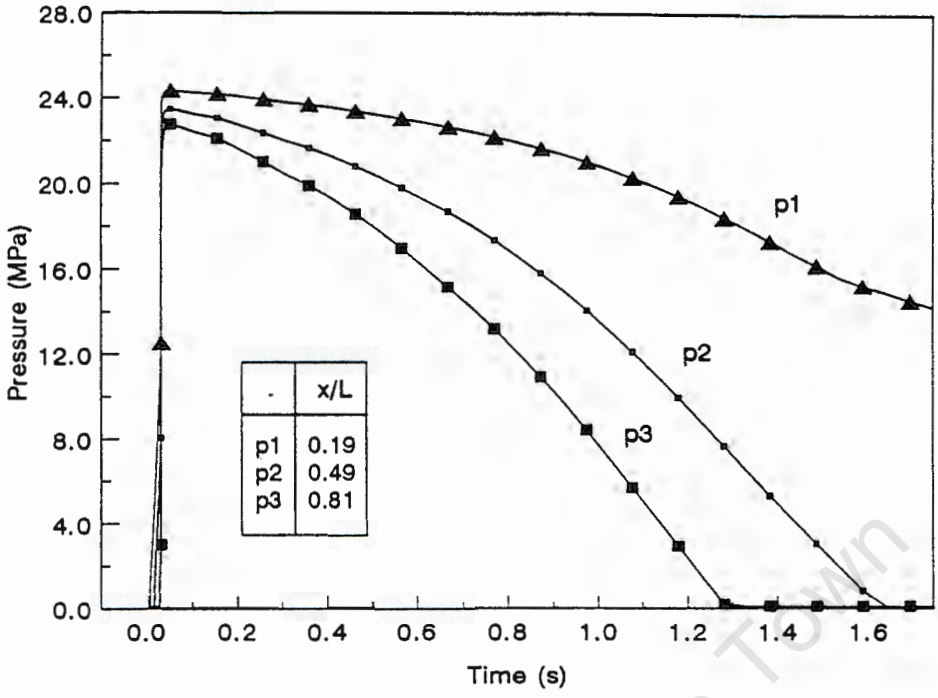

FIGURE 5.7 Pressure development during injection moulding with increased holding pressure.

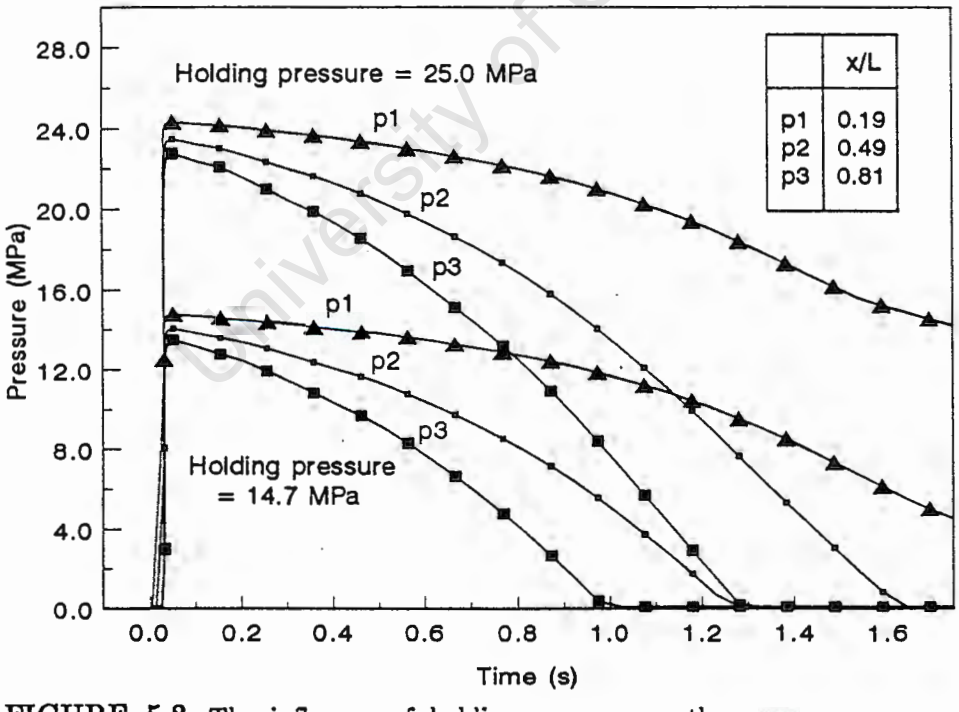

FIGURE 5.8 The influence of holding pressure on the pressure development during the post–filling stage.

5.4.2 A two–dimensional flow case

A quarter model of the cavity with a direct sprue gate at the centre (see Figure 5.2) is shown in Figure 5.9. Consider the filling of the cavity with molten PS at a specified flow rate of 20 cm^3/s at the inlet. The temperature of the inflowing melt is 210°C and the fixed wall is kept at a temperature of 60°C. The polymer melt flows radially outwards from the inlet and reaches the closed sides nearest to the inlet first. As more material flows into the cavity the pressure will start to build up at these sides until the material reaches the other two sides of the cavity and the cavity is filled.

This two–dimensional flow case was solved with a generalized Hele–Shaw model, including the movement of the flow front, as reported by Kietzmann (1993). The time dependent pressure development at p1, p2

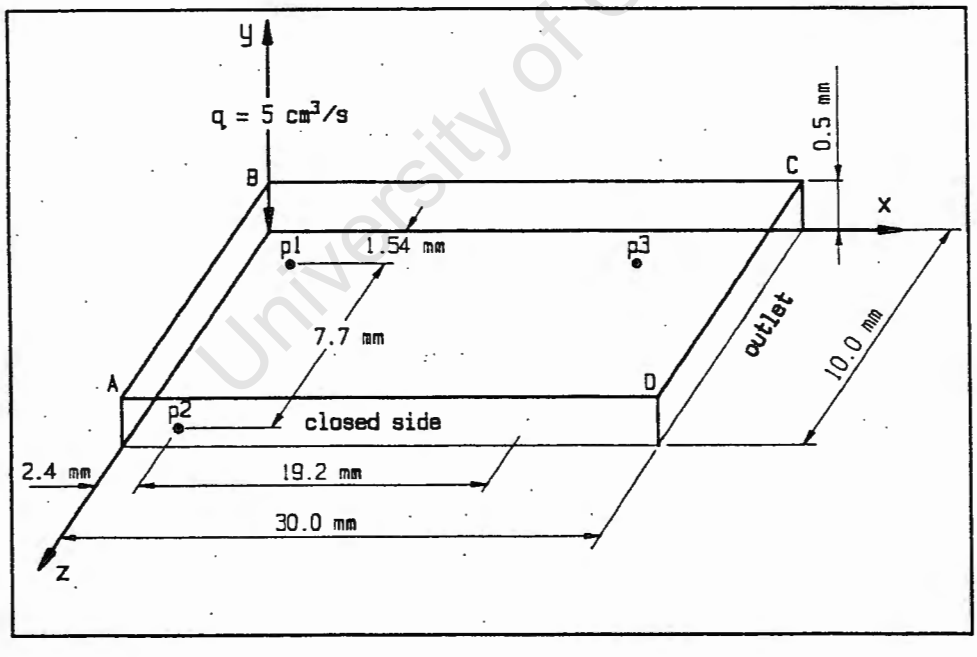

FIGURE 5.9 A quarter model of the cavity with two–dimensional flow

and p3 is shown in Figure 5.10. The most significant difference in the results of this flow case as compared to a one–dimensional flow case is that there are pressure drops in both the x and z directions. In Figure 5.11 the pressure drop in the x direction along a line through p1 and p3 is shown. In Figure 5.12 the pressure drop in the z direction along a line through p1 and p2 is shown. At a time t = 0,007 s the flow front reaches the side of the cavity nearest to the inlet. As more material enters the the cavity the pressures at the inlet and at the sides of the cavity increase further until the cavity is filled at time t = 0,031 s.

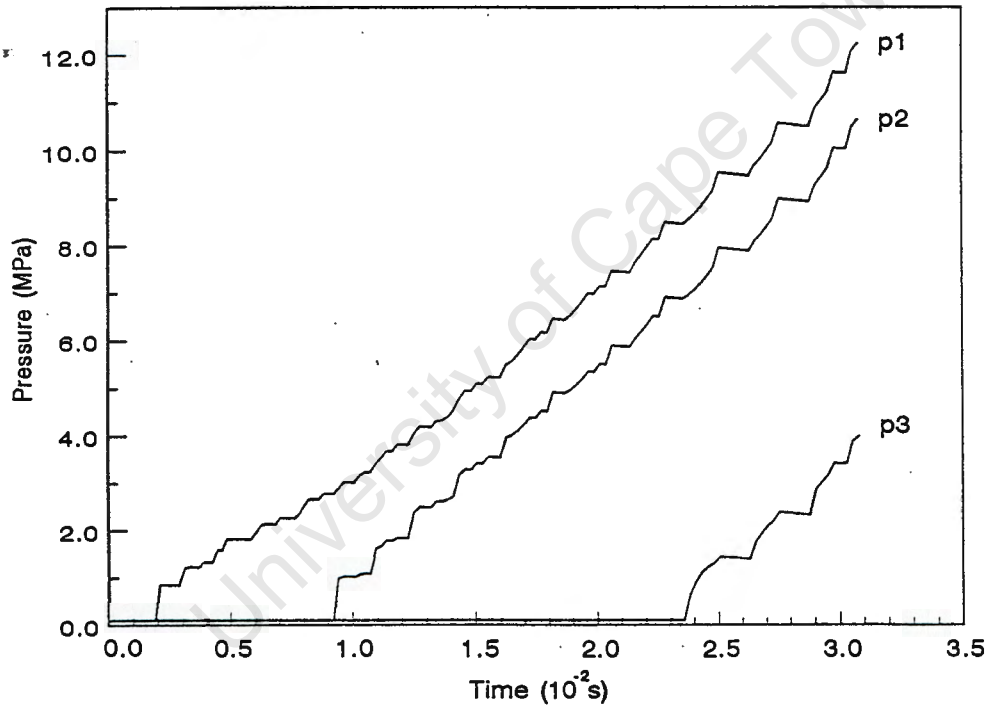

FIGURE 5.10 Time–dependent pressure development in two–dimensional flow

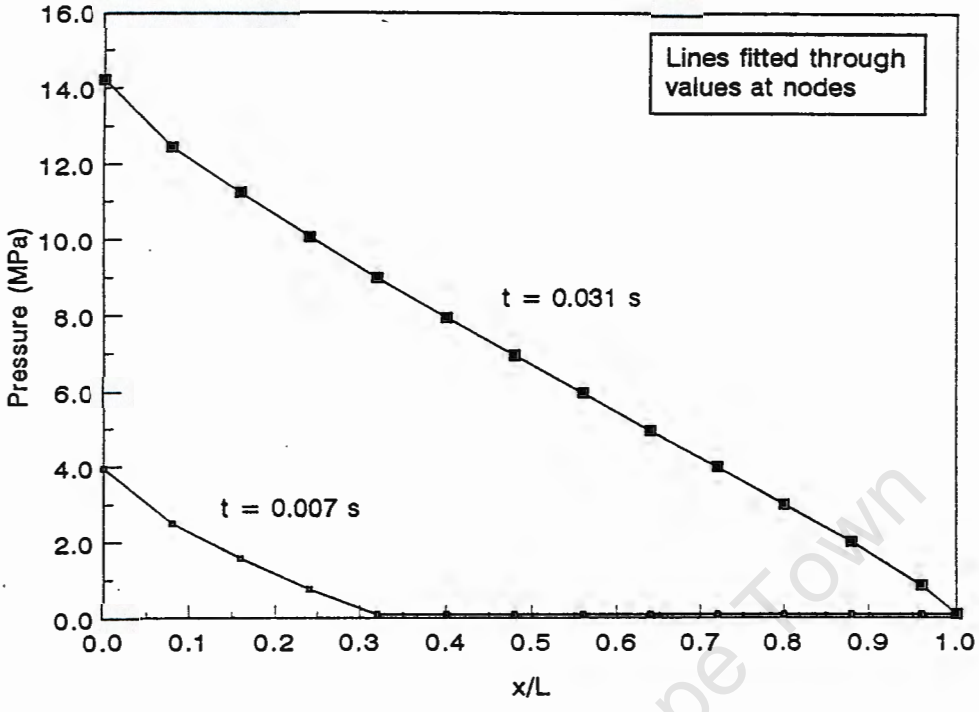

FIGURE 5.11 Pressure drop in the x direction of two–dimensional flow

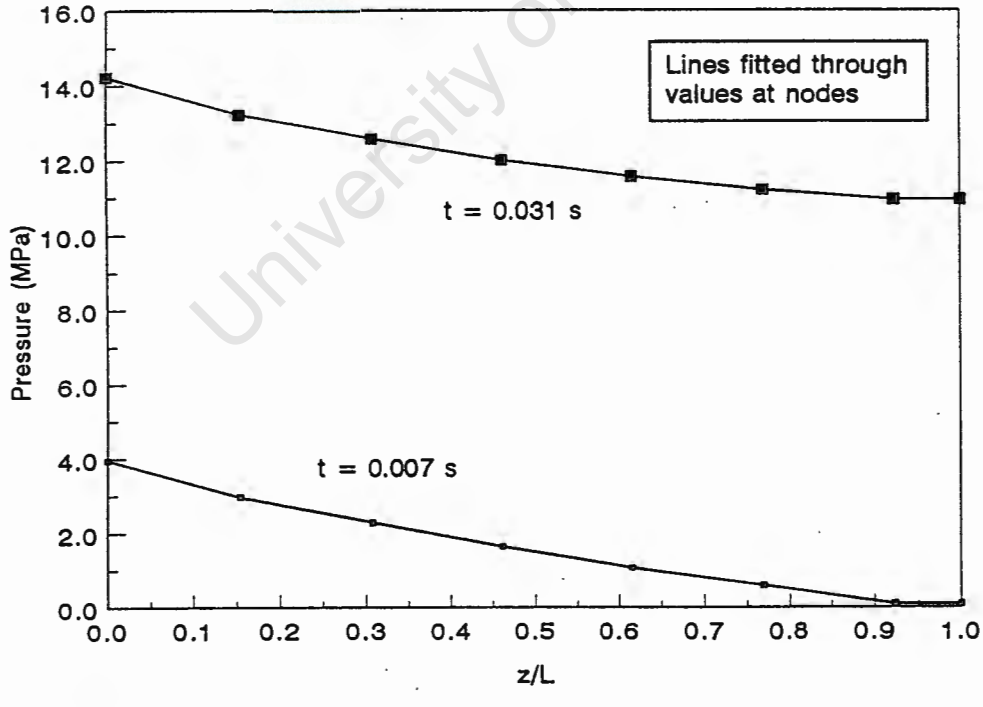

FIGURE 5.12 Pressure drop in the z direction of two–dimensional flow

5.5 Summary

A one–dimensional flow case has been simulated to demonstrate the filling stage with movement of the flow front and the post–filling stage with packing and cooling. The GHS model has been refined to model the cooling effects during the post–filling stage. The density and the viscosity have also been modelled more accurately. The influence of two viscosity models on the pressure development in the post–filling stage was determined. It was concluded that the same constitutive equations can be used to model the filling– and the post–filling stages, including cooling. The effect of the holding pressure and the effect of cooling on the pressure development have been demonstrated.

A two–dimensional flow case has also been simulated. The time–dependent pressure development and the pressure drops in two perpendicular directions have been demonstrated.

CHAPTER 6

6 CLOSURE

6.1 Summary

The conclusions made as a consequence of this study can be summarized as follows :

i) Numerical models to simulate the injection moulding process can be simplified and the computer time required to solve these models can be reduced by using the Hele–Shaw formulation instead of solving the full Navier–Stokes equations.

ii) Numerical models based on the Hele–Shaw formulation are well suited to simulate the injection moulding process when the geometries and flow conditions fall within certain limits. These limits are determined by the combined effect of the geometry and the flow conditions as represented by the Reynolds number for each flow case.

iii) The simplicity of the finite volume method used in the generalized Hele–Shaw model makes it an attractive model to use for the simulation of the injection moulding process.

6.1 Conclusion

Numerical simulation of the injection moulding process has become a crucial part of advanced injection mould design. Considering the high cost and the time required to produce injection moulds, the designer can no longer rely on his experience only. During recent years the need to accurately predict the parameters required in sophisticated injection mould design has been addressed increasingly by the use of computer simulation techniques.

The generalized Hele–Shaw (GHS) model simplifies the numerical simulation of the injection moulding process as compared to a model solving the full Navier–Stokes equations. The solution algorithms are less complex since the pressure and the velocities are not solved simultaneously as in a model which solves the full momentum equations. The computer time required is also reduced since a model solving the Navier–Stokes equations requires time–steps which are much smaller than the time–steps required by the GHS model to obtain a time–step independent solution.

Numerical models based on the Hele–Shaw formulation are well suited for injection moulding simulations. Although the Hele–Shaw formulation is based on certain approximations, it is widely used to simulate the injection moulding process when viscoelastic effects are not considered. By comparing the solutions obtained using a generalized Hele–Shaw model with the solution obtained by solving the full Navier–Stokes equations, it was established that the influence of the Hele–Shaw approximations on the solutions are within acceptable limits for a range of Reynolds numbers. This range of Reynolds numbers, which represents the combined effect of the geometry and the flow conditions, are determined by the Hele–Shaw assumptions : Firstly, the thickness dimension has to be small enough to ensure that the flow is predominantly shear flow and the velocity component in the thickness direction is negligible. Secondly, the viscous forces resulting from the combined effect of the inlet velocity and the thickness dimension must always be smaller than the inertial forces.

Most researchers use finite element methods in the numerical schemes employed to simulate the injection moulding process. Although the finite volume method is very powerful it has not yet been well established for the simulation of the injection moulding process. The simplicity of the finite volume method has been demonstrated in this thesis. Due to its simplicity it is easier to use than the finite element

method. It has been shown that the GHS model, which employs a finite volume method, can be used for injection moulding simulations.

6.3 Need for further work

Viscoelastic effects are important when residual stresses or orientation in a part has to be predicted. The Hele–Shaw formulation can only be used if these effects are negligible. Unless a simulation model is specifically required to take viscoelastic effects into account they are not included due to the complexity of the viscoelastic constitutive equations and because three hydrodynamic variables u, v, and p need to be solved simultaneously by the numerical scheme. Therefore, there is a need for further work to incorporate viscoelastic effects more effectively in simulation models to predict residual stresses and orientation.

Since the subject of crystallinity falls outside the scope of this thesis the constitutive equations used only applies to amorphous polymers and not to crystalline or semi–crystalline polymers. For these types of materials different material constants are required in the constitutive equations and the effect of crystallinity at the boundary between the solid and liquid phases has to be included. This will require further development work.

There is a need to develop the GHS model further to simulate more complex planar geometries. When an injection mould is simultaneously filled from two gates or the injected polymer flows around an insert in the mould the flow fronts meet during the filling stage, forming a weld line. The extension of the GHS model to include the prediction of weld lines will require the use of either an unstructured grid or a moving grid. Weld line prediction is important in the design of plastic products where the weld lines influence the aesthetics or the structural strength of the product.

There is also a need to develop the GHS model further to simulate the filling– and post–filling stages for curved geometries by using curvilinear coordinates. Although many three–dimensional products can be approximated by curved planes, further work is also needed to extend the model to more complex geometries with, for example, ribs and flanges.

Although the movement of the flow front in two–dimensions was simulated with an existing model based on the Hele–Shaw formulation, there is a need to extend and refine the simulation of the flow front movement used in the GHS model.

The development work mentioned above covers only a few of the wide range of aspects that can be addressed in the ongoing research work on the numerical simulation of the injection moulding process.

REFERENCES

AGASSANT, J.F., AVENDAS, P., SERGENT, J.P. & CARREAU, P.J. 1991. Polymer processing. Principles and modeling. Munich : Hanser. 475p.

AGASSANT, J.F. & VILLEMAIRE, J.P. 1988. Rheology for polymer processing : an overview of the present knowledge and some open problems. Makromolekular Chemie, Macromolecular Symposium, 22:39–57.

ANDERSON, D.A., TANNEHILL, J.C. & PLETCHER, R.H. 1984. Computational fluid mechanics and heat transfer. New York : Hemisphere. 599 p.

BENODEKAR, R.W., GODDARD, A.J.H., GOSMAN, A.D. & ISSA, R.I. 1985. Numerical prediction of turbulent flow over surface–mounted ribs. AIAA journal, 23 (3):359–366.

BIRD, R.B., ARMSTRONG, R.C. & HASSAGER, O. 1977. Vol I : Dynamics of polymer liquids. New York : Wiley. 470 p.

BIRD, R.B., STEWART, N.E. & LIGHTFOOT, E.N. 1960. Transport phenomena. New York : Wiley. 780 p.

BREUER, H. & REHAGE, G. 1967. Zur Thermodynamik der glasigen Erstarrung. Kolloid–Zeitschrift und Zeitschrift für Polymere, 216/217:159–179.

BROWNE, L.W.B. 1978. The marker and cell technique. (In Noye, J., ed. Numerical simulation of fluid motion. Amsterdam : North–Holland. p. 223–247.)

BROYER, E., GUTFINGER, C. & TADMOR, Z. 1975. A theoretical model for the cavity filling process in injection molding. Transactions of the Society of Rheology, 19(3):423–444.

CHIANG, H.H., HIEBER, C.A. & WANG, K.K. 1991a. A unified simulation of the filling and post filling stages in injection molding. Part I. Formulation. Polymer engineering and science, 31 (2):116–124.

CHIANG, H.H., HIEBER, C.A. & WANG, K.K. 1991b. A unified simulation of the filling and post filling stages in injection molding. Part II. Experimental Verification. Polymer engineering and science, 31(2):125–139.

CROSS, M.M. 1979. Relation between viscoelasticity and shear–thinning behavior in liquids. Rheologica acta, 18(5):609–614.

DUPRET, F. & VANDERSCHUREN, L. 1988. Calculation of the temperature field in injection molding. AIChe journal, 34(12):1959–1972.

GüCERI, S. 1989. Finite difference solution of field problems (In Tucker, C.L., ed. Fundamentals of computer modeling for polymer processing. Munich : Hanser. p. 142–236.)

HIEBER, C.A. 1987. Melt–viscosity characterization and its application to injection molding. (In Isayev, A.I., ed. Injection and compression molding fundamentals. New York : Marcel Dekker. p. 1–136.)

HIEBER, C.A. & CHIANG, H.H. 1989. Some correlations involving the shear viscosity of polystyrene melts. Rheologica acta, 28(4):321–332.

HIEBER, C.A. & SHEN, S.F. 1978. Flow analysis of the non–isothermal two–dimensional filling process in injection moulding. Israel Journal of Technology, 16(1):248–259.

HIEBER, C.A. & SHEN, S.F. 1980. A finite–element/finite–difference simulation of the injection–molding filling process. Journal of non–newtonian fluid mechanics, 7(1):1–32.

HIEBER, C.A., SOCHA, L.S., SHEN, S.F., WANG, K.K. & ISAYEV, A.I. 1983. Filling thin cavities of variable gap thickness : A numerical and experimental investigation. Polymer engineering and science, 23(1):20–26.

HIEBER, C.A., VANDENENGEL, G. & CHIANG, H.H. 1986. Cavity–pressure variations during the post–filling stage of injection molding. (In Annual Technical Conference of the Society of Plastics Engineers, 44th, Boston, USA. Brookfield. p. 181–184.)

HIRT, C.W. & NICHOLS, B.D. 1981. Volume of fluid (VOF) method for the dynamics of free boundaries. Journal of computational physics, 39(1):201–225.

HUILIER, D., LENFANT, G., TERISSE, J. & DETERRE, R. 1988a. Modeling the packing stage in injection molding of thermoplastics. Polymer engineering and science, 28(24):1637–1643.

HUILIER, D. & PATTERSON, W.I. 1991. Simulation of the packing and cooling phases of thermoplastics injection molding. (In Isayev, A.I., ed. Modeling of polymer processing. Recent developments. Munich : Hanser. p. 174–201).

HUILIER, D., TERISSE, J., DE LA LANDE, M.E. & LATROBE, A. 1988b. Modeling the packing cooling stage in injection molding of amorphous polymers. International polymer processing, 3(4):184–190.

ISSA, R. I. 1986. Solution of the implicity discretised fluid flow equations by operator – splitting. Journal of computational physics, 62(1):40–65.

KAMAL, M.R., GOYAL, S.K. & CHU, E. 1988. Simulation of injection mold filling of viscoelastic polymer with fountain flow. AIChe journal, 34(1):94–106.

KAMAL, M.R. & LAFLEUR, P.G. 1982. Computer simulation of injection molding. Polymer engineering and science, 22(27):1066–1074.

KAMAL, M.R. & LAFLEUR, P.G. 1986. A structure–oriented computer simulation of the injection molding of viscoelastic crystalline polymers. Part II. Model prediction and experimental results. Polymer engineering and science, 26(1):103–110.

KAMAL, M.R. & RYAN, M.E. 1989. Models of material behaviour. (In Tucker, C.L., ed. Fundamentals of computer modeling for polymer processing. Munich : Hanser. p. 8–68.)

KIETZMANN, C.v.L. 1994. The numerical simulation of plastics injection mould flow using a thin gap numerical model. Potchefstroom. (Thesis (M.Eng.) – PUCHE.)

LAFLEUR, P.G. & KAMAL, M.R. 1986. A structure–oriented computer simulation of the injection molding of viscoelastic crystalline polymers. Part I. Model with fountain flow, packing, solidification. Polymer engineering and science, 26(1):92–102.

LEE, C. & CASTRO, J.M. 1989. Model simplification. (In Tucker, C.L., ed. Fundamentals of computer modeling for polymer processing. Munich : Hanser. p. 69–140.)

LE GRANGE, L.A. 1990. Numerical simulation of polymer melt flow in a mould using a boundary–fitted coordinate system. Vanderbijlpark. (Thesis (M.Eng.) – PUCHE.)

MAVRIDIS, H., HRYMAK, A.N. & VLACHOPOULOS, J. 1986. Finite element simulation of fountain flow in injection molding. Polymer engineering and science, 26(7):449–454.

MICHAELI, W. & LAUTERBACH, M. 1989. Die pmT–Optimierung – Konsequenzen aus dem pvT – Konzept zur Nachdruck führung. Kunststoffe German plastics, 79(9):852–856.

NAUDé, W. 1992. Plastics Federation of South Africa. Johannesburg. (Personal discussions with author.)

PATANKAR, S.V. 1984. Numerical heat transfer and fluid flow. New York : McGraw–Hill. 197 p.

PHILIPON, S., ALLES, H., VINCENT, M. & AGGASSANT, J.F. 1986. Thermoplastic injection molding : modelling of the filling of a complex geometry mold. (In Proceedings of the 2nd International Conference on Numerical Methods in Industrial Forming Processes. Gothenburg. Sweden. p.177–182.)

POWELL, P.D. 1983. Engineering with polymers. London : Chapman and Hall. 318 p.

RICHARDSON, S. 1972. Hele–Shaw flows with a free boundary produced by the injection of fluid into a narrow channel. Journal of fluid mechanics, 56(4):609–618.

ROACHE, P.J. 1972. Computational fluid dynamics. Albuquerque, N.M. : Hermosa. 446 p.

SCHLICHTING, H. 1979. Boundary–layer theory. 7th ed. New York : McGraw–Hill. 817 p.

SCHMIDT, T.W. & MENGES, G. 1986. Calculation of the packing phase in injection molding with a two–layer segment model. (In Annual Technical Conference of the Society of Plastics Engineers, 44th Boston USA. Brookfield. p. 92–96.)

SHAMES, I.H. 1982. Mechanics of fluids. 2nd ed. Singapore : McGraw–Hill. 690 p.

VAN DOORMAAL, J.P. & RAITHBY, G.D. 1984. Enhancements of the simple method for predicting incompressible fluid flows. Numerical Heat Transfer, 7(2):147–163.

WANG, K.K. & HIEBER, C.A. 1987. A viscosity–based simulation of the injection–molding process. (In Samanta, S.K., Komanduri, R., McKeeking, R., Chen, M.M. & Tseng, A., eds. Interdisciplinary issues in materials processing and manufacturing, vol 2. New York : ASME. p. 645–660.)

WANG, K.K. & HIEBER, C.A. 1988. Injection molding simulation. (In Gutowski, T.G., ed. The manufacturing science of composites, vol. 4. New York : ASME. p. 87–94.)

WANG, K.K., HIEBER, C.A. & WANG, K.K. 1986. Dynamic simulation and graphics for the injection molding of three–dimensional thin parts. Journal of polymer engineering, 7(1):21–45.

WANG, H.P. & LEE, H.S. 1989. Numerical techniques for free and moving boundary problems. (In Tucker, C.L., ed. Fundamentals of computer modelling for polymer processing. Munich : Hanser. p. 369–402.)

WILLIAMS, M.L., LANDEL, R.F. & FERRY, J.D. 1955. The temperature dependence of relaxation mechanisms in amorphous polymers and other glass–forming liquids. Journal of the American Chemical Society, 77(14):3701–3707.

WOOD, L.A. 1964. Utility of the Tait equation relating volume and pressure in the study of transitions in polymers. Journal of polymer science, B, 2(7):703–707.